Titre: Title:	Organic Gate Dielectrics for Tetracene Field Effect Transistors
Auteur: Author:	Simone Bertolazzi
Date:	2010
Type:	Mémoire ou thèse / Dissertation or Thesis
Référence: Citation:	Bertolazzi, S. (2010). Organic Gate Dielectrics for Tetracene Field Effect Transistors [Mémoire de maîtrise, École Polytechnique de Montréal]. PolyPublie. https://publications.polymtl.ca/478/

URL de PolyPublie: PolyPublie URL:	https://publications.polymtl.ca/478/
Directeurs de recherche: Advisors:	Clara Santato, & Federico Rosei
Programme: Program:	Génie physique

UNIVERSITÉ DE MONTRÉAL

ORGANIC GATE DIELECTRICS FOR TETRACENE FIELD EFFECT TRANSISTORS

SIMONE BERTOLAZZI

DÉPARTEMENT DE GÉNIE PHYSIQUE

ÉCOLE POLYTECHNIQUE DE MONTRÉAL

MÉMOIRE PRÉSENTÉ EN VUE DE L'OBTENTION

DU DIPLÔME DE MAÎTRISE ÈS SCIENCES APPLIQUÉE

(GÉNIE PHYSIQUE)

DÉCEMBRE 2010

UNIVERSITÉ DE MONTRÉAL

ÉCOLE POLYTECHNIQUE DE MONTRÉAL

Ce mémoire intitulé:

ORGANIC GATE DIELECTRICS FOR TETRACENE FIELD EFFECT TRANSISTORS

présenté par : BERTOLAZZI Simone

en vue de l'obtention du diplôme de : Maîtrise ès sciences appliquée

a été dûment accepté par le jury d'examen constitué de:

M. MASUT Remo A., Ph.D., président

Mme SANTATO Clara, Ph.D., membre et directrice de recherche

M. ROSEI Federico, Ph.D., membre et codirecteur de recherche

M. DESJARDINS Patrick, Ph.D., membre.

DÉDICACE

A mio padre e mia madre

« Si tu veux construire un bateau, ne rassemble pas des hommes pour aller chercher du bois, préparer des outils, répartir les tâches, alléger le travail… mais enseigne aux gens la nostalgie de l'infini de la mer »

Antoine de Saint-Exupéry

ACKNOWLEDGMENTS

There are many people that I want to thank, without whom this work would not have been possible. First of all, I want to express my gratitude to my supervisor, Clara Santato, for introducing me to organic electronics and to the world of scientific research. I owe her much in terms of scientific knowledge and methods: she taught me how to tackle a scientific problem and let me participate in high-level scientific activities, including the MRS conference in Boston, F-Pi-9 in Atlanta and the research experience at the synchrotron in Trieste, Italy.

I thank FQRNT (Fonds Québécois de la Recherche sur la Nature et les Technologies) for financial support and Politecnico di Milano for choosing me to participate in its double degree program at École Polytechnique de Montréal. It has been a unique experience and I am sure that I received a lot from many points of views; not only scientific knowledge and technical experience but also culture and humanity.

I want to thank all the laboratory technicians, for their silent but invaluable work, in particular Joël Bouchard and François Rigano. I am also thankful to Fabio Cicoira, Khalid Laaziri, Jacqueline Sanchez and Patricia Moraille for their precious technical and scientific advices.

Here in Montréal I was surrounded by friendly people that supported me throughout this time. I am deeply grateful all the students in Clara Santato's group for their friendship and for the good time spent together in the laboratory. I want also to thank Charles Brosseau and Gaëlle Terrom, who helped me to prepare the polymer dielectric layers and to carry out the AFM imaging of the tetracene films, and François La Pointe, for helping me with the silanization process.

Last but not least, a huge thanks to my family, who made the sacrifice to let me live abroad for more than two years, and to all the friends in Italy, in Canada and worldwide for helping me to take the right steps throughout my life.

RÉSUMÉ

Dans les trois dernières décennies, les couches minces de semiconducteurs organiques ont fait l'objet de recherches intensives. Ces couches peuvent être utilisées dans une grande variété de dispositifs optoélectroniques de nouvelle génération, tels que les diodes électroluminescentes (OLED), les transistors à effet de champ (OFET), et les cellules photovoltaïques. Récemment, des couches minces poly-cristallines de tétracène, sublimées sous vide, ont été utilisées pour réaliser le premier transistor organique à effet de champ émetteur de lumière (OLEFET), qui intègre dans un seul dispositif la fonction de modulation du courant typique d'un transistor avec la capacité de production de lumière d'une diode électroluminescente.

La démonstration des OLEFETs n'est pas simple. Tout d'abord, une intégration efficace des fonctions optiques et électroniques nécessite l'utilisation d'un semiconducteur électroluminescent ayant aussi des propriétés de transport de charge intéressantes. Deuxièmement, un transport de charge ambipolaire (i.e. de trous et d'électrons) doit être réalisé pour produire des OLEFETs à haute performance. Dans ce contexte, le contrôle de la chimie de surface du substrat diélectrique s'est révélé être une stratégie efficace pour limiter la suppression du transport des électrons induite par les états électroniques pièges à l'interface diélectrique/semiconducteur. En même temps, la modification de la nature chimique et physique du substrat diélectrique influence la morphologie/structure des couches minces organiques, qui à son tour influence la performance du dispositif.

Dans le cadre de ce projet, des couches minces poly-cristallines de tétracène – pour applications dans les OLEFETs – ont été sublimées sous vide sur différents substrats organiques diélectriques, y compris des polymères (parylène C, poly méthacrylate de méthyle, polystyrène) et des monocouches auto-assemblées d'hexaméthyldisilazane (HMDS) et octadécyltrichlorosilane (OTS). Le taux de dépôt était de 3.5 Å/s, la pression à l'intérieur de la chambre à vide était de 2.5×10^{-6} Torr, les substrats ont été maintenus à température ambiante.

Le processus de germination et croissance a été étudié à partir des premières étapes de la croissance jusqu'au recouvrement complet de la surface, au moyen de la microscopie à force atomique (AFM) ex-situ. La densité de nucléation, la forme des grains cristallins et leur inter-

connectivité dépendent fortement des propriétés physiques et chimiques de la surface diélectrique.

Des transistors organiques à effet de champ, dans la configuration « bottom gate – top contact », ont été fabriqués pour explorer les propriétés de transport de porteurs de charge et l'électroluminescence des couches minces de tétracène déposées sur les différents substrats diélectriques organiques. L'utilisation des couches diélectriques organiques conduit à des valeurs de mobilité des porteurs de charge sensiblement différentes, variant entre $1 \cdot 10^{-2}$ et $2 \cdot 10^{-1}$ $cm^2V^{-1}s^{-1}$, la valeur la plus élevée étant celle des couches déposées sur du polystyrène.

Le prolongement naturel de ce travail est d'établir une corrélation entre le transport de charge, l'émission de lumière et la morphologie/structure des couches organiques pour applications dans les OLEFETs.

ABSTRACT

Over the last three decades, thin films of organic semiconductors (OS) have been the object of intense research. These films can be used in a wide variety of new-generation optoelectronic devices, such as Organic Light Emitting Diodes (OLED), Organic Field Effect Transistors (OFET) and photovoltaic cells. Recently, vacuum sublimed tetracene films were used to realize the first Organic Light Emitting Field Effect Transistor (OLEFET), which integrates in a single device the current modulation function of a FET with the light generation capability of a LED.

The demonstration of OLEFETs is not straightforward. First of all, an efficient integration of optical and electronic functionalities requires the use of a semiconductor with both efficient electroluminescence and good charge transport properties. Secondly, an ambipolar charge transport has to be achieved to produce high performance OLEFETs. Within this context, controlling the dielectric substrate surface chemistry has proven to be an efficient strategy, since it contributes to avoid the suppression of the electron transport induced by the electronic trap states at the dielectric/semiconductor interface. At the same time, the modification of the chemical and physical nature of the dielectric substrate influences the morphology/structure of the organic thin-films, in turn influencing the final device performance.

In this work, polycrystalline tetracene thin films – to be incorporated in OLEFETs – were vacuum sublimed on different organic dielectric substrates, including polymers (parylene C, polymethylmethacrylate, polystyrene) and self-assembled monolayers of hexamethyldisilazane (HMDS) and octadecyltrichlorosilane (OTS). The scope of the work was indeed to shed light on the role of the organic dielectric surface in influencing the charge transport properties of tetracene OLEFETs.

The tetracene deposition rate was 3.5 Å/s, the substrates were kept at room temperature and the pressure inside the vacuum chamber was 2.5×10^{-6} Torr.

The growth process was studied from sub-monolayer to complete coverage by means of ex-situ Atomic Force Microscopy (AFM). The nucleation density, the grain size and the connectivity between the grains were observed to be strongly dependent on the physical and chemical properties of the dielectric substrate surface.

Thin-film transistors, in the bottom gate – top contact configuration, were fabricated to explore charge transport and electroluminescence in tetracene films vacuum sublimed on the different organic gate dielectrics. It was found that the use of the organic dielectric layers leads to considerably different values of the charge carrier mobility, ranging between $1 \cdot 10^{-2}$ and $2 \cdot 10^{-1}$ $cm^2V^{-1}s^{-1}$, the highest mobility being observed in the case of polystyrene.

The natural extension of this project is to establish a sound correlation between charge transport, light emission and film morphology/structure in organic thin films for applications in OLEFETs.

CONDENSÉ EN FRANÇAIS

Depuis les années 80, suite à la découverte des propriétés conductrices et semi-conductrices des polymères et des molécules organiques, s'est progressivement développée une nouvelle branche de l'électronique moderne, c'est-à-dire l'« électronique organique ».

L'intérêt pour l'électronique organique est motivée par les avantageuses propriétés de semi-conducteurs organiques, y compris un faible coût, la flexibilité mécanique, les basses températures de processus et la possibilité de les appliquer sur des substrats à large surface flexibles et enroulables. En outre, les propriétés optiques et électroniques de ces matériaux (par exemple le « gap » d'énergie entre la bande de conduction et la bande de valence) peuvent être facilement modifiés par des procédés de synthèse chimique et sont donc facilement adaptable aux besoins spécifiques des différentes applications.

L'utilisation de matières organiques à la place des semi-conducteurs inorganiques typiquement utilisés dans l'industrie microélectronique (par exemple, Si, Ge, GaAs), permet de fabriquer une grande variété de dispositifs optiques et électroniques parmi de processus de dépôt simples et peu coûteux, tels que le dépôt par solution (méthode de la tournette et dépôt par immersion) ou encore parmi une imprimante à jet d'encre. En plus, la flexibilité mécanique et les basses températures de traitement des matériaux moléculaires permettent de fabriquer des circuits électronique et optoélectronique sur des substrats de plastique flexible, enroulable et avec une très élevé extension superficielle.

Outre les produits tels que diodes (OLEDs) et transistors organiques à effet de champ (OFETs), déjà disponibles sur le marché, beaucoup d'autres applications sont à l'étude, comment par exemple des cellules photovoltaïques, des lasers ou des capteurs. Récemment, en 2003, un nouveau type de dispositif a été développé, à savoir le transistor organique à effet de champ émetteur de lumière (OLEFET), qui intègre dans une seule unité la fonction de modulation du courant typique d'un transistor avec la capacité de production de lumière d'une diode électroluminescente. L'OLEFET est intéressant d'un point de vue soit fondamental soit appliqué. Contrairement à l'OLED, qui è caractérise par une géométrie à empilement vertical, l'OLEFET est caractérise par un géométrie plane; ça permet l'accès direct à la surface des couches

organiques parmi des détecteurs optiques, ce qui rend possible l'étude des phénomènes physiques fondamentaux dans les matériaux semi-conducteurs organiques, tels que le transport de charge et l'électroluminescence.

Le premier prototype d'OLEFET utilisait comme matériau active des couches minces poly-cristallines de tétracène, qui font aussi l'objet de ce travail de maîtrise. Le premier OLEFET était caractérisé par un transport de charge unipolaire de type « p », où seulement des charges positives (trous) sont impliqués dans le phénomène de conduction de courant. Par conséquent, la région d'émission de la lumière était localisé à proximité de l'électrode d'injection des porteurs minoritaires (drain) et ça limitait l'efficacité du dispositif, en réduisant la formation et la recombinaison des excitons par un effet de « quenching » induit par le métal de l'électrode (Or).

L'objectif général de ce travail était de donner une réponse à la question si est possible obtenir un transport de charge ambipolaire, c'est-à-dire un transport simultané des électrons et des trous, dans les transistors organiques à effet de champ basés sur des couches minces poly-cristallines de tétracène. L'approche adoptée a été l'ingénierie de la surface diélectrique. L'utilisation des diélectriques organiques, tels que des polymères ou des monocouches moléculaires auto-assemblées, a été démontré être une approche efficace pour obtenir un transport de charge ambipolaire. En fait, le contrôle de la chimie de la surface diélectrique permet de limiter la densité des états électroniques pièges présents à l'interface diélectrique-semiconducteur, qui sont responsable de la suppression du transport des électrons.

L'ambipolarité du dispositif est une propriété fondamentale pour les OLEFETs car permet de déplacer la position de la région de formation/recombinaison des excitons dans le canal du transistor, loin des électrodes, et en conséquence permet d'augmenter l'efficacité d'émission de lumière.

En 2007, Takahashi et al. ont démontré la possibilité de réaliser des transistors à effet de champ ambipolaires en utilisant des monocristaux de tétracène laminés sur des couches diélectriques de poly méthacrylate de méthyle (PMMA) et contactés par des électrodes avec une basse fonction de travail, tels que argent et magnésium; après cette découverte, la recherche de l'ambipolarité dans les couches minces poly-cristallines de tétracène est devenue significative et scientifiquement intéressant.

Pour différentes raisons, qui seront expliqué par la suite, nous n'avons pas pu observer le transport de type « n » (électrons) et cet étude à été focalisé principalement sur les propriétés morphologiques et structurelles des couches minces poly-cristallines de tétracène en corrélation avec la performance des correspondantes transistors organiques.

Les semiconducteurs organiques sont fortement sensibles à l'oxygène et à l'eau présents dans l'atmosphère ambiante, qui peuvent être adsorbé dans le dispositif – s'il n'est pas convenablement encapsulé – et induire la dégradation de leur performance. Per conséquent, a fin d'observer l'ambipolarité, un contrôle rigoureux de l'atmosphère pendant toutes les étapes de la fabrication et caractérisation des dispositifs est obligatoire. En plus, il est nécessaire d'optimiser l'architecture du dispositif, y compris le choix des matériaux pour les électrodes de « source » et « drain ». Ces dernières doivent être choisis attentivement, avec une faible fonction de travail, afin d'empêcher la formation de barrières d'injection pour les électrons entre l'électrode de « drain » et le canal semiconducteur du transistor.

Tous les aspects abordés (surface du substrat diélectrique, influence de l'eau e de l'oxygène, fonction de travail des électrodes métalliques) sont à la fois crucials pour l'observation d'un transport ambipolaire dans les couche minces de tétracène. Présentement, dans nos laboratoires, des difficultés expérimental doivent encore être résolues, comment le (i) développement d'un méthode pour la réalisation/caractérisation complète des dispositifs sous atmosphère inerte et (ii) la réalisation de dispositifs avec des électrodes de « source » et « drain » fabriqués en utilisant de matériaux différents, tels que Au-Mg (ou Au-Ca) respectivement. Seulement après que tous les aspects seront dûment pris en compte, on sera en mesure de donner une réponse claire sur le rôle que l'ingénierie de surface diélectrique joue sur le propriétés de transport de charge et donc on pourra répondre à la question concernant l'ambipolarité.

Le **Chapitre 1** décrit les principes et l'architecture des OFETs et des OLEFETs (section 1.3 et 1.4) et présente plus en détail le but de cette travail de recherche (section 1.5).

Dans ce travail de maîtrise on à étudié les effets de la modification des propriétés chimiques et physiques de la surface diélectrique sur la morphologie/structure de couches minces et leurs effets sur la performance des transistors à effet de champ.

Des couches minces poly-cristallines de tétracène ont été sublimées sous vide sur différents substrats diélectriques organiques, y compris des polymères, tels que parylène C, poly méthacrylate de méthyle (PMMA) et polystyrène (PS), et des monocouches moléculaires auto-assemblées d'hexaméthyldisilazane (HMDS) et octadécyltrichlorosilane (OTS).

L'utilisation de diélectriques organiques influence le processus de croissance, la morphologie et la structure cristalline des couches poly-cristallines et par conséquence aussi leurs propriétés fonctionnelles. Le processus de germination et croissance a été étudié à partir des premières étapes de la croissance jusqu'au recouvrement complet de la surface, au moyen de la microscopie à force atomique (AFM) ex-situ.

L'objectif spécifique de cette étude était d'établir une corrélation entre les propriétés de la surface diélectrique (par exemple l'énergie de surface, la rugosité et la permittivité diélectrique) et le transport de charge. On a également entrepris une étude pour identifier une corrélation entre le mode de croissance, la morphologie des couches minces et la mobilité des porteurs de charge (trous). Pour faire cela, des dispositifs OFETs ont été fabriquées dans la géométrie « bottom gate – top contacts », où les électrodes d'Or ont été déposés directement sur la surface des couches de tétracène en utilisant une technique d'évaporation thermique et des « shadow masks ».

Le **Chapitre 2** décrit les procédures et les techniques expérimentales utilisées pour le dépôt et la caractérisation soit des couches minces de tétracène soit des couches diélectriques organiques (polymères et monocouches moléculaires auto-assemblées). La mesure d'épaisseur des couches de polymères diélectriques a été effectuée par ellipsométrie spectroscopique et profilométrie. La méthode de l'angle de contact a été utilisée pour étudier la nature hydrophobe/hydrophile de la surface diélectrique et pour estimer l'énergie libre de surface.

La technique expérimentale plus largement utilisé a été la microscopie à force le atomique (AFM) avec laquelle il a été possible d'obtenir une pluralité d'informations sur la morphologie des substrats diélectriques et des couches minces de tétracène. Des mesures de diffraction de rayons X ont été aussi conduites au Synchrotron (ELETTRA, Trieste), en utilisant la technique appelée « Grazing Incidence X-Ray Diffraction » qui permette de caractériser la structure et la

texture de couches minces organique à l'interface entre le diélectrique et le semiconducteur. Le résultats sont actuellement en cours d'élaboration.

Dans le Chapitre 2 on décrit également la procédure adoptée pour la fabrication de dispositifs OFETs et OLEFETs et leur caractérisation électrique. Le point de départ a été un substrat de silicium hautement dopé (résistivité d'environ 0.001-0.005 Ohm·cm) et oxydé thermiquement (épaisseur de l'oxyde de 200 nm), qui peut être convenablement utilisé soit comment substrat soit comment électrode de grille. Les couches diélectriques organiques ont été déposés sur la surface de l'oxyde en utilisant différentes techniques, y compris la méthode de la tournette (PMMA, PS et HMDS), la silanization par phase vapeur (OTS) et la polymérisation par dépôt chimique en phase vapeur (Parylène C).

Les couches minces de tétracène (épaisseur d'environ 50 nm) ont été sublimé sous vide sur le différents substrats diélectriques avec un taux de déposition de 3.5 Å/s. Les substrats ont été maintenus à la température de la pièce et la pression à l'intérieur de la chambre à vide était de 2.5×10^{-6} Torr. En suite, les électrodes d'or ont été évaporés thermiquement (épaisseur de 50 nm et un taux de dépôt de 1 Å/s) sur les couches organiques avec différents géométries (interdigités et à canal unique) et longueurs de canal. Le désavantage principal de cet approche est la petite résolution de la « shadow mask », qui ne permet pas de fabriquer de transistors avec une longueur de canal plus petite que 50 µm.

Le **Chapitre 3** est dédié à la présentation et à la discussion des résultats expérimentaux. La première partie du chapitre (section 3.1) présente les résultats de l'étude de germination et croissance et les propriétés morphologiques des couches de tétracène déposées sur les différentes surfaces diélectriques. On a déposé des couches avec différents épaisseurs nominales (2, 5, 10, 17, 35 et 50 nm) qui en suite on été caractérisée par la microscopie à force atomique (AFM). On a identifié trois phases distinctes: (i) le début de la croissance (germination), (ii) le développement et la coalescence des îles, (iii) le recouvrement complet de la surface. La première observation à été le fait que la densité de nucléation, la forme des grains cristallins et leur inter-connectivité dépendent fortement des propriétés physiques et chimiques de la surface diélectrique.

La deuxième partie du chapitre (section 3.2) présente les résultats de caractérisation électrique des OFETs et montre les courbes de « output » et de « transfer » des dispositifs à canal unique fabriqués sur tous le différents substrats diélectriques.

On a réussi à fabriquer des transistor de tétracène de type « p », en employant tous cinq les couches diélectriques organiques (PMMA, PS, Parylene C, OTS, PMMA) et on rapporte les principaux facteurs de mérite, y compris la mobilité μ_{FET} des porteurs de charge (trous), la tension de seuil V_T et le rapport entre le courant de ON et le courant de OFF (I_{ON}/I_{OFF}).

La mobilité des trous dépende significativement des propriétés de la surface diélectriques et varie dans une plage de valeurs plus large qu'un ordre de grandeur, entre $1 \cdot 10^{-2}$ $cm^2V^{-1}s^{-1}$ (sur SiO_2 non traité) et $2 \cdot 10^{-1}$ $cm^2V^{-1}s^{-1}$ (sur PS). La valeur de mobilité obtenue dans le cas des couches minces des tétracène déposé sur PS est le plus élevé rapporté dans la littérature jusqu'au présent pour ce type de matériau. De meilleurs résultats sont attendus en ayant à disposition un système d'évaporation avec une pression de l'ordre de $10^{-8} \div 10^{-7}$ Torr et parmi une soignée purification du matériau source.

Dans la troisième partie (section 3.3) on discute et analyse les données présentées dans les deux sections précédentes afin de établir le rôle joué par les propriétés de la surface diélectriques dans la détermination des propriétés de transport de charge dans les couches minces de tétracène. Enfin, la dernière partie du chapitre (section 3.4) concerne la caractérisation des OLEFETs en tétracène et la mesure de l'électroluminescence.

L'énergie de surface du substrat diélectrique a été observée jouer un rôle significatif dans la détermination de la densité et de la forme des îles de tétracène.

Le substrat avec la plus faible énergie de surface, OTS, présenté la plus élevé densité d'îles tridimensionnelles. Nous avons observé que le traitement de la surface de SiO_2 avec OTS favorise la nucléation à l'interface conduisant ainsi à une meilleur couverture de la surface du substrat. Cependant, la forme hautement tridimensionnelle des îles de tétracène sur OTS peut induire la formation de remarquables « grain boundaries » pendant la coalescence, ce qui n'est pas favorable pour le transport de charge dans le canal du transistor. Le compromis entre ces deux aspects pourrait expliquer l'augmentation modérée de mobilité des trous associés au

traitement OTS de la surface de l'oxyde de silicium (~$2.0 \cdot 10^{-2}$ $cm^2V^{-1}s^{-1}$ sur OTS vs. ~$1.0 \cdot 10^{-2}$ $cm^2V^{-1}s^{-1}$ sur SiO_2)

Les couches de tétracène sur HMDS montrent des îles plat et grandes qui se développent selon un schéma similaire à un mode de croissance « couche par couche ». Cela devrait générer des grains cristallins grandes et bien reliées les uns aux autres proche à l'interface entre le diélectrique et le semiconducteur, c'est-à-dire là où le transport de charge se produit. La mobilité des trous sur HMDS est seulement modérément plus élevé (~$2.6 \cdot 10^{-2}$ $cm^2V^{-1}s^{-1}$) car des évidentes effets de stress (« bias stress effects ») limitent la performances du dispositifs.

La mobilité des trous dans les couches de tétracène sur PMMA (~$1.8 \cdot 10^{-2}$ $cm^2V^{-1}s^{-1}$) est significativement inférieur si comparée au parylène C (~$6.5 \cdot 10^{-2}$ $cm^2V^{-1}s^{-1}$) et PS (~$2 \cdot 10^{-1}$ $cm^2V^{-1}s^{-1}$). On a observé que la taille moyenne des grains de tétracène sur PMMA est nettement plus petit par rapport aux autres couches diélectriques (section 3.3).

Le couches de tétracène sur PS présente une faible rugosité et la couverture complète de la surface du substrat à été observe avec seulement 10 nm d'épaisseur nominale. Les îles paraissent homogènes dans leurs formes et bien serrés les uns aux autres. En plus, à partir des premières monocouches, les grains sont bien interconnecté et ordonné, ce qui représente une possible raison pour l'haute valeur de mobilité obtenu pour le tétracène sur PS.

L'élaboration des données des mesures GIXRD permettront de étudier la possibilité d'une corrélation entre le transport de charge, la performance du dispositif et la structure/texture des couches minces à l'interface diélectrique/semiconducteur.

On dit à plusieurs reprises que les propriétés de la couche diélectrique, tels que la chimie de surface, la rugosité RMS et la permittivité diélectrique, influencent directement les propriétés fonctionnels des couches. Un exemple est donné à la section 3.3, lorsqu'on traite avec le rôle de la permittivité diélectrique en influençant la mobilité des porteurs de charge. Nos résultats sur les couches des tétracène déposés sur les polymères diélectriques semblent confirmer le modèle présenté par Veres et collaborateurs: matériaux diélectriques avec une forte permittivité (ou constant diélectrique), même si avantageux pour la réduction des voltages opérationnels, produisent des mobilités plus faible. À ce propos il convient de noter que parmi les couches diélectriques utilisés dans ce projet de recherche, PS avait le plus faible constante diélectrique.

Un autre aspect qui joue un rôle significatif pour déterminer la performance de l'OFET, est la pureté chimique de la surface du diélectrique. En fait, dans le cas de couches diélectriques déposées par solution, des traces résiduelles de solvants ou de contaminants chimiques, peuvent affecter la performance du dispositif en générant des états électroniques pièges, comment observé dans le cas du HMDS.

Dans ce contexte, il est intéressant de noter que les OFETs qui emploient parylène C comment couche diélectrique (déposé en phase vapeur) montrent la plus petite variabilité en termes de tension de seuil et mobilité.

Nos procédures expérimentales n'ont pas conduit à l'observation de transport ambipolaire. Des travaux sont en cours pour concevoir une procédure de fabrication/caractérisation des dispositifs conduite entièrement sous atmosphère inerte, sans exposer les substrats à l'air ambiante après le dépôt de la couche diélectrique organique. Cela permettrait de limiter l'adsorption de l'oxygène et de l'eau à l'interface semiconducteur/diélectrique.

L'électroluminescence n'a pas été détecté dans les OLEFETs de tétracène employant la géométrie « bottom gate – top contact ». Ce résultat est probablement lié à l'élevé distance inter-électrodes typique de transistors où les électrodes de source et drain sont fabriqués parmi des « shadow masks ». D'autres stratégies seront examinées dans un proche avenir pour fabriquer des « shadow masks » avec une meilleure résolution, comment « micro-photo-electroforming » et aussi des masques réalisées au moyen de la gravure physique d'une côté à l'autre d'une plaquette de silicium.

En utilisant des dispositifs dans la géométrie « bottom gate – top contacts » n'a pas été possible d'observer aucune émission de lumière, malgré l'utilisation des électrodes interdigités (W = 48.6 mm et L = 100 microns), caractérisé par une densité de courant élevée et conséquemment par une majeure probabilité de formation/recombinaison des électrons.

Au contraire, en utilisant la géométrie « bottom gate – bottom contacts », avec une plus petite distance entre les électrodes (L = 6 μm), il a été possible d'observer l'émission de lumière à proximité de l'électrode de « drain » (transport unipolaire), ce qui confirme que le système expérimental, construit ad hoc pour la caractérisation de transistors émetteurs de lumière, fonctionne correctement et ne limite pas l'évaluation de leurs propriétés.

TABLE OF CONTENTS

LIST OF TABLES

LIST OF FIGURES

LIST OF ABBREVIATIONS

AFM	Atomic Force Microscopy
AM	Amplitude Modulation
AMLCD	Active Matrix Liquid Crystals Display
CVD	Chemical Vapor Deposition
DOS	Density of States
F8T2	Poly-9,9’ dioctyl-fluorene-co-bithiophene
FET	Field Effect Transistor
FFT	Fast Fourier Transform
FM	Frequency Modulation
HMDS	Hexamethyldisilazane
HOMO	Highest Occupied Molecular Orbital
LUMO	Lowest Unoccupied Molecular Orbital
MEMS	Micro-Electro-Mechanical System
MOSFET	Metal Oxide Semiconductor Field Effect Transistor
MSE	Mean Square Error
OLEFET	Organic Light Emitting Field Effect Transistor
OLED	Organic Light Emitting Diode
OFET	Organic Field Effect Transistor
OS	Organic Semiconductor
OTFT	Organic Thin Film Transistor
OTS	Octadecylthrichlorosilane
P3HT	Poly (3-Hexylthiophene)

PARY-C	Poly(monochloro-p-xyllyene)
PDS	Parylene Deposition System
PMMA	Polymethylmethacrylate
PPV	Poly(*p*-phenylene vinylene)
PS	Polystyrene
PSD	Power Spectral Density
PVD	Physical Vapor Deposition
QCM	Quartz Crystal Microbalance
RMS	Root Mean Square
RFID	Radio Frequency Identification
SAM	Self Assembled Monolayer
SCA	Single Curve Analysis
SPM	Scanning Probe Microscopy
STM	Scanning Tunnelling Microscopy
TLM	Transfer Line Method
UHV	Ultra High Vacuum

Chapter 1. INTRODUCTION

1.1 Historical perspective and motivation

It has long been a widespread idea that organic materials are electrical insulators. In 1977 A. J. Heeger, A. G. MacDiarmid and H. Shirakawa, discovered that the electrical conductivity of polyacetylene could be dramatically increased (up to eleven orders of magnitude) by chemical doping and showed to the world the possibility to synthesize conducting plastics [1-2]. For this discovery, they were awarded the Nobel Prize for Chemistry in 2000. It represented a breakthrough in the field of organic materials and marked the beginning of a new research field focused on electrically conducting organic polymers and molecules.

After this discovery, scientists were mainly interested in polymers with "metallic" behavior and hence little research was carried out on the semiconducting properties of organic polymers and molecules. From the historical point of view, the first investigations of Organic Semiconductor (OS) molecules date back to the beginning of the 20^{th} century, as witnessed by the pioneering works of the Italian scientist A. Pochettino [3], who discovered and studied the photoconduction mechanism in crystals of anthracene. Electroluminescence and photovoltaic effects in π-conjugated small molecules and polymers, where the molecular structure is characterized by the presence of alternate single and double bonds, were demonstrated by the half of the century [4]. For the first time in 1964 a field-dependent electrical conduction was observed in thin films of phthalocyanines [5]. However, until the late 1980s, research on OSs was far from being satisfactory and no practical applications were demonstrated.

An important step occurred in 1986, when Koezuka and Tsumura demonstrated the first Organic Field Effect Transistor (OFET) based on an electrochemically polymerized polythiophene thin-film [6]. This demonstration opened the possibility to fabricate organic electronic circuits and started the era of "organic electronics", enabling for a series of significant technological applications, such as flexible field-driven displays, logic circuits, chemical and mechanical sensors, image sensing devices and Radio Frequency Identification (RFID) tags [7].

Nowadays, a number of OS, both polymers and small molecules, have been synthesized and commercialized [8] and new OFET architectures have been designed to exploit the functionalities of these materials.

The great interest in organic electronics is motivated by the unique characteristics of OSs, such as the possibility to conveniently tailor their optoelectronic properties (e.g. optical band gap) by means of chemical synthesis, low-cost processing, compatibility with flexible plastic substrates and biocompatibility [9]. Differently from the conventional inorganic semiconductors employed in the electronic industry, OSs do not necessarily require any expensive under-vacuum and high-temperature processes but can be deposited with low-cost methods, such as solution cast, inkjet and micro-contact printing [10]. The mechanical flexibility of organic materials and their low processing temperature allow for using low-cost and flexible substrates, such as glasses, plastics and metal foils [11]. In turn, this enables for fabricating large-area/roll-up displays (e.g. electronic newspaper) and photovoltaic panels.

Since the first devices – characterized by a mobility of 10^{-5} $cm^2V^{-1}s^{-1}$ – OFETs have known an extraordinary increase in mobility (more than six orders of magnitude), as shown in Figure 1.1.

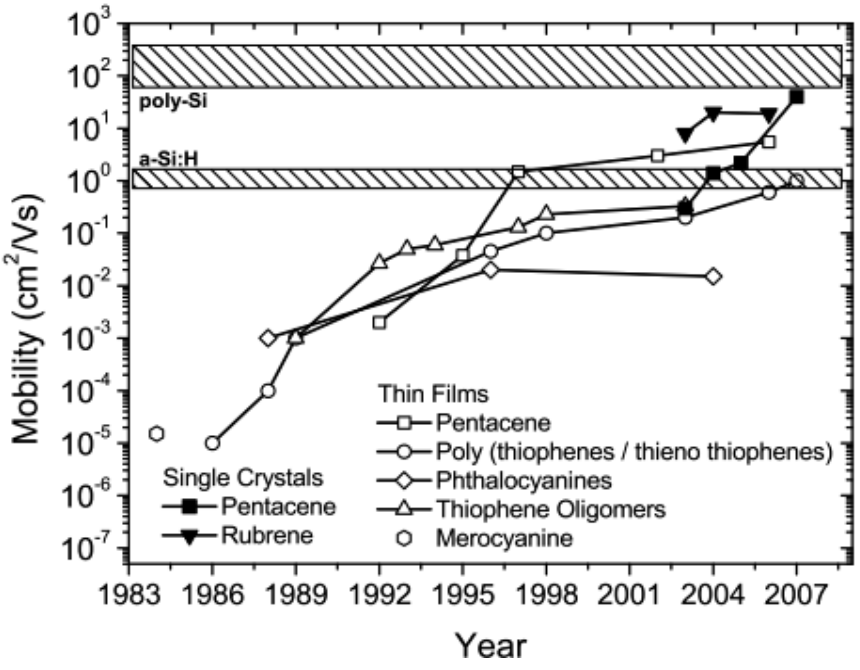

Figure 1.1 – P-type OFET mobility in organic thin films and single crystals, during the last three decades. Extracted from reference [12].

Hence, nowadays, the OFET technology is mature enough to compete with amorphous and polycrystalline silicon (a-Si:H and poly-Si) technologies, e.g. in Active Matrix Liquid Crystals Displays (AMLCD) backplanes. However, as pointed out in [13], organic electronics will never replace the well established Si electronics, which will continue to keep a dominant role in the microprocessor industry. The charge carrier mobility in single crystals of the most common inorganic semiconductors (Si, Ge, GaAs), is at least three orders of magnitude larger than in the best performing OS. Instead of this, organic electronics is expected to complement and extend it in applications where high switching speed is not a requirement and where low costs, biocompatibility, large and flexible substrates represent a priority.

Beyond OFETs, which are devices used to switch and modulate electronic signals, current research in organic electronics includes light-emitting devices, such as Organic Light Emitting Diodes (OLEDs) and photo-absorption devices, such as solar cells and photodetectors. In 2003, a new class of organic devices has been demonstrated, i.e. Organic Light Emitting Field Effect Transistors (OLEFETs) which represent the smallest possible integration of the light emission function of the OLED with the current modulation function of the OFET [14].

OLEFETs are interesting from a technological standpoint, due to the many applications envisaged, such as active matrix full-color displays, optical communication devices, solid-state lighting and ultimately organic injection lasers [9, 15]. Moreover, due to their planar geometry (see Section 1.4), as opposite to the vertically stacked geometry of OLEDs, they offer direct access to optical probes thus opening the possibility for investigating fundamental processes in OSs, such as excitons formation, recombination and light emission [15]. High-performance OLEFETs have been recently demonstrated with an efficiency higher than the equivalent OLEDs [16], suggesting that the promises related to this technology are not far from becoming reality.

However, much work is left to do to fully understand the aspects that influence the performance of OLEFETs. This project aims to shed light on the role of the dielectric surface (Section 1.3 and Section 1.4) in influencing the charge transport properties of organic thin films to be incorporated in OLEFETs.

1.2 Organic semiconductors: an overview

OSs are carbon based polymers and small molecules where adjacent carbon atoms are linked together by alternate single and double bonds. The carbon atoms of an OS are hybridized in the sp^2 configuration, as shown in Figure 1.2. The σ-bonds, formed by the overlap of the sp^2 orbitals of two adjacent carbon atoms, constitute the backbone of the molecule. On the other hand, the π-bonds result from the overlap of the p_z orbitals of two adjacent carbon atoms and are weaker than the σ bonds. The p_z orbitals of all the carbon atoms in the OS combine to form a delocalized electronic orbital spread over the entire backbone of the molecule. The resulting electronic structure is referred to as a π-conjugated electronic system, which is peculiar to all OSs, both polymers and small molecules [17].

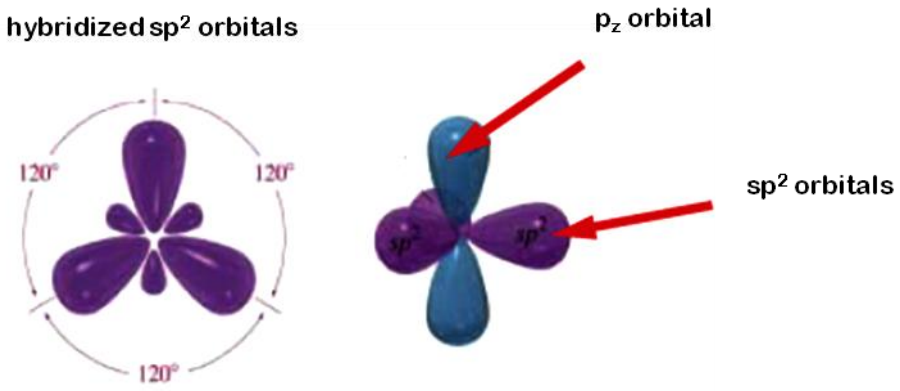

Figure 1.2 – sp^2 hybridization of a carbon atom. (Left) In-plane arrangement of the sp^2 orbitals; (right) three dimensional representation of the sp^2 and p_z orbitals.

Small molecules can form single crystals and thin films and are commonly deposited by Physical Vapor Deposition (PVD) techniques. Polymers, on the other hand, can be deposited only in the form of thin films, by the use of solution processing techniques. This stems from the fact that thermal evaporation induces their degradation.

The electronic structure of all OSs is characterized by the presence of a relatively large energy gap (usually 2 - 3 eV [18]) between the energies of two molecular orbitals, the Highest Occupied Molecular Orbital (HOMO) and of the Lowest Unoccupied Molecular Orbital (LUMO). These are analogous to the edges of the valence and conduction band respectively of conventional inorganic semiconductors [19].

Thin films and single crystals of OSs are often investigated as active materials in Field Effect Transistors (FET), which provide a straightforward configuration to study their charge transport properties [18]. Several OSs, when incorporated in OFETs (see Section 1.3), show accumulation of positive charges (holes) in the transistor channel upon application of a negative gate bias. The opposite process, i.e. accumulation of negative charges (electrons) upon application of a positive gate bias, is less frequently observed [19]. When holes are accumulated and transported inside the transistor channel, the OS is referred to as "p-type". On the other hand, when electrons are accumulated and transported, the OS is referred to as "n-type".

Nowadays, several high-performance p-type OSs are commercially available, but the same is not true for the n-type counterpart. The development of high-performance n-type materials is challenging [8] and it is regarded as the key step towards the fabrication of complementary transistor circuits (CMOS-type), for application in organic digital electronics [19].

The "type" of an OS depends on its chemical structure, so that chemical synthesis processes have been intensively studied to develop new p-type and n-type materials starting from pre-existing OSs. For example, from a common core unit, such as a thiophenes oligomer, it is possible to obtain both p-type and n-type materials by adding electron-accepting or electron-donating groups, as reported in reference [20].

The possibility for n-type or p-type conduction does not depend only on the chemical structure of the OS but also on other aspects related to both the semiconductor deposition/processing conditions and the device architecture/components (we refer to Section 1.3 for the description of the OFET). It is known that the source and drain electrodes materials as well as the dielectric layer surface chemistry play a crucial role in establishing a p-type or n-type transport. As pointed out in [8, 18], one should not refer to an OS as p-type or n-type, but rather should apply this classification to the transistor channel.

A key step in the knowledge of OSs and related devices was taken in 2005, when Chua et al. proved that the use of hydroxyl free gate dielectrics – instead of the commonly employed SiO_2 dielectric – enabled the n-type transport in a number of polymeric OSs that were previously believed to be exclusively p-type [21]. This discovery paved the way towards the observation of n-type transport at first in a number of semiconducting polymers and afterward in small molecules [22], seeming to confirm the hypothesis that organic semiconductors are in principle

"intrinsically ambipolar", i.e. capable to transport – under specific device configurations and processing conditions – both electrons and holes [18]. Reasons for the commonly observed n-type conduction suppression were individuated in the electron trapping mechanisms associated to the silanol groups present on the SiO_2 surface. Recently, it was shown that the electron transport suppression is more in general induced by an electrochemical charge transfer processes between the semiconducting channel and the red-ox couple system of an adsorbed water/oxygen layer [23]. The adsorption of the oxygen/water layer is favored by the presence of hydrophilic groups (e.g. silanols) on the dielectric substrate surface. It can be limited by hydrophobic groups, such as for example polymer layers and Self Assembled Monolayers (e.g. octadecyltrichlorosilane, OTS).

Ambipolarity is a critical property from a technological standpoint, for the fabrication of complementary transistor circuits based on a single organic semiconducting material. This would imply the possibility to conveniently fabricate logic gates without the requirement to pattern two different OSs. Moreover, ambipolarity is a fundamental property for the realization of high-performance OLEFETs, where efficient light emission is possible only if excitons (bound electron-hole pairs) are formed inside the transistor channel, far from metal electrodes.

In the following sections we introduce the architecture and the working principle of OFETs (Section 1.3) and OLEFETs (Section 1.4), which are the devices under study in this research project.

1.3 Organic Field-Effect Transistors

Organic Field Effect Transistors (OFETs) are devices constituted by five distinct components. A gate electrode (i) is separated from the active OS (ii) by the gate dielectric (iii). In bottom gate transistors, schematically represented in Figure 1.3, the source (iv) and drain (v) electrodes can be positioned either on top of the OS (top contacts, Figure 1.3a) or on the gate dielectric (bottom contacts, Figure 1.3b).

In OFETs, the transistor channel is located at the interface between the dielectric layer and the OS and extends only for a few nanometers in the direction orthogonal to the interface [24]. For this reason, the bottom contact geometry is referred to as "coplanar", in the sense that both the electrodes and the transistor channel lie on the same plane. On the contrary, the top contact

geometry is referred to as “staggered”, since the source and drain electrodes do not contact directly the transistor channel but lie above it [25].

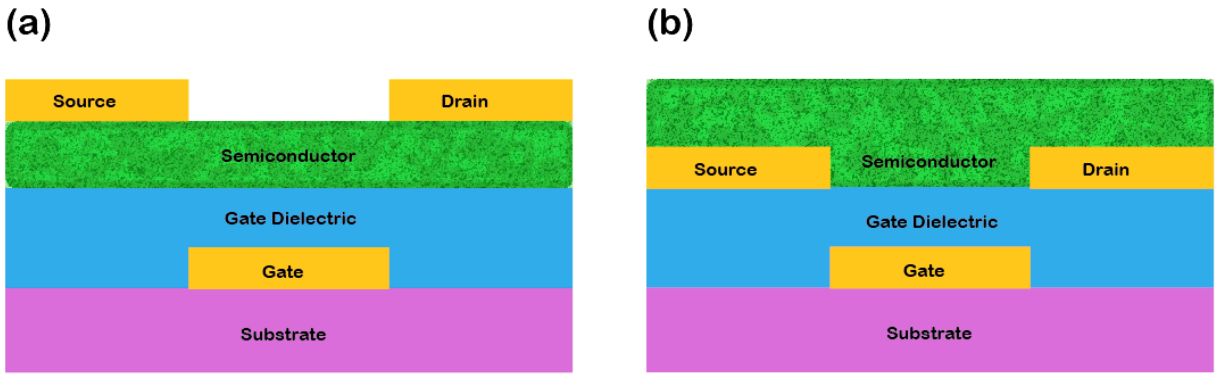

Figure 1.3 – Bottom gate OFET architectures: (a) top contact and (b) bottom contact geometry.

The geometry of the transistor channel is characterized by the inter-electrode distance L and the electrode width W, as represented in Figure 1.4.

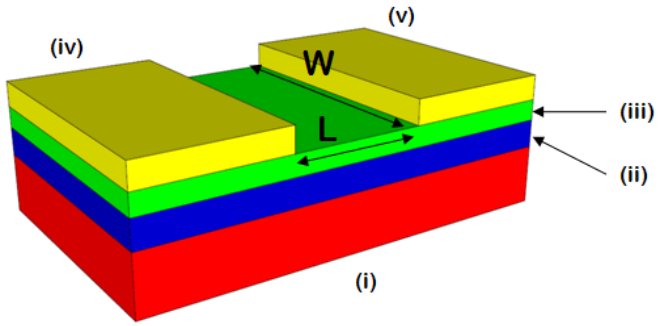

Figure 1.4 – Schematic illustration of the transistor channel geometry in the case of a top-contact OFET, employing the substrate as the gate electrode. See text for definition of symbols.

The working mechanism of OFETs can be described by means of the long-channel silicon device model [7, 26], that is based on the gradual channel approximation. This requires that the electric field induced by the gate electrode in the direction orthogonal to the current flow is much larger than the electric field induced by the source and drain electrodes in the direction parallel to the current flow. This condition is generally satisfied when the channel length L is much larger than the thickness of the insulating layer t_i ($L > 10 \cdot t_i$) [18] and is essential for having OFETs with current-voltage characteristics that could be described by the equations of the long-channel silicon device model (vide infra). Only under this condition it is possible to extract the correct

field effect mobility μ, which represents the charge carrier drift velocity per unit of electric field strength. The model requires also that the charge carrier mobility is constant over all the transistor channel.

OFETs work in accumulation mode and therefore the polarity of the transistor channel is the same as the polarity of the majority carriers in the OS. In addition, it is not possible to define the threshold voltage (V_{th}), similarly to the case of MOSFETs, as the gate voltage necessary to achieve the inversion regime [26]. In OFETs there is not a depletion layer and thus, ideally, the threshold voltage should be zero [27]. However, this condition is never satisfied and a non vanishing voltage has to be applied to the gate to induce a significant current flow between the source and drain electrodes. As pointed out in [7], in the context of OFETs there is not a unique and rigorous definition of threshold voltage. Generally, the threshold voltage is described as the gate voltage required to achieve the "onset of accumulation".

In the following discussion, we refer to OFETs based on p-type OSs. Basically, an OFET can be regarded as a capacitor where the two plates are (i) the gate electrode and (ii) the OS, separated by the gate dielectric. The source electrode is usually grounded. When a negative voltage V_{GS} is applied between the source and gate electrodes, as in Figure 1.5, mobile charge carriers (holes) are drawn into the transistor channel and are accumulated at the semiconductor/dielectric interface. If a negative voltage V_{DS} is applied between source and drain, an electric current I_{DS} starts to flow between the two electrodes. Under the effect of the V_{DS} bias, the holes injected from the source electrode into the HOMO level of the OS, move towards the drain electrode where they are finally collected.

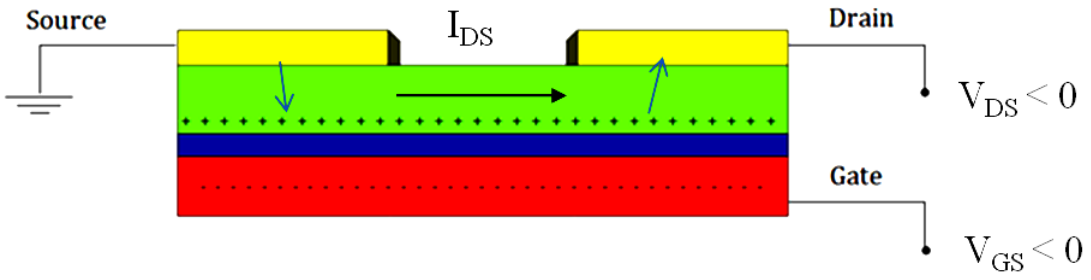

Figure 1.5 – Schematic representation of a p-type OFET working in accumulation mode. (Green) p-type semiconductor; (blue) gate dielectric; (red) gate electrode.

The magnitude of the transistor current flowing between the source and drain electrodes is modulated by the gate voltage V_{GS}. Ideally, with no bias applied to the gate, the current should be nil; however a non vanishing current, (I_{OFF}) is measured in all OFETs.

The long channel silicon device model deals with three different regimes of operation. When the gate voltage is lower than the threshold voltage V_{th}, there are few mobile carriers in the transistor channel and no current flows between the drain an source electrodes. The device is said to be in "cut-off ":

$$I_{DS} \simeq 0 \quad \text{for} \quad V_{GS} < V_{th} \tag{1.1}$$

At small V_{DS} and large V_{GS} the device is in the "linear regime" and the current-voltage relation is given by the following equation.

$$I_{DS}{}^{lin} = \frac{W}{L} C_i \mu \left[(V_{GS} - V_{th}) V_{DS} - \frac{V_{DS}^2}{2} \right] \quad \text{for} \quad V_{DS} < V_{GS} - V_{th} \tag{1.2}$$

where C_i is the capacitance of the gate dielectric. By increasing V_{DS}, a condition can be achieved in which the potential drop between the transistor channel and the gate electrode becomes smaller than the threshold voltage. This condition is satisfied in close proximity to the drain electrode when $V_{DS} = V_{GS} - V_{th}$. The channel becomes "pinched-off " and a region is formed at the "pinch-off" point where no significant concentration of mobile charge carriers are accumulated at the dielectric/semiconductor interface. This limits the rate of current increase and causes the current to saturate [7]. The value of I_{DS} in the "saturation regime" is obtained by evaluating the (1.2) at $V_{DS} = V_{GS} - V_{th}$:

$$I_{DS}{}^{sat} = \frac{W}{2L} C_i \mu (V_{GS} - V_{th})^2 \quad \text{for} \quad V_{DS} > V_{GS} - V_{th} \tag{1.3}$$

The drain-source current I_{DS} can be measured and plotted either by varying the drain-source voltage V_{DS} and keeping constant the gate-source voltage V_{GS} (output curves, Figure 1.6) or by varying V_{GS} and keeping constant V_{DS} (transfer curves, Figure 1.7 and Figure 1.8). An example of output characteristics, obtained from the top-contact tetracene OFETs fabricated in this research project is shown in Figure 1.6.

The figures of merit of OFETs are the threshold voltage V_{th}, the FET mobility μ, the I_{ON}/I_{OFF} ratio, and the sub-threshold slope. The threshold voltage is commonly obtained from the

saturated transfer characteristics (at large constant V_{DS}) as the X-axis intercept of the linear extrapolation of the $\sqrt{|I_{DS}|}$ vs. V_{GS}, as shown in Figure 1.7.

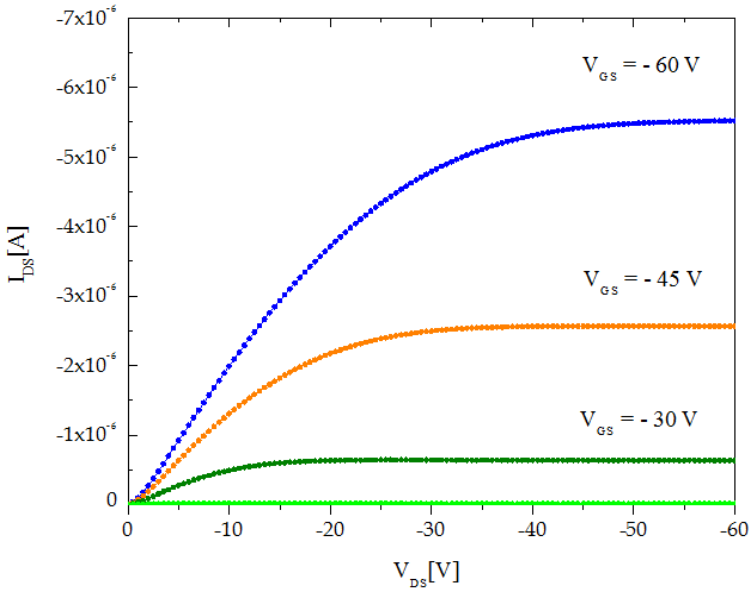

Figure 1.6 – I_{DS} vs. V_{DS} output characteristics of a tetracene-based top-contact OFET for different V_{GS} biases: 0, -15, -30, -45, -60 V.

The mobility is commonly extracted in the saturation regime. In this way, possible non linear effects that may influence the transistor behavior at small drain-source voltages, such as non-ohmic contacts (injection barriers due to the mismatch between the HOMO/LUMO of the OS and the work function of the electrode), do not affect the mobility measurement.

The FET mobility μ is calculated using the following formula, which is derived from the (1.3):

$$\mu = \frac{2L}{WC_i}\left(\frac{\delta\sqrt{I_{DS}}}{\delta V_{GS}}\right)^2_{V_{DS}=\text{const}>V_{GS}-V_{th}} \qquad (1.4)$$

where $\left(\frac{\delta\sqrt{I_{DS}}}{\delta V_{GS}}\right)$ is the slope of the linear extrapolation of the $\sqrt{|I_{DS}|}$ vs. V_{GS} plot (Figure 1.7).

The sub-threshold slope is obtained from the saturated transfer characteristics and is defined as the inverse slope of the $\log(|I_{DS}|)$ vs. V_{GS} curve at large constant V_{DS}, as indicated in Figure 1.8. The sub-threshold slope is related to the device switching speed: the smaller the sub-threshold slope, the faster the transition between the ON and the OFF states. Typical values of the sub-threshold slope for the tetracene OFETs fabricated in this project are in the range 1-3 V/dec.

I_{ON}/I_{OFF} is defined as the ratio between the maximum current in the ON state (I_{ON}) and the minimum current in the cut-off regime (I_{OFF}). It is evaluated from the saturated transfer characteristics at large constant V_{DS}, as shown in Figure 1.8. The tetracene OFETs fabricated in this research project had a I_{ON}/I_{OFF} value included in the range $10^5 – 10^6$.

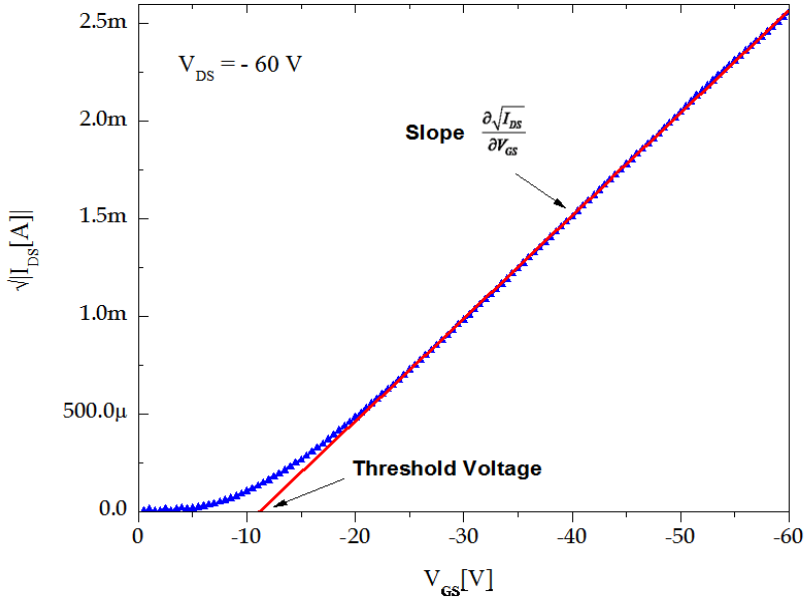

Figure 1.7 – $\sqrt{|I_{DS}|}$ vs. V_{GS} plot of a tetracene OFET. V_{DS} is biased at -60 V.

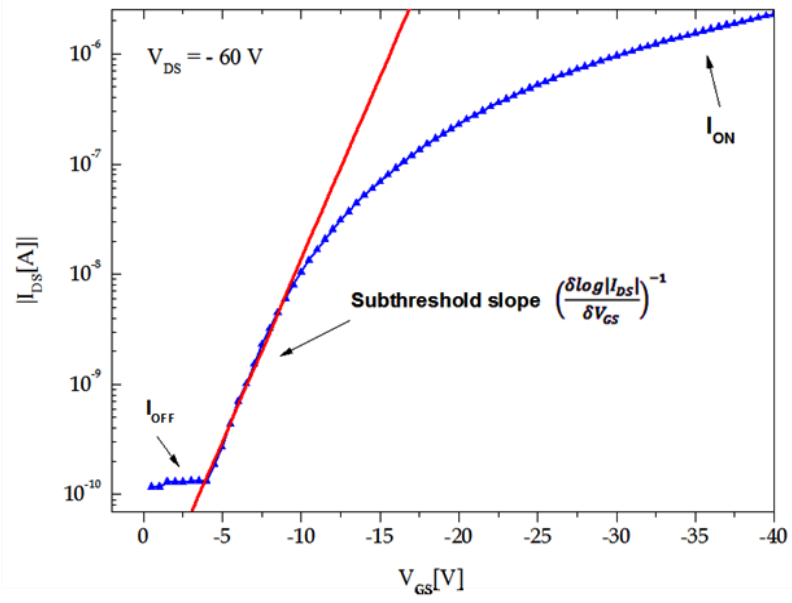

Figure 1.8 – $|I_{DS}|$ vs.V_{GS} transfer characteristics of a tetracene OFET. V_{DS} is biased at -60 V.

1.4 Organic Light Emitting Field Effect Transistors

OLEFETs, whose structure and working principle are shown in Figure 1.9, integrate the switching function of the transistor with light emission and are attractive for both fundamental studies and technological applications. Differently from OLEDs, where the OS is sandwiched between the anode and cathode electrodes, the planar geometry of the OLEFET offers direct access to optical probes and permits a direct imaging of the electroluminescence generated by the OS. Hence, OLEFETs can be conveniently used as test systems to investigate fundamental physical processes in OSs, as mentioned in Section 1.1. The OLEFET of Figure 1.8 corresponds to a bottom gate – bottom contact OFET, where the organic semiconducting film is deposited on substrates with pre-patterned source and drain electrodes.

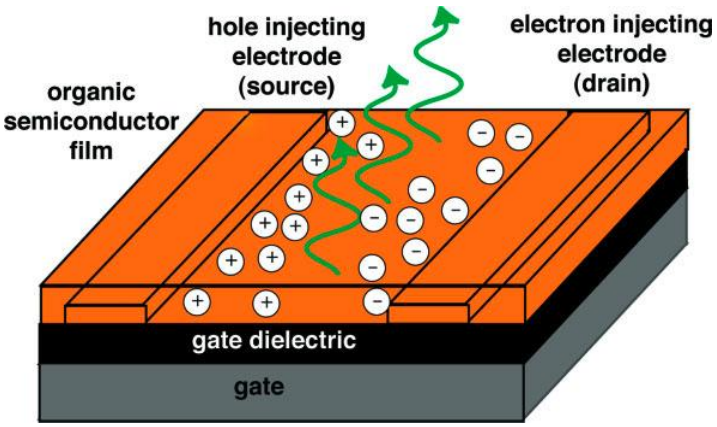

Figure 1.9 – Architecture and working principle of a bottom-contact OLEFET (see text for details). Extracted from reference [9].

Notice that other OLEFET geometries are possible, among which the bottom gate – top contact (Figure 1.3a) geometry is among the most commonly employed (e.g. [16]), since it allows for an ad hoc preparation/treatment of the dielectric substrates surface. For the same reason, a bottom gate – top contact architecture was employed in the context of this research project.

The working mechanism of an OLEFET stems from that of the corresponding OFET (Section 1.3). When an appropriate bias V_{GS} is applied to the gate, holes and electrons are injected from the source and the drain and are accumulated in the transistor channel, where they move under the action of a drain-source bias (V_{DS}). If the OS is electroluminescent, holes and electrons form

excitons that recombine radiatively and generate light. The current (I_{DS}) flowing between source and drain and the intensity of the light emitted from the OLEFET are modulated by V_{GS}, which is also used to switch the device between the OFF (dark) and the ON state (light). Hence, OLEFETs can be indeed regarded as self-driven light-emitting devices.

The first OLEFETs were based on unipolar OSs, but their efficiency was low due to the localization of the light emission region in the proximity of the minority charge carrier-injecting metal electrode, which causes light emission quenching. Nowadays, high efficiency OLEFETs based on ambipolar materials have been demonstrated: the light emission region can be moved far from the metal electrodes; the position inside the transistor channel where excitons form and recombine, can be easily controlled by varying the gate voltage V_{GS} and the drain-source voltage V_{DS} [28]. This allows limiting metal quenching effects and thus improving the light emission efficiency.

1.5 Tetracene-based OLEFETs

The first prototype of OLEFET was based on polycrystalline films of tetracene, a π-conjugated small molecule constituted by four fused benzene rings (Figure 1.10). Tetracene, a commercially available p-type OS, is characterized by both good charge transport properties and relatively high fluorescence quantum yield [29]. The hole mobility can be as high as 2.4 and 0.1 $cm^2V^{-1}s^{-1}$ in single crystals and polycrystalline films, respectively [30-31].

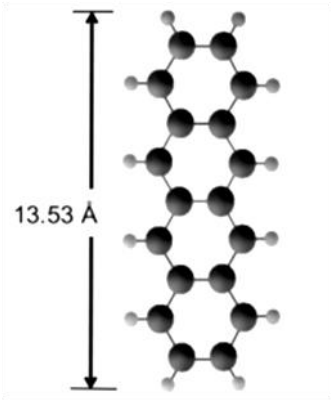

Figure 1.10 – Structure of the tetracene molecule. (Dark grey) Carbon atoms. (Light grey) Hydrogen atoms. Extracted from reference [32].

Light-emission in OLEFETs based on tetracene films occurs in the vicinity of the negatively biased drain electrode. When gold is employed as the source/drain electrode material, a high energy barrier is formed at the drain, (Figure 1.11 [4]) and makes the injection of electrons from the metal electrode into the LUMO level of tetracene strongly unfavorable. Nevertheless, electrons are injected into the OS, as witnessed by the light-emission observed close to the drain electrode (a photograph of a working device is reported in Figure 3.22). Mechanisms for electron injection have been proposed in [33]: electrons would be injected into the LUMO level of tetracene via tunneling through the energy barrier.

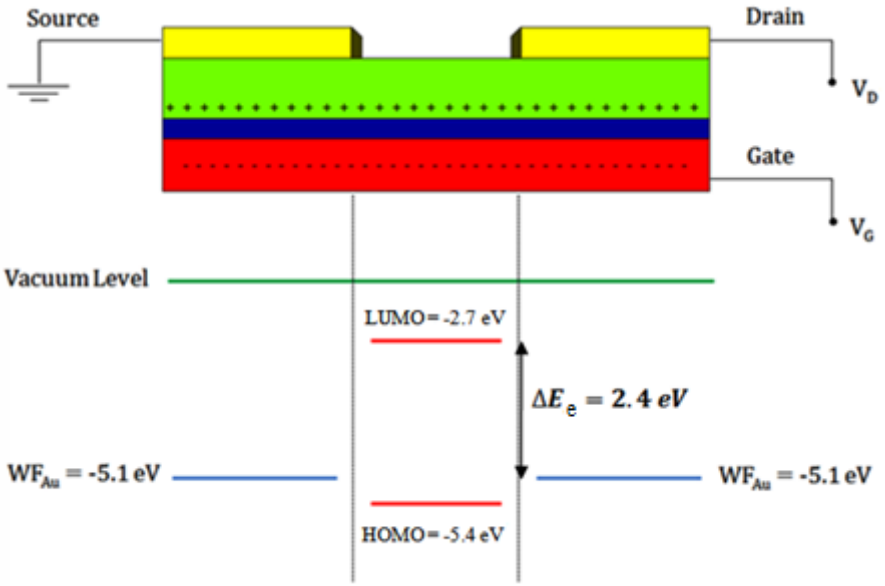

Figure 1.11 – Schematic representation of the energy levels of tetracene (HOMO and LUMO) [4] and the gold work function (WF_{Au}). The device scheme of the tetracene FET is also presented.

However, the injected electrons are not transported inside the transistor channel, so that the formation and recombination of excitons occurs with significant probability only in the proximity of the drain electrode. Hence, metal quenching effects are responsible for limiting the efficiency of light emission. The electroluminescence signal from these devices is weak, so that appropriate optical probes (e.g. a pre-amplified photomultiplier in combination with an integrating sphere [33]) are required to detect the emission of photons from the active material. A commonly adopted strategy consists in fabricating OLEFETs with interdigitated electrodes, i.e. characterized

by a high W/L ratio. This allows increasing the magnitude of the current flow (Equations 1.2 and 1.3) and thus the intensity of the light emitted from the device.

A key requirement for improving the efficiency of these devices is represented by the achievement of an ambipolar transport. The possibility to obtain ambipolar tetracene films is not remote. In 2007, Takahashi et al. developed an ambipolar OLFET based on a tetracene single crystal, with hole and electron mobilities up to $1.6 \cdot 10^{-1}$ and $3.7 \cdot 10^{-2}$ $cm^2V^{-1}s^{-1}$ respectively [29]. The activation of the electron transport in tetracene single crystals was made possible by both the use of an organic dielectric layer, i.e. polymethylmethacrylate (PMMA), and by a scrupulous control of the surrounding atmosphere, carefully limiting the exposure to oxygen and moisture. The authors observed that the exposure to ambient air was the principal reason for the suppression of the n-type transport in tetracene single crystals laminated onto PMMA substrates.

It is also worth to note that they fabricated source and drain electrodes with low work function (i.e. air unstable) metals – such as (i) magnesium (drain) and gold (source) or (ii) silver (source, drain) – in order to reduce the energy barriers at the metal/OS interface.

If an ambipolar transport has been achieved for tetracene single crystals laminated on a polymeric dielectric layer, a natural extension of the research is the investigation of the potential ambipolarity of polycrystalline tetracene films deposited on organic dielectric substrates.

1.6 Scope of the work

The scope of this work is providing an answer to the question of whether it is possible to achieve an ambipolar transport (i.e. simultaneous electron and hole transport) in Organic Field Effect Transistors/Organic Light Emitting Field Effect Transistors based on polycrystalline tetracene films, usually showing an exclusive p-type transport, by means of dielectric surface engineering. As already mentioned, achieving ambipolarity in tetracene films is required to achieve efficient tetracene-based Light Emitting Transistors.

The use of hydrophobic polymers and self assembled monolayers (SAM) as gate dielectrics limits the electron trapping phenomena, as mentioned in Section 1.2. This opens the possibility to enable, as reported in the literature for tetracene single crystals laminated on PMMA, n-type transport. The organic gate dielectric investigated will be: (i) octadecyltrichlorosilane (SAM), (ii)

hexamethyldisilazane (SAM), (iii) polymethylmethacrylate, (iv) polystyrene and (v) parylene C. Details on the characteristics of each dielectric material will be given extensively in Section 2.3.

However, due to different reasons (vide infra) we could not prove the possibility of electron transport in the tetracene films and the focus of this study was on the properties of the films in relation to the performance of the OFETs based there on.

It is known that changing the dielectric surface properties strongly impacts the growth and morphology/structure of organic films [34] and ultimately the films' functional properties (e.g. charge carrier transport and electroluminescence). In fact, dielectric substrate surface chemistry, dielectric substrate surface energy, and Root Mean Square (RMS) roughness all play a significant role in determining the films' nucleation and growth process and consequently the films' morphology and structure. Hence, our first objective consists in controlling and optimizing the deposition of polycrystalline tetracene thin films on the different organic dielectric substrates. The goal is depositing films characterized by complete substrate surface coverage, uniformity, and well-interconnected large crystalline grains. As indicated in reference [34], this allows improving the films' charge transport properties. Top-contact OFETs/OLEFETs, employing the mentioned organic gate dielectrics will be fabricated to deduce the charge carrier mobility and to explore its relationship with the films' morphological properties. The establishment of such a relationship will be the second objective to achieve.

It is worth mentioning that a careful control of the surrounding atmosphere during all the steps of OLEFETs/OFETs fabrication and characterization (Section 2.1) is mandatory. An appropriate engineering of the device architecture, including the choice of the source and drain electrode materials, could be required for achieving an efficient electron injection into the transistor channel. All the discussed aspects (dielectric substrate surface, atmosphere, metal electrodes) are both crucial for the possible observation of an ambipolar transport in tetracene thin films. Only after all the aspects will be properly taken into account we will be able to give a clear answer on the role that surface dielectric engineering plays in permitting ambipolar transport in organic thin films.

Chapter 2. EXPERIMENTAL METHODS

This chapter deals with the experimental methods employed to fabricate and characterize tetracene-based Organic Field Effect Transistors (OFETs).

Since the objective of this research project is determining the influence of the dielectric substrate surface on the growth process and structure/morphology of tetracene films to establish a sound correlation with the films' functional properties, a number of experimental methods are required.

Section 2.1 illustrates the fabrication steps used to realize the OFETs. It also describes the set-up and the procedure for device characterization.

Section 2.2 describes the techniques utilized to study the physical properties of the dielectric layers as well as the nucleation and growth process and the morphology of tetracene films. Spectroscopic ellipsometry and profilometry were used to measure the dielectric layer thickness, whereas contact angle goniometry was used to explore the hydrophobic/hydrophilic behavior of the dielectric substrate. Atomic Force Microscopy (AFM) was employed to investigate the morphology of the dielectric substrates and of the overgrown tetracene films.

Not only AFM but also Grazing Incidence X-Ray Diffraction (GIXRD) was used for tetracene film characterization. The former bears information on the morphology of the layer at the nanometer to micrometer scale. The latter provides information on the in-plane crystal structure of the layer, in a portion of the film ranging from a few nanometers to hundreds of nanometers beneath the film surface [35]. The results of the GIXRD investigation will not be discussed in this text since the interpretation of the data is still in progress.

Section 2.3 focuses on the deposition and the characterization of the dielectric layers – polymeric and self assembled monolayers (SAM) – on the SiO_2 substrate surface.

The last two sections describe the thermal evaporation of the tetracene films and of the gold electrodes. More specifically, Section 2.4 deals with the set up and the deposition parameters for tetracene films deposition, whereas Section 2.5 deals with gold electrode deposition and shadow masks design for top contact electrodes patterning.

2.1 Sequential steps in OFETs' fabrication and characterization

Since Organic Semiconductors (OS) can be readily obtained as thin films – e.g. by solution casting or vacuum thermal evaporation – OFETs are commonly designed as Organic Thin-Film Transistors (OTFTs), where the semiconductor is deposited on the gate dielectric [36].

In research laboratories, OFETs are often fabricated starting from a highly doped Si wafer, which can act both as the substrate and the gate electrode. A thin layer of SiO_2 is then thermally grown on the Si wafer to realize the gate dielectric. Reasons for the popularity of this approach can be found in the large commercial availability of high quality thermally oxidized Si substrates and in the possibility to obtain convenient OFET structures by employing standard microfabrication processes.

However, over the past years, the SiO_2 layer has been gradually substituted by organic dielectrics, which have proven to be effective for improving the performance of OFETs.

In this research project, a bilayer approach is employed for the gate dielectric. A thin polymeric film (less than 100 nm thick) or a molecular SAM is deposited on the surface of the SiO_2 layer. The SiO_2 layer is not replaced, but purposely kept beneath the organic dielectric layer to prevent complications such as gate dielectric leakage currents. The thin polymer films or the SAMs do not significantly affect the total thickness of the insulating layer. In this way, the devices can be tested and compared in a similar range of electric fields/gate voltages and therefore also at similar values of the densities of charge carriers accumulated in the transistor channel. On the contrary, a single polymeric dielectric layer would require a very high film thickness (up to a few microns) to minimize the gate leakage.

In this project, tetracene OFETs were fabricated in the bottom gate-top contact configuration, as shown in Figure 2.1. The OS was deposited on the gate insulator/gate electrode, whereas the source and drain contacts were deposited on the semiconducting layer as the final step of the fabrication process.

The substrates were heavily doped n-type <100> silicon wafers (100 mm diameter, 500÷550 μm thickness), with a resistivity of 0.001-0.005 Ohm·cm. A 200 nm thick layer of SiO_2 was grown by thermal wet oxidation at 1100 °C. Spectroscopic ellipsometry measurements were carried out to estimate the oxide layer uniformity. The thickness deviation was found to be smaller than 5% of

the nominal thickness. Afterwards, the wafers were cut into 2 cm × 2 cm pieces and cleaned by sequential sonication in acetone and isopropanol. The samples were then dried with a N_2 stream and exposed for 20 minutes to UV/Ozone to remove residual traces of organic contaminants.

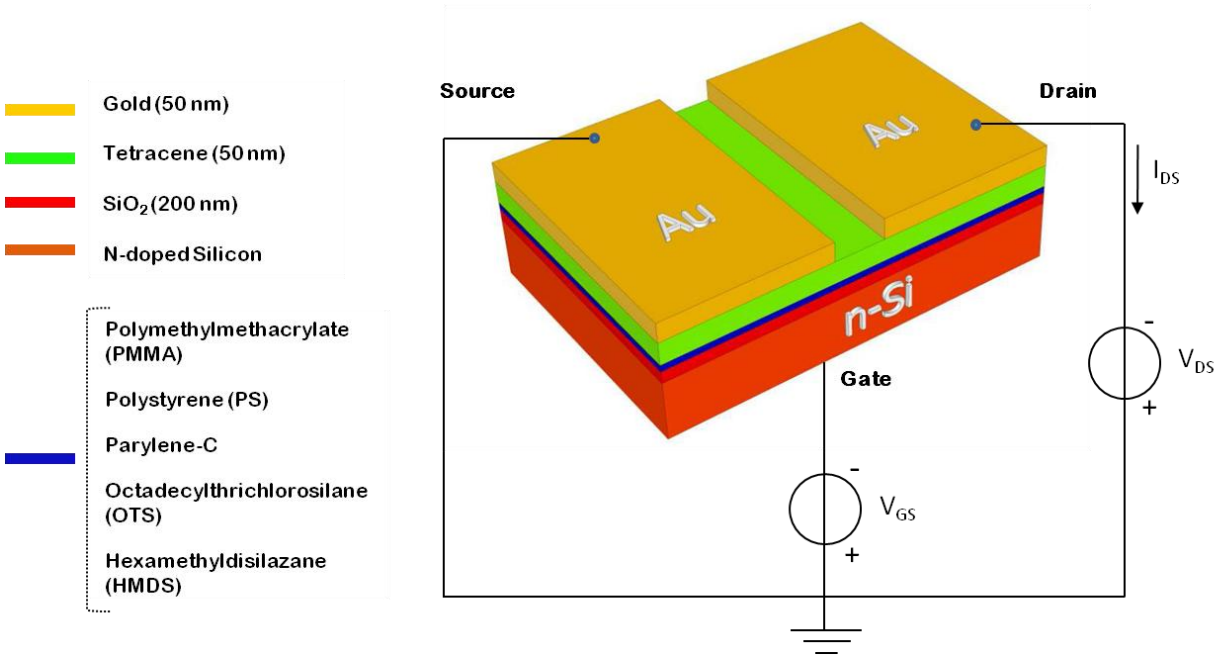

Figure 2.1 – Bottom gate – top contact tetracene OFET with a bilayer gate dielectric.

Five organic dielectric layers (PMMA, PS, parylene C, OTS, and HMDS) were considered. They were deposited as described in Section 2.3 – using both solution and evaporation-based techniques – and characterized as discussed in Section 2.2. After the deposition of the organic dielectrics, the samples were stored inside an MBraun N_2 filled glove box (O_2 and H_2O about 1 ppm). Tetracene films were deposited using a multi-source evaporator connected to the glove box (described in Section 2.4) and appositely designed to deposit both organic molecules and metals. Tetracene (more than 97% pure) was purchased from Tokyo Chemical Industry (Japan) and was used as received without any further purification. Thin films of tetracene were vacuum sublimed – at a base pressure of $2.5 \cdot 10^{-6}$ Torr – on the five organic dielectric surfaces. Films were also deposited on bare and photolithographically patterned SiO_2/Si substrates (with bottom Au source/drain electrodes) for reference analysis.

Due to the geometry of the sample-holder (10 cm diameter disk), it was not possible to include all the substrates in a single evaporation run. A single run would have been advantageous to avoid

complications emerging from possible run-to-run variations. At the same time, using a large sample holder would not have been an efficient solution, since the thicknesses of tetracene films deposited on samples located at two opposite edges of the sample holder (e.g. at a distance of 7-8 cm) may have differed by more than 15%, as will be discussed in Section 2.4. We then grew the films in two runs: (i) HMDS, OTS, bare SiO_2 and (ii) PS, PMMA, parylene C. In each run a pre-patterned reference sample was included to check the reproducibility of the deposition process. After tetracene evaporation, the vacuum chamber was filled with N_2 and opened towards the glove box space. The bottom contact reference sample was removed from the sample-holder to be electrically characterized, whereas shadow masks were applied to the other samples.

The masks were applied to the substrates, previously fixed to the sample-holder, with ~ 4 mm wide stripes of Kapton™ tape applied along the edges of the sample surface. The masks (1.8 cm × 1.8 cm, stainless steel, 250 μm thick) were gently laid on the substrates, with the rim contacting the Kapton™ tape stripes, and then fixed using two small pieces of tape already attached to the masks. The small thickness of the Kapton™ stripes (less than l00 μm) permitted to keep a gap between the shadow mask and the substrate. This approach was found to be effective in avoiding damages to the organic films that can emerge in case of a direct contact of the shadow mask with the substrate.

The sample-holder was then put back in the chamber and positioned in front of the Au source, as described in Section 2.5. After the deposition of the Au electrodes, the shadow masks were removed. The substrates were detached from the sample-holder and then transferred to the probe station for the electrical characterization of the devices. The devices were not encapsulated, but the adsorption of oxygen and water was limited by transferring the samples from the glove box where the fabrication took place to the glove box where the electrical measurements were carried out by the use of a suitably sealed transfer box. If the devices have to be operated under ambient conditions the encapsulation is strictly necessary. A straightforward encapsulation method is presented in reference [16] and consists in applying a glass coverslip onto the samples and sealing it with an ultraviolet-cured epoxy sealant.

Electrical measurements in FET configuration were performed in N_2 atmosphere. A semiconductor parameter analyzer (SPA, Agilent B1500A) was used for applying voltages to the gate and drain electrodes (with the source electrode being the common ground) and for

measuring the drain current and the gate leakage current. The intensity of the light emitted from tetracene films was detected by a silicon photodiode (Hamamatsu S1337-16BR) coupled to the probe station and placed in close proximity to the device surface (about 3 mm from the sample). The photodiode was inversely biased (-1 V) and the photocurrent was collected by the SPA and measured simultaneously with the acquisition of the output and transfer FET characteristics.

2.2 Experimental techniques

This section deals with the experimental techniques employed for the characterization of both the organic dielectric layers and the overgrown tetracene films: (i) Spectroscopic Ellipsometry and Profilometry, (ii) Atomic Force Microscopy (AFM) and (iii) Contact Angle goniometry. The principles and the fundamental physics underlying these methods will be presented together with the details of the operations carried out in the specific context of this research project.

2.2.1 Spectroscopic Ellipsometry and Profilometry

Ellipsometry is an optical technique that detects the variation of the polarization state of an electromagnetic wave, when it interacts with a material [37]. Most of the times, it consists in measuring the difference between the incident and the reflected electric field vectors associated to an electromagnetic wave reflected by a film/substrate system, as schematized in Figure 2.2.

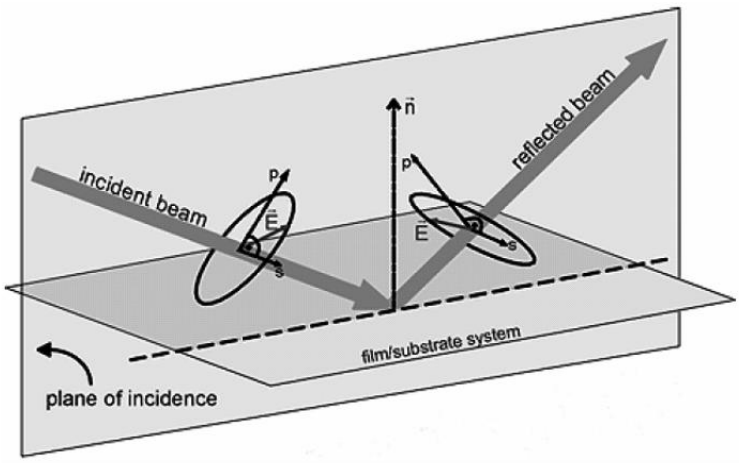

Figure 2.2 – Incident and reflected beams and corresponding electric field vectors used in Spectroscopic Ellipsometry [38]. The meaning of the symbols is given in the text.

Since the object of an ellipsometric measurement is the polarization state of the electric field, ellipsometry is not sensitive to the absolute intensity of the beam interacting with the material, so that convenient low-intensity light sources, with non-monotonous wavelength spectrum can be used. For this reason ellipsometry is referred to as a "self-normalizing" technique.

Differently from profilometry, ellipsometry is a non-contact/non-destructive technique and this fact alone could be enough to explain its wide utilization for the characterization of materials. Moreover, due to its versatility, it can be employed for the real-time in-situ monitoring of film growth [39]. It allows measuring both the thickness and the optical properties (e.g. dielectric constant) of thin films of a large variety of materials, such as organic and inorganic semiconductors/dielectrics, metals, and even composites [40].

The only requisite for extracting information with ellipsometry on the optical properties of a given material is the presence of a non-vanishing specular reflectivity from the sample surface. On the other hand, for determining film thickness, a further requirement is a partial absorption, so that part of the light can travel forth and back through the entire film.

For ellipsometry purposes it is convenient to consider the electric field vector $\vec{E}$, orthogonal to the wave propagation direction, as the sum of the vectors $\vec{E}_S$ and $\vec{E}_P$, orthogonal and parallel to the incidence plane respectively (Figure 2.2). Ellipsometry is interested in how these two components change upon reflection on the sample surface, in terms of their relative amplitude and phase. The quantities measured with an ellipsometer are Δ and Ψ, which are correlated to the Fresnel reflection coefficients by the following equation:

$$\rho = \frac{R_S}{R_P} = tan\psi \cdot e^{i\Delta} \tag{2.1}$$

Δ and Ψ are the so called ellipsometric angles, which describe the change in phase (Δ) and amplitude ($tan\psi$) of the polarization state. R_S and R_P and are the complex Fresnel reflection coefficients associated to $\vec{E}_S$ and $\vec{E}_P$ respectively and contain all the information about the sample, including optical constants and thickness.

The basic components of the spectroscopic ellipsometer used in this research project (M-2000V by J.A. Woollam Co., Inc) are presented in Figure 2.3. A Xenon arc lamp is used to produce broadband white light, whose wavelengths are individually selected by a monochromator in a

spectral range going from 300 to 1000 nm (390 points). Afterward, a polarizer transforms the incoming unpolarized light into linearly polarized light, whose state of polarization is known. After reflection on the sample, the light passes through the analyzer (usually a rotating polarizer) and it is collected by the detector, which measures the new state of polarization in terms of Δ and Ψ. A computer is used for signal processing and data elaboration.

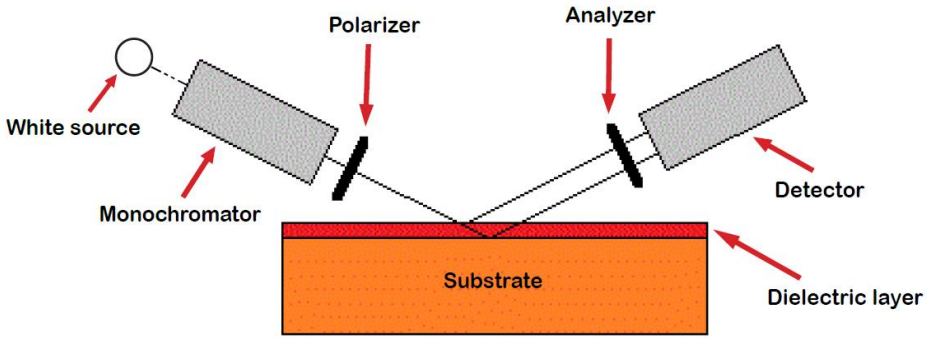

Figure 2.3 – Basic components of an ellipsometer. A known polarization state is changed upon reflection and the final polarization state is measured by the analyzer and the detector.

The data analysis is carried out by comparing the theoretical response, calculated according to a model of the sample, with the real experimental data. The model is built on the basis of the Fresnel's equations and takes into account both the thickness and the optical constants of each layer in the sample. If these are not known, an initial estimate must be given; afterwards, the unknown parameters are varied to improve the matching between theory and experiment. The Mean Square Error (MSE) is the figure of merit for the quality of this matching so that the unknown variables are allowed to vary till this figure achieves a minimum value.

The unknown parameters are fitted by means of the software VWASE32 [41], which calculates the MSE as the sum of squares of the differences between the measured and generated data (ψ, Δ), with each difference weighted by the standard deviation of the measured data, according to the formula:

$$MSE = \frac{1}{2N_C - N_V} \sum_{i=1}^{N_C} \left[\left(\frac{\psi_i^{mod} - \psi_i^{exp}}{\sigma_{\psi,i}^{exp}} \right)^2 + \left(\frac{\Delta_i^{mod} - \Delta_i^{exp}}{\sigma_{\Delta,i}^{exp}} \right)^2 \right] \qquad (2.2)$$

where N_C and N_V indicate the number of couples (ψ, Δ) and the number of variables in the model; the expressions mod and exp denote the *modeled* and the *experimental* ellipsometric angles respectively and σ is the standard deviation of the experimental data.

Afterwards, the software minimizes the MSE and provides the values of the unknown parameters (e.g. thickness) in correspondence of the minimum MSE value. The convergence is obtained upon application of the Levenberg–Marquardt algorithm, which is a standard routine for the adjustment of non linear curves [41-42].

For MSE values in the range from 3 to 4, the experimental and calculated curves fairly overlap with each other, as shown in Figure 2.4, which is relative to a thin layer of PMMA deposited a thermally oxidized silicon wafer.

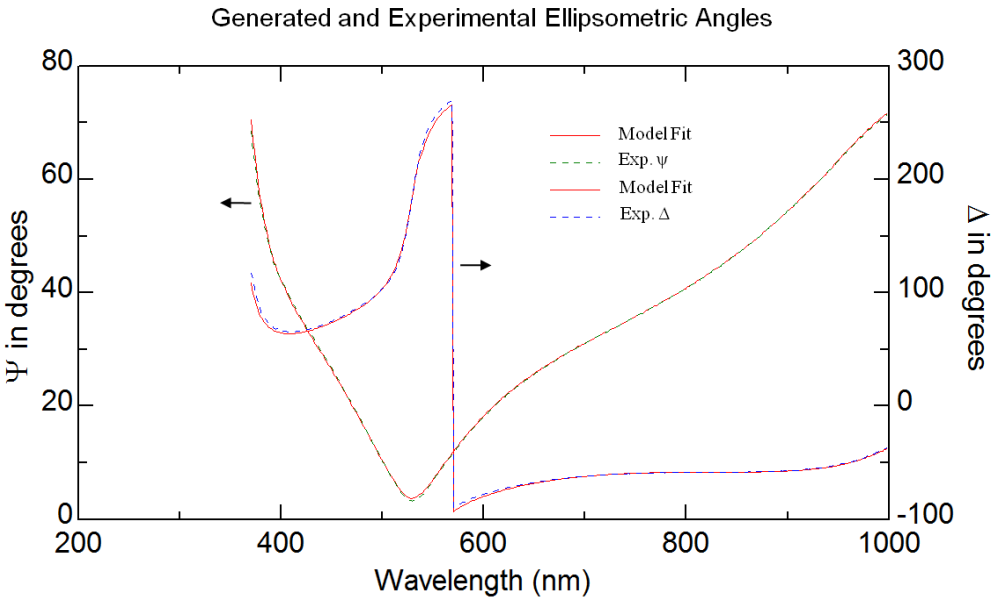

Figure 2.4 – Ellipsometric angles measured experimentally (ψ in green and Δ in blue) and calculated from the theoretical model (red). The curves are relative to a thin layer of PMMA spin coated on a thermally oxidized silicon wafer (ca. 30 nm of PMMA on 200 nm of SiO_2 on a Si(100) wafer). A fair overlap between generated and experimental data exists, corresponding to an MSE value equal of 3.61.

The thickness of PMMA and PS films, deposited on the oxidized silicon wafers, was determined by constructing a three-layer model, including a massive Si substrate, a 200 nm thick layer of SiO_2 and a polymer film. For the first calculation, the thickness of the polymer layer was set to an initial hypothetical value and allowed to vary; the refraction index was modeled according to the Cauchy-Sellmeier equation:

$$n(\lambda) = A + \frac{B}{\lambda^2} + \frac{C}{\lambda^4} \tag{2.3}$$

This relationship is suited for transparent materials (i.e. for materials whit k ≈ 0, where k is the imaginary component of the refraction index) [41] and is commonly employed for modeling polymeric materials. The values of the three parameters A, B, and C are available on polymer handbooks or ellipsometry databases. We report them below:

$(A, B, C)_{PMMA}$ = (1.4855, 0.003714, 0.000079207) $(A, B, C)_{PS}$ = (1.5364, 0.007815, 0.000385)

It is worth noting that different preparation conditions of the polymer films, such as the polymer solution concentration, may give rise to films with slightly different refraction indexes. The three parameters A, B, and C were not kept constant, but were allowed to vary, starting from the values found in literature [42]. The fitted parameters were not found to deviate significantly from the original ones.

According to reference [43], the angle of incidence – i.e. the angle between the direction of the incident wave and the direction normal to the sample – was set to 70° and the ellipsometer was calibrated using thermally oxidized silicon substrates. Afterward, samples with PMMA and PS were tested, each one at least three times in three different regions. In each case, the minimum MSE observed (always lower than 6) suggested a high reliability of the results. At the first time, to confirm the efficacy of the method, we checked the thickness by means of profilometry. The two measurements were not found to differ by more than 1 nm.

In the case tetracene films, due to their granular polycrystalline structure, modeling the sample was not straightforward. Therefore, before evaporating tetracene, a sacrificial substrate was located inside the evaporation chamber, to be subsequently tested by means of a mechanical profilometer (Veeco Dektak). The thickness of gold top contacts was also measured by means of profilometry, through the evaluation of the height of the tetracene-gold step.

Mechanical Profilometry is a contact technique used for characterizing the surface profile of a sample. The basic principle is the following: a diamond stylus is scanned over a sample surface while its vertical displacement is measured and recorded by means of a capacitive transducer, generating a profile of the surface. This technique is commonly employed for measuring the height of a step-feature. In our case, a tetracene/substrate step was realized on the sacrificial sample by means of shadow masking. The drawbacks of this technique are essentially the direct contact with the sample and the dependence on the overall surface planarity. The substrate should be planar enough to provide a well-defined reference plane [44].

2.2.2 Atomic Force Microscopy

Atomic force microscopy (AFM) was invented in 1986 by G. C. Binnig, C. Quate, and C. Gerber [45], few years after the invention of Scanning Tunneling Microscopy (STM) for which G. Binning and H. Rohrer were awarded of the Nobel Prize in Physics in 1986. These two techniques revolutionized the concept of microscopy, introducing a new generation of instruments, the Scanning Probe Microscopes (SPM) that provide information about the surface properties of materials in a spatial range going from a few angstrom to several microns. Each SPM instrument is able to sense a specific material property, but all of them share a basic principle. A probe, typically a sharp tip, is scanned across the sample, while the probe-sample interactions are measured and recorded to give a map of the sample surface. Interactions of different nature are sensed by different SPMs. For instance, STM measures the tunneling current between a sharp metal tip and the atoms of a conductive specimen. AFM is extremely popular since its use is not limited to a specific type of specimen such that it can be employed on metals, semiconductors, and insulators, without any special specimen preparation. Moreover it can be employed in ambient air or even in liquids [46].

In AFM, a sharp tip – usually a few microns long and with a radius of curvature of less than 10 nm – is microfabricated at the free end of a cantilever. The interatomic forces occurring between tip and sample, induce a cantilever deflection proportional to their strength [47]. The deflection is recorded as the tip is scanned across the sample, yielding a topographical map of the surface. Often, as shown in Figure 2.5, the small cantilever deflection is measured by means of a laser beam directed to the back of the cantilever and reflected off to a position-sensitive photodiode.

Piezoelectric transducers and actuators – in the form of cylindrical tubes – are frequently used to monitor and control the relative tip-sample position in the x, y, and z directions.

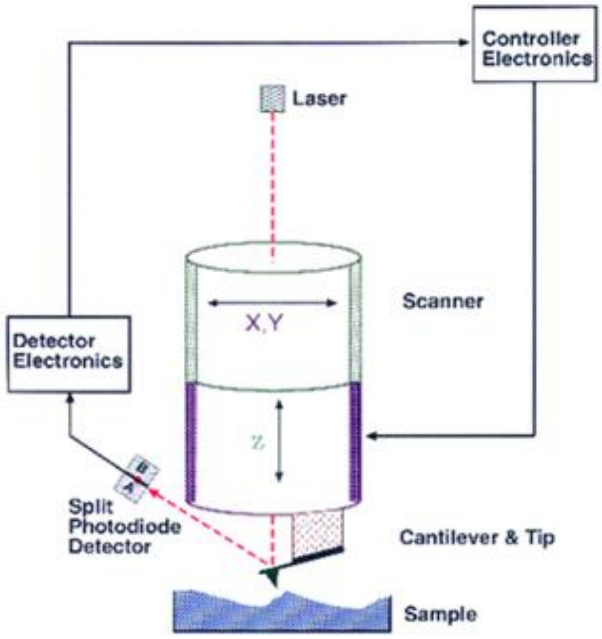

Figure 2.5 – Schematic illustration of the operating principle of an AFM (from Digital Instruments, Santa Barbara, California).

Two different modes are possible for operating an AFM, depending on the tip-sample distance. The interaction between the atoms at the apex of the tip and those of the sample surface is conveniently described in terms of van der Waals forces, whose typical dependence on the tip-sample distance is shown in Figure 2.6. As the tip approaches the surface, the attractive forces predominate and keep increasing till the electron clouds of the tip and of the surface atoms begin to repel each other. Starting from this point, the repulsive forces become increasingly more significant and tend to balance the attractive forces. When the attractive and repulsive interactions compensate the tip lies exactly in physical contact with the surface. It is under this condition that the *contact mode* AFM is performed. As the tip is scanned over the surface, the cantilever deflects to accommodate changes in the sample morphology. The cantilever deflection is measured and used as the input of a feedback loop that maintains a constant setpoint deflection by varying the *z* component of the piezoelectric actuator. The topographical image is then derived from the vertical motion of the piezoelectric actuator. In *contact mode*, it is also possible to obtain a map of the interaction forces over the surface, by keeping the z-coordinate constant,

measuring the cantilever deflection and calculating the force using the Hooke's equation, $F = -k \cdot \Delta x$, where k and Δx are the cantilever spring constant and displacement respectively.

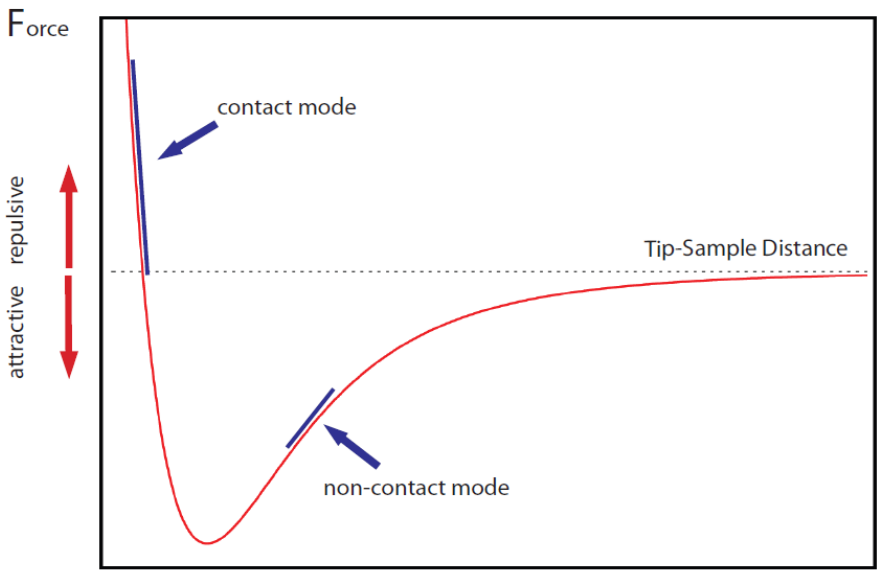

Figure 2.6 – Van der Waals force occurring between tip and sample as a function of the tip-sample distance in an AFM microscope.

The main drawback of the *contact mode* AFM is sample damaging arising from surface friction. Especially when dealing with delicate biological and organic specimens, the tip-substrate contact has to be avoided since it alters the sample characteristics. To face this obstacle, a *non-contact mode* AFM has been developed. The tip is kept about 5–15 nm far from the substrate and the attractive van der Waals forces are sensed. However, in this position, the interactions are weaker and not as much sensitive to the tip-sample distance as in *contact mode*. To increase the measurement sensitivity, the tip is made to oscillate at a given frequency (close to the resonance frequency of the cantilever) and amplitude, by means of a piezoelectric crystal. As the tip is scanned across the sample surface, the variations in amplitude (or frequency) are measured and they are used as the input of the feedback loop that controls the cantilever z-coordinate and restores the setpoint amplitude (or frequency).

When the oscillation amplitude is used as the feedback signal, the technique is referred as Amplitude Modulation (AM) and is commonly employed in ambient air. When the frequency is

used as feedback input, the technique is referred to as Frequency Modulation (FM) and is most commonly adopted in UHV environments [48].

The main drawback of *non-contact mode*, with respect to *contact mode*, is its lower vertical resolution. An intermediate approach was developed by Digital Instruments to overcome the limitations of both modes. It is called *Tapping Mode* and allows imaging soft and easily damageable samples with high resolution. Basically, it works as an AM *non-contact mode* where, at the bottom of each oscillation, the tip lightly touches the substrate, entering in physical contact with the surface. The high "tapping" frequency (a few hundred thousand cycles per second) avoids the tip to stick on the sample and prevents damages. Furthermore, the intermitting physical contact allows for high resolution.

In the context of this work, the AFM imaging of the organic dielectrics and tetracene thin films was performed using *Tapping Mode*. Different scanning-area dimensions were considered, ranging from 1 μm × 1 μm to 30 μm × 30 μm. For each specimen, at least four images were taken in four distinct locations of the sample.

A Digital Instruments Dimension 3100 (Santa Barbara, CA) microscope was operated in ambient air, at room temperature, with a scan rate of 1 Hz. Aluminum-coated, etched silicon cantilevers (Arrow-NCR from Nanoworld), characterized by a spring constant $k \simeq 42\, N \cdot m^{-1}$, were oscillated close to their resonance frequency (about 300 kHz) with a medium oscillation damping (20–30%). The tip radius was 10 nm.

The RMS roughness of an AFM image, constituted by M × N pixels (usually 512 × 512), is given the following equation:

$$\mathrm{RMS} = \sqrt{\frac{1}{\mathrm{NM}} \sum_{\mathrm{i}=0}^{\mathrm{N}-1} \sum_{\mathrm{j}=0}^{\mathrm{M}-1} [\mathrm{z}(\mathrm{i},\mathrm{j}) - \bar{\mathrm{z}}]^2} \tag{2.4}$$

Where $\mathrm{z}(\mathrm{i},\mathrm{j})$ is the surface height at the position (i,j), and $\bar{\mathrm{z}}$ is the average height, given by:

$$\bar{\mathrm{z}} = \frac{1}{\mathrm{NM}} \sum_{\mathrm{i}=0}^{\mathrm{N}-1} \sum_{\mathrm{j}=0}^{\mathrm{M}-1} \mathrm{z}(\mathrm{i},\mathrm{j}) \tag{2.5}$$

The average Root Mean Square (RMS) roughness of the dielectrics layers was obtained by averaging the RMS roughness of four images, each one weighted according to its surface area.

The acquisition/processing of the images and the roughness analysis were performed by the software NanoScope v.5.30. The elaboration of the AFM data concerning the nucleation and the growth of tetracene films (described in Section 3.1), was conducted by means of the software WSxM v.5.0, whose functions are reviewed in reference [49].

2.2.3 Contact Angle Technique

Measuring the contact angle (CA) formed by a liquid droplet (e.g. water) with a solid surface is a convenient and straightforward method for describing quantitatively the wettability of a substrate. This technique has also long been used for determining the surface free energy of solids [50-52].

As shown in Figure 2.7, the CA (θ) is the angle formed between the solid/liquid (SL) interface and the tangent to the liquid/vapor (LV) interface. Its vertex lies on the so called "contact line", i.e. at the intersection of the SL and LV boundaries with the solid/vapor (SV) interface.

Low water CAs indicate that the surface is hydrophilic; on the contrary, high water CAs reveal hydrophobicity. When the water spreads homogeneously over the surface, the CA is zero and this condition is referred to as "complete wetting". Instead, when the CA is larger than 90° the substrate is defined "not wetting".

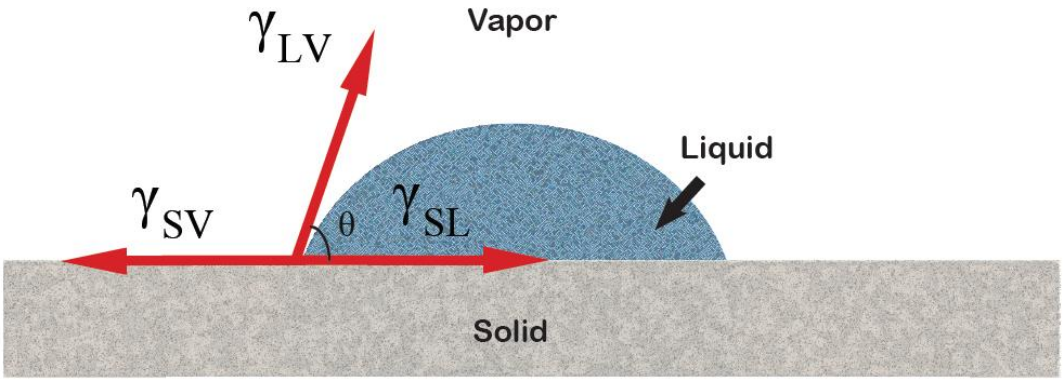

Figure 2.7 – Schematic representation of the contact angle θ and illustration of the three surface tension forces included in the Young's equation (see text).

The CA is formed when the three surface tension forces – associated to the SL, SV and LV interfaces – balance each other . This condition is expressed by the Young's equation:

$$\gamma_{SV} = \gamma_{SL} + \gamma_{LV}\cos\theta \qquad or\ equivalently \qquad \cos\theta = \frac{1}{\gamma_{LV}}(\gamma_{SV} - \gamma_{SL}) \tag{2.6}$$

where, γ_{SV}, $\gamma_{SL}$and γ_{LV} are the surface tension energies associated to the three interfaces and θ is the CA. The known quantities in the equation are only θ and γ_{LV}; the former is measured experimentally, while the latter is a specific property of the liquid drop. By measuring the CAs formed by droplets of liquids with different values of γ_{LV}, it is possible to extract the surface free energy γ_{SV} of a solid, only if an additional relationship exists. In fact, γ_{SL} depends on the characteristics of both the liquid and the solid, so that the plot of $\cos\theta$ versus $1/\gamma_{LV}$ is not simply a straight line. Extensive work has been conducted to individuate conditions of the type $\gamma_{SL} = F(\gamma_{SV}, \gamma_{LV})$ to respond to this need. For further information we refer to the works of Zisman [53], Tavana and Neumann [51].

The wettability of the organic dielectric substrates was investigated by means of the sessile drop method. Droplets of ultrapure water (18 MΩ·cm) – with a diameter of about 0.4/0.5 cm, were deposited on the sample by means of a micro-syringe. CA measurements were performed at room temperature and ambient humidity (r.u ~30%) using a Ramé-Hart Inc. goniometer. Three drops, on three distinct regions of the sample, were deposited and measured on both droplet's sides. For each type of substrate, at least two specimens have been analyzed. Variations of the CA with time were also taken into account, by measuring the same drop few times at intervals of 1 minute. The final values and the corresponding variability, are obtained by averaging all the measurements conducted for each dielectric substrate.

2.3 Organic dielectric layer deposition and characterization

The specific methods for depositing the different organic dielectric layers are discussed in the following sections. Here we introduce the reasons that led us to choose each one of the dielectric materials and we give an overall presentation of the results obtained from their characterization.

Polymethylmethacrylate (PMMA) is a thermally and mechanically stable polymer, which presents high resistivity (larger than $2 \cdot 10^{15}$ Ωcm). Its dielectric constant is similar to that of SiO_2 and it can be easily deposited on large areas and processed at relatively low temperatures (below 170 °C). In addition, from a chemical point of view, PMMA has hydrophobic methyl radical groups, which can act as moisture inhibitors and are known to favor order in a number of overgrown molecular films [54]. These factors all contribute to make of PMMA an optimum candidate as a gate dielectric layer in OFETs; this is clearly witnessed by its increasing popularity in the organic electronics community [54-56].

Polystyrene (PS) does not have polar groups and it can easily form smooth and uniform films when spin-coated on SiO_2. Similarly to PMMA, PS thin films present minimal gate leakage and very low surface roughness. Moreover, several reports exist in literature showing that PS leads to increased electron mobility of air-sensitive OS films deposited on its surface [22].

Parylene C, differently from other polymers, can be deposited from the vapor phase by means of chemical vapor deposition polymerization [57]. Therefore, the drawbacks commonly associated to solution processing – such as impurities coming from the solvents, solvent traces trapped into the film – can be avoided. Moreover, we observe that parylene C is hydrophobic and chemically inert, thus opening the possibility to promote electron transport in the overgrown OS film [23].

Self Assembled Monolayers (SAMs), such as Octadecylthrichlorosilane (OTS) and Hexamethyldisilazane (HMDS), provide a straightforward method for tuning the chemical and physical properties of a substrate surface. When deposited on SiO_2, monolayers of OTS and HMDS lead to (i) lower substrate surface energy and (ii) reduced density of electron traps associated to the surface hydroxyl groups. This induces a significant improvement in the functional properties of the overgrown OS films, which is widely documented in the literature. Hereafter we mention a few reports that illustrate the efficacy of the SAM approach for improving the charge carrier transport of both polymer and small-molecule OSs.

Improvements in transistor performance have been reported for pentacene thin films deposited on OTS treated SiO_2 [58-59]. OTS monolayers contribute considerably to enhance the quality of the overlying pentacene films, which are characterized by ordered domains and larger and smoother grains, if compared to films deposited on bare SiO_2 [34]. Salleo measured a twenty fold enhancement of the hole FET mobility of a polyfluorene copolymer (F8T2), after OTS treatment of the SiO_2 surface. [60]

Similarly, an increase of the FET mobility for P3HT grown on HMDS treated SiO_2 has been reported [61-62]. Bao [63] proved that the FET mobility is higher for pentacene thin films deposited on HMDS treated SiO_2, where the overgrown pentacene films are characterized by more compact and less dendritic islands compared to bare SiO_2 [64].

In the context of this research project, the use of polymers and SAMs for tuning the properties of the dielectric substrate will be discussed in relation to the characteristics of the overgrown tetracene thin films. The entire experimental work was therefore conceived into two parts: the first devoted to the deposition and characterization of the dielectrics, the second devoted to the deposition and characterization of the tetracene films. Throughout Section 2.3 we will be dealing with the first part, describing the specific methods for the deposition of the dielectrics. Herein we introduce the general procedure adopted to characterize the dielectric layers.

For each dielectric substrate we investigated its morphology by means of AFM and we evaluated the average value of the Root Mean Square (RMS) Roughness. Afterwards, we calculated the capacitance of the bilayer structure using the formula of the series capacitance:

$$\frac{1}{C_{tot}} = \frac{1}{C_{polymer}} + \frac{1}{C_{oxide}} \tag{2.7}$$

The capacitance of a single layer is given by $C_i = \frac{\varepsilon_r}{t_i}\varepsilon_0$, where t_i is the thickness of the layer, ε_r is the layer relative dielectric constant and ε_0 is the absolute dielectric constant. The thickness of the polymeric dielectric layers was measured experimentally, by ellipsometry and profilometry, following the procedure described in Section 2.2.1. The relative dielectric constant was extracted from the literature. In the case of SAMs, we assumed that a single monolayer does not affect the overall gate dielectric capacitance, which therefore remains equal to that of the SiO_2 layer.

Finally, we measured the water contact angle according to the procedure presented in Section 2.2.3. The results are all reported in Table 2.1, together with the indication of the specific characteristics of each dielectric material. The values of the capacitance reported in Table 2.1 are relative only to the top-dielectric layer and not to the bilayer structure. The capacitance values of the entire bilayer-structures were calculated using Equation 2.7 and are reported in Table 2.2.

Dielectric	Characteristics	Thickness	Av. Water Contact Angle	Layer Capacitance	Av. RMS Roughness
Parylene C 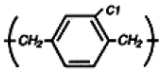	*Oxygen-free. Hydrophobic*	93 ± 4 nm	85°	29.9 nF·cm^{-2}	1.2 nm
Polystyrene (PS) 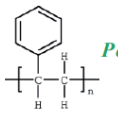	*Minimal roughness. Hydrophobic*	33 ± 1 nm	87°	69.7 nF·cm^{-2}	0.145 nm
Polymethylmetacrilate (PMMA) 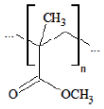	*Low leakage. Low dielectric constant*	35 ± 1 nm	67°	88.5 nF·cm^{-2}	0.15 nm
Hexamethyldisilazane (HMDS) 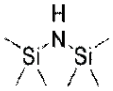	*Self-assembled monolayer*	-	68°	-	0.27 nm
Octadecyltrichlorosilane (OTS) 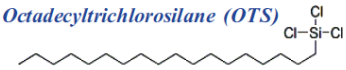	*Self-assembled monolayer*	-	83°	-	0.3 nm
Silicon Dioxide	*Reference gate dielectric*	200 ± 2 nm	28°	17.3 nF·cm^{-2}	0.11 nm

Table 2.1 – Properties of the organic dielectric layers employed in this project.

	Bare SiO_2	OTS	HMDS	PARY C	PS	PMMA
C_{TOT}	17.3 nF·cm^{-2}	~17.3 nF·cm^{-2}	~17.3 nF·cm^{-2}	10.9 nF·cm^{-2}	13.8 nF·cm^{-2}	14.4 nF·cm^{-2}

Table 2.2 – Total capacitance of the dielectric bilayers employed in this project.

We conclude this part by presenting the complete set of AFM images of the dielectrics layers (Figure 2.8). This will be used for further discussion throughout the following sections.

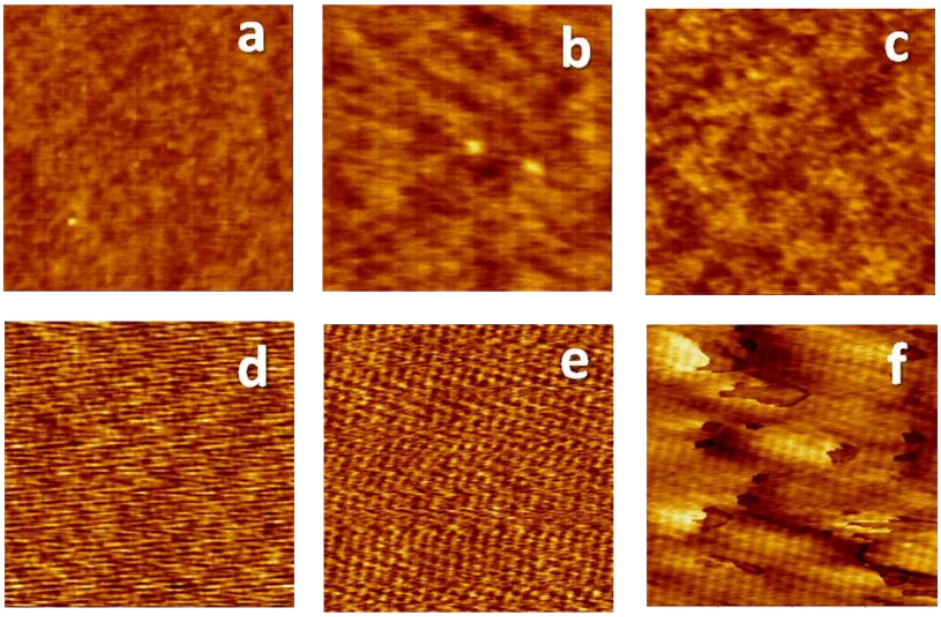

Figure 2.8 – 1 μm × 1 μm AFM images of the dielectric substrate surfaces employed in this project; height scale: 0 - 3 nm. (a) bare SiO_2; (b) PS; (c) PMMA; (d) OTS; (e) HMDS; (f) parylene C.

2.3.1 Polystyrene and polymethylmethacrylate thin films

This section deals with the preparation of ultra thin PS and PMMA films using the spin coating technique. The choice of the deposition parameters has been conducted with special care, both referring to the existing literature [22, 43, 54-55, 65-67] and applying an appropriate design of experiments [68-69]. The control variables that determine the final thickness of the polymer film and its quality, in terms of smoothness and uniformity, are the rotation speed, the solution concentration, the solution viscosity, the polymer molecular weight and the solvent volatility. The spinning time is not a critical parameter, provided that it is large enough to allow the complete evaporation of the solvent. Instead, the acceleration time, defined as the time required to achieve the target rotation speed, was found to play a crucial role in determining film uniformity and pinholes density. Similarly, the amount of solution to dispense is not a significant process parameter, provided that it is enough to cover the whole sample surface. On the other hand, it is important to choose if the solution is dispensed in a dynamic or static manner. The dynamic approach consists in dispensing the solution while the substrate is turning at low speed,

while the static approach consists in dispensing the fluid on the sample surface before the spinning starts.

There are other external factors that can significantly influence the process but cannot be easily controlled. Among them we considered the temperature and the humidity of the ambient air, which affect the solvent evaporation rate and therefore the film formation kinetics; the cleanness of the sample surface; the purity of the solution; the shape of the sample and its position with respect to the sample holder, which can cause an asymmetric rotational momentum and consequently a non-uniform spreading of the fluid.

To avoid the effects of these factors, we adopted specific strategies. Firstly, before spinning the solution we measured the ambient temperature and relative humidity. The spin process was conducted at ~21 °C and at a relative humidity lower than 38%. These values were found to be in agreement with those indicated in the literature [22].

Secondly, we filtered all solutions through a 200 nm pore size nylon membrane syringe filter [70]. This allowed removing particles of dust and agglomerates of polymers. Immediately before depositing the solution, a nitrogen blow was used to remove the dust particles from the substrates.

Finally, we had a special attention in cutting regular squares of silicon wafers and in positioning them precisely on the sample-holder, with the specimen barycentre over the center of rotation of the spin coater. Because of the squared shape of the samples, the resulting films were not uniform in the proximity of the sample corners. However, the devices were fabricated on the central area of the samples, where the films were found to be smooth and pinhole-free.

The steps carried out to limit the external factors were all essential to obtain uniform, smooth and continuous films of PMMA and PS. Nevertheless, the efficacy of these methods was not absolute, and a limited rate of success (~70%) had to be associated with the film formation process.

The optimal values for the control variables were found starting from those reported in the literature and conducting experiments. Different combinations of the control parameters have been chosen and after each “trial” the resulting films were analyzed by means of AFM and optical microscopy; their thicknesses were measured by means of ellipsometry or profilometry. Four different solution concentrations were considered (5 mg/ml, 10 mg/ml, 15 mg/ml and 30

mg/ml) together with the possibility of static/dynamic dispense and presence/absence of acceleration ramps. The spin speed was kept constant at the value of 5000 rpm, as indicated in reference [22] and [54] for PS and PMMA, and the spin time was set to 60 seconds. The polymers, characterized by a molecular weight of 211,000 g/mol for PS and 100,000 g/mol for PMMA, were purchased from Sigma Aldrich and were used without further purification. Toluene (Sigma Aldrich, 99.8%) was chosen as the solvent for both PS and PMMA.

PMMA is not easily soluble in toluene so that it was necessary to gently heat the solution (up to 50 °C) and leave it stirring overnight. Other solvents, such as chloroform, are most commonly used in combination with PMMA. However, toluene – with a vapor pressure of 0.037 atm at 25 °C – is significantly less volatile than other solvents (for instance, it is seven times less volatile than chloroform, which has a room-temperature vapor pressure of 0.26 atm). It has been proven that low solvent volatility, which implies slow evaporation, causes a larger radial outflow during the spin coating process; in turn, this allows obtaining thinner, smoother and more uniform films [43].

Before studying the properties of PMMA and PS films at different concentrations, we have been studying the acceleration time, as well as the method of solution dispense. We noticed that setting a slow acceleration ramp had a negative effect on the overall film quality and that the best films were obtained with the smallest possible acceleration time. Moreover, we observed that the solution dispense had to be conducted in a static way, covering the whole sample surface before spinning. The dynamic approach is not adequate, since the dispense of the solution must be done when the sample is rotating at low speed but – as previously mentioned – this does not contribute positively to the film quality. The non-uniformity of films deposited using the dynamic dispense or setting an acceleration ramp was even visible to the naked eye, as shown in Figure 2.9.

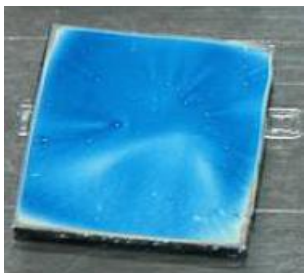

Figure 2.9 – PMMA spin-coated on SiO_2/Si substrates using the dynamic dispense procedure (see text for details).

Thin films of PMMA and PS were spin-coated over the SiO_2 on Si substrates using the four aforementioned concentrations. After spin coating, all the films were left overnight inside a vacuum oven kept at a temperature of 80 °C, to induce the evaporation of residual traces of solvent.

We could observe that not only the thickness of the film changes as a function of the concentration but also the film aspect.

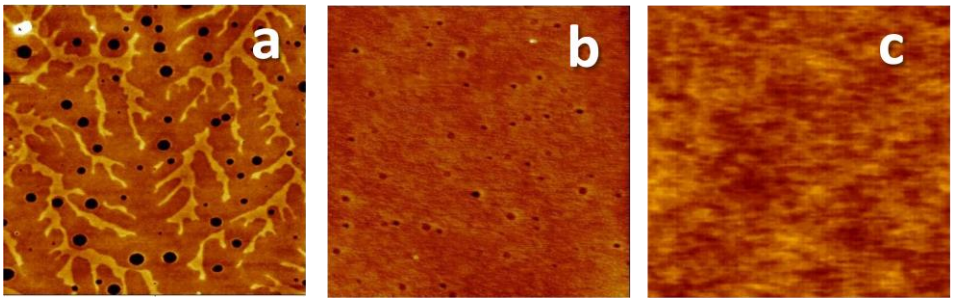

Figure 2.10 – AFM images of PS thin films deposited on SiO_2 on Si substrates; image size 3 µm × 3 µm; height range: 0 - 3 nm; concentrations: (a) ~3 mg/ml, (b) 5 mg/ml, (c) 10 mg/ml.

In the case of PS, for concentrations below 5 mg/ml, the resulting films are neither integer nor uniform and present pinholes and dendritic structures, as shown in Figure 2.10a. At a concentration of 5 mg/ml the PS layer becomes uniform, even though pinholes remain visible in the AFM image (Figure 2.10b). For concentrations above 5 mg/ml the PS films appear smooth, uniform and integer (Figure 2.10c). Once the spin speed is fixed at 5000 rpm, the thickness increases with the concentration up to 33.5 ± 1 nm (ellipsometry) at 10 mg/ml and to 63 ± 2 nm (ellipsometry/profilometry) at 15 mg/ml. The RMS roughness, as measured by AFM, also increases with film thickness, presenting an average value of 0.145 nm at 10 mg/ml.

In the case of PMMA we could not observe a change in the film aspect with the solution concentration, but only a decrease in the density of pinholes while increasing the concentration. At the same spin speed used for PS, the thickness of the PMMA films assumed slightly smaller values: 24.5 ± 1 nm (ellipsometry) at 10 mg/ml and 35 ± 2 nm (ellipsometry/profilometry) at 15 mg/ml. The average RMS roughness at 15 mg/ml was found to be very similar to that of PS films at 10 mg/ml. The similarity between films of PS and PMMA emerges also from the observation of their AFM images (Figure 2.8c and Figure 2.8b).

The water contact angle was measured for PMMA and PS films deposited from the four solutions at different concentrations. As one would expect, the contact angle does not vary as a function of the concentration. However, as illustrated in reference [66], for very low concentrations, the water contact angle on PS decreases significantly, because of the non uniform coverage of the surface. The contact angle measurements were repeatable over several batches of samples and the values 87 ± 2° for PS and 67 ± 2° for PMMA were observed, in agreement with those reported in the literature [56, 66].

The solution concentrations selected to carry on the fabrication of the OFET devices were 10 mg/ml and 15 mg/ml for PS and PMMA respectively, whose corresponding film thicknesses and RMS roughness are basically identical, considering the error bars of the measurements.

The last step in the characterization of the PS and PMMA films was the evaluation of the capacitance per unit surface area of the polymer/SiO_2 dielectric structure. It was calculated as a series capacitance constituted by 200 nm of SiO_2 and 33.5 nm (PS) or 35 nm (PMMA) of polymer films, according to Equation 2.7. The low-frequency values of the polymers' dielectric constants were extracted from the literature. PMMA has a dielectric constant similar to that of SiO_2 [54, 71] (~3.5), while PS has a lower dielectric constant, approximately equal to 2.6 [22, 71]. Facchetti et al [22] obtained a value of 2.5 for the dielectric constant of thin films of PS and have proven that this value does not change significantly (less than 3%) in a range of frequency from 0 to 100 kHz. The values of calculated capacitance for the individual polymeric layers are reported in Table 2.1.

2.3.2 Parylene Vapor Deposition

The term parylene indicates a unique class of polymers that can be deposited from the vapor phase and that are able to form highly conformal and chemically inert films [72]. Among the many applications of parylene, the most popular are in the microelectronics (e.g. packaging, gas/moisture barrier) and biomedical industries, or more recently in the fabrication of microstructures, such as Micro-Electro-Mechanical Systems (MEMS) and microfluidic systems [73]. Beyond being biocompatible, chemically resistant, thermally stable and capable to withstand low temperature and high vacuum, parylenes are also excellent dielectrics. Among the 20 types of parylenes available, the most common are three – parylene C, D and N – whose chemical structures are shown in Figure 2.11.

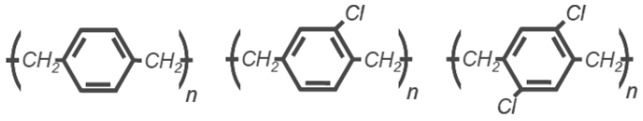

Figure 2.11 – Chemical structures of parylene N, C and D.

The different chemical structures of these polymers lead to a variety of mechanical, electrical and thermal properties. In Table 2.3 we report some properties of interest for applications of parylenes as OFET gate dielectrics [74].

	Parylene N	**Parylene C**	**Parylene D**
Dielectric Constant at 60 Hz	2.65	3.15	2.84
Volume Resistivity	14 x 10^{16} Ω·cm	8.8 x 10^{16} Ω·cm	12 x 10^{16} Ω·cm
Water Absorption (% after 24h)	< 0.1	< 0.1	< 0.1
Breakdown Voltage for 1 µm thick films	276 V	220 V	217 V

Table 2.3 – Some properties of parylene N, C, and D [74].

Parylene N is known to produce the best barrier against gas and moisture, but its main drawback is the low deposition rate, that makes it not favorable for mass production processes. Among the three parylenes, we used parylene C (poly(monochloro-p-xylylene)) which presents a good combination of electrical properties and low permeability to gas and moisture. However, the presence of chloride in its chemical structure renders it a polar dielectric material, which can have some effects on the charge carrier transport properties of the overgrown OS films (Section 3.2).

The process used to deposit parylenes is called Chemical Vapor Deposition (CVD) Polymerization and it requires that a spontaneous polymerization occurs on the sample surface. It is worth noting that parylene is deposited inside a vacuum chamber kept at a base pressure of a few mTorr, where the molecular mean free path is of the order of 1 mm. Therefore the monomers impinge the substrate from homogenously distributed directions thus permitting the deposition of uniform and pinhole-free films.

The deposition process consists of three distinct steps, namely (i) vaporization, (ii) pyrolysis, (iii) deposition/polymerization, which take place inside the three distinct parts of the vacuum deposition system, as illustrated in Figure 2.12. The deposition system employed in the context of this research project was a Labcoater 2 PDS 2010, developed by Specialty Coating Systems.

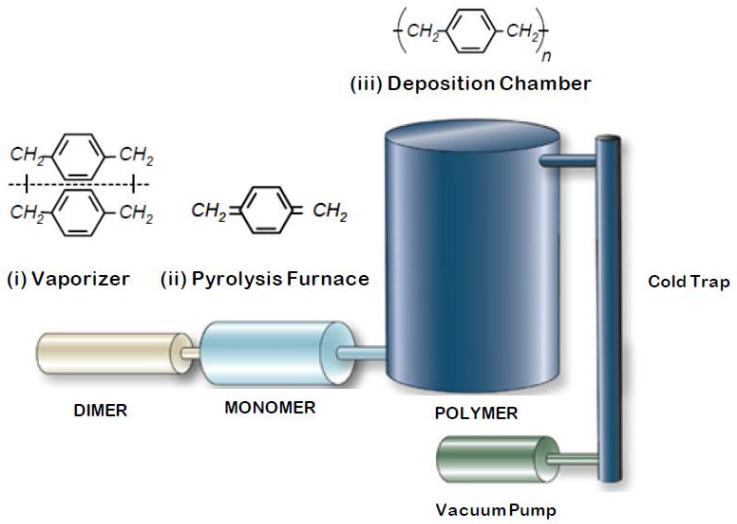

Figure 2.12 – Schematic illustration of the Parylene Deposition System (PDS).

The procedure begins by inserting a predetermined amount of the raw material (dimer) – a stable compound in granular form – inside the vaporizer. In general, the film thickness is proportional to the amount of dimer used, as showed by the set of experimental data plotted in Figure 2.13.

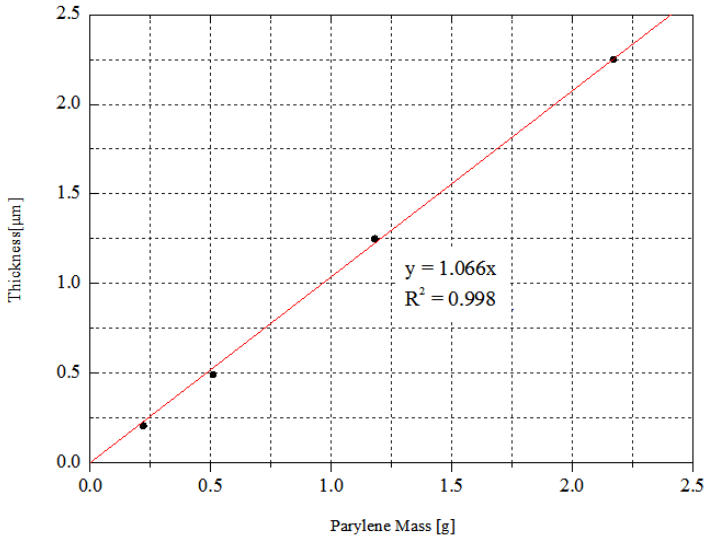

Figure 2.13 – Experimental relationship between film thickness and mass of parylene C inserted in the vaporizer (see text), employed in this project.

However, for thicknesses below a few hundred of nanometers, we found that the correlation is no longer linear, since other factors become relevant in determining the final film thickness, such as the deposition of additional parylene coming from the vacuum chamber walls. Thus, the cleanness of the system was crucial for the repeatability of the experiment.

By using 0.035 g of parylene C, almost the lowest amount that is possible to manipulate due to the granular form of the raw material, the thickness obtained was 93 ± 4 nm (as measured by profilometry).

After disposing the SiO_2/Si substrates inside the deposition chamber, the whole system is pumped down to ~10 mTorr, by means of a mechanical vacuum pump, and the vaporizer and the pyrolysis furnace are heated up to their process target temperature. When the temperature in the vaporizer ((i) in Figure 2.12) reaches 175 °C, the raw material starts to sublime and a dimeric gas is produced. Afterwards, the dimers flow in the pyrolysis furnace (ii) – heated up to 690 °C – and are cleaved into monomers. Subsequently, the monomer gas flows in the deposition chamber (iii) – kept at room temperature – and gets deposited on all the exposed surfaces, where the monomers link to each other to form the parylene polymer. The substrates in the chamber are located on a rotating sample-holder, which permits to further improve the parylene film uniformity. A cold trap, filled with liquid nitrogen, is used to take away the extra monomer vapor.

The average deposition rate for parylene C is about 5μm/h. However, together with system cleanness, also fluctuations of the base pressure and of temperature may result in changes of the deposition rate.

An AFM image of a 90 nm thick parylene C film is shown in Figure 2.8f. The RMS roughness of parylene C films is significantly larger than for PMMA and PS, 1.2 nm vs. ~0.15 nm. The film surface is less uniform but there are no traces of pinholes. The average water contact angle is of 85° ± 3° (Table 2.1). Finally, the layer capacitance (33 $nF \cdot cm^{-2}$), was calculated using the value of the low frequency dielectric constant provided by the vendor [74], i.e. 3.15 (Table 2.3).

2.3.3 Molecular Self Assembled Monolayers on SiO_2

Molecular Self-Assembled Monolayers (SAMs) have drawn growing interest in the field of organic electronics due to their ability to spontaneously form highly organized organic structures over the most commonly used dielectric surfaces, such as SiO_2 or aluminum oxide (Al_2O_3) [75].

SAMs provide an easy method to turn an inorganic surface into organic and to significantly change its properties. For instance, hexamethyldisilazane (HMDS) and octadecyltrichlorosilane (OTS), as a result of their favorable attachment to hydroxidized or oxidized surfaces, allow to lower significantly the surface energy of SiO_2 and to change its behavior from polar to non-polar [76-79]. Moreover, they reduce the density of hydroxyl groups, which are known to behave as electronic trap states limiting electron transport in the overgrown OS. Figure 2.14, extracted from reference [80], shows the chemical structure of the molecules of OTS and HMDS together with the SAMs resulting from the covalent bond of their headgroups with the siloxanes and silanols present on the substrate surface.

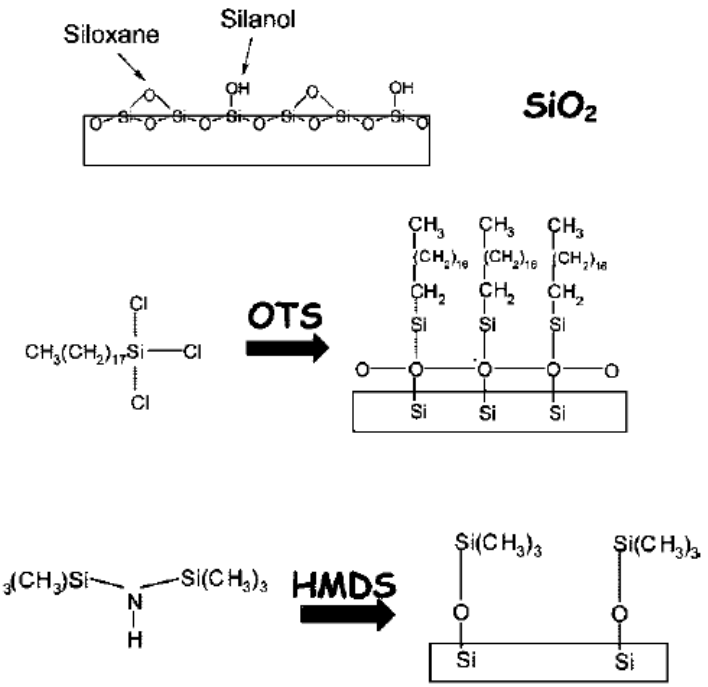

Figure 2.14 – (Top) SiO_2 substrate surface characterized by the presence of siloxanes and silanol groups. (Bottom) Chemical structures of OTS and HMDS (left) and corresponding SAMs (right). Extracted from reference [80].

Different procedures have been developed to improve the ordering and packing of the molecular chains in the OTS monolayer [81]. Among them, those from the vapor phase are often preferred to those from solution (e.g. dip-coating and spin-coating) where solvent related contaminations are possible. The different factors/dynamics involved in the two classes of processes give rise to distinct monolayer structures – crystalline or amorphous, densely or poorly packed – as pointed

out by Ito [75] and the results are not easily predictable. While OTS monolayers deposited from the vapor phase or by solution immersion are amorphous and poorly packed, those deposited by spin-coating (under specific atmosphere conditions) are ultra-smooth, crystalline, and densely packed.

Hereafter we describe the procedures used to prepare SAM of OTS and HMDS on SiO_2, from vapor phase and solution respectively. All commercially available chemicals were used as purchased without further purification. OTS (as well as HMDS) are stored inside an N_2 filled glove boxes with a concentration of water vapor and oxygen of a few ppm.

As mentioned in Section 2.1, the oxidized silicon wafers were cut into 2 cm × 2 cm pieces. The resulting samples were cleaned by a sequential ultrasonic bath in acetone and isopropanol and then dried under a nitrogen stream. Afterwards, substrates to be treated with HMDS were exposed to UV/Ozone for 20 minutes and then rapidly transferred inside a N_2 filled glove box. On the other hand, the samples to be treated with OTS were immersed in a freshly prepared Piranha solution (75% H_2SO_4, 25% H_2O_2) for 20 minutes and then rinsed abundantly with ultrapure deionized water. Beyond eliminating all the organic contaminants, the goal of this step was to "activate" the surface, by promoting the formation of silanol groups and making the surface highly hydrophilic. It has been proven that a thin film of water on the SiO_2 surface is necessary for the formation of a complete monolayer [77]. For this reason we left the samples in a beaker filled with highly pure boiling water for a few hours. After extracting the samples and drying them with a nitrogen blow, we checked the "total wetting" (zero contact angle) behavior of the surface by means of a drop of pure deionized water. The samples were then transferred in the glove box and, in order to avoid any aging effect, we immediately performed the silanization.

For the HMDS treatment, all operations were conducted under inert atmosphere, using a spin-coater integrated with the glove-box. Following procedures similar to those described in Section 2.3.1 and starting from different recipes available in the literature [22, 34, 59, 61] we spin-coated the HMDS solution on top of the SiO_2 on Si substrates. We deposited 200 µl of solution on the 2 cm x 2 cm sample, and successively we started the spinning (static dispense). We set 5 seconds as acceleration time, 60 seconds as spin time, and 2000 rpm as target spin speed. [82] After spin coating, the samples were annealed at 120 °C for 1 hour and then stored inside the glove-box. The resulting surfaces were investigated by means of AFM and water contact angle. Comparing

the AFM images in Figure 2.8e (HMDS on SiO_2) and Figure 2.8a-b-c (bare SiO_2, PS on SiO_2, PMMA on SiO_2) it can be observed that the silanization makes the surface significantly rougher, as witnessed by the higher value of the average RMS roughness (0.270 vs. ~0.15 nm – Table 2.1). The modification of the surface chemistry, i.e. the substitution of the polar –OH groups of silica with the non polar $–(CH_3)_3$-Si groups of the HMDS molecules, was proven by measuring the water contact angles of a non-treated and a treated surface. We observed that the contact angle increases considerably with the treatment, from 28° ± 2° (hydrophilic surface) to 68° ± 2° (hydrophobic surface), in good agreement with those reported in the literature [82].

The deposition of OTS was conducted in vapor phase, using the vacuum-oven system illustrated in Figure 2.15.

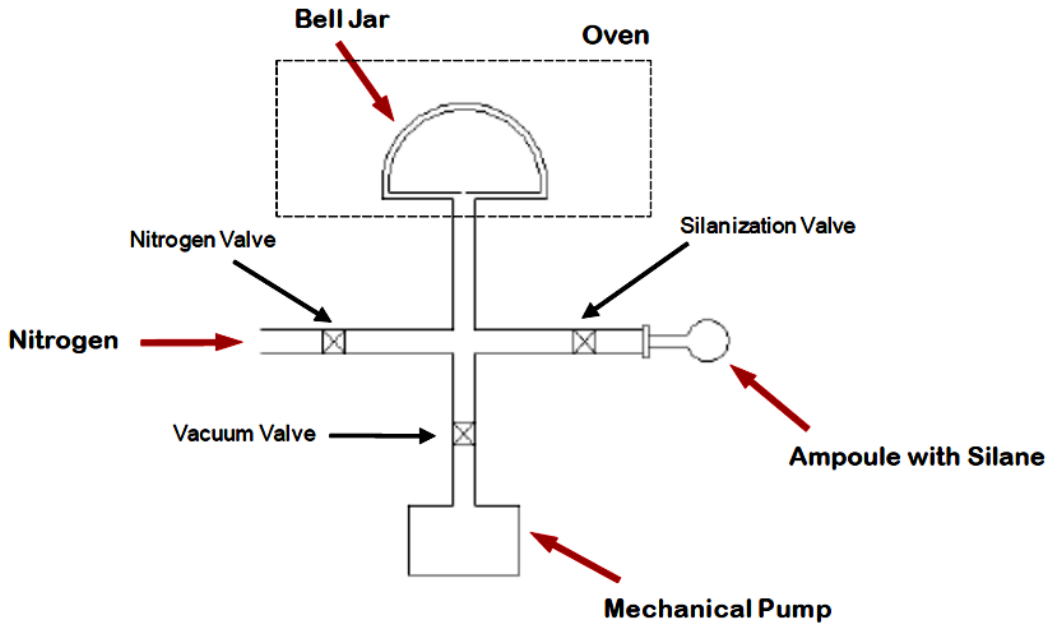

Figure 2.15 – Schematic illustration of the vapor phase silanization system used in this project.

A properly cleaned ampoule was inserted in the glove box and filled with the OTS liquid. Afterward, avoiding the exposure of the silane to the ambient atmosphere, we transferred the ampoule to the vacuum-oven and we connected it to the silanization arm (Figure 2.15). This procedure was conducted only for the first run, whereas for successive deposition runs we judged not necessary to replace the silane with a new one stored in the glove box. The OTS left in the ampoule was purified by freezing the ampoule with liquid nitrogen and then evacuating the contaminant gases.

The pre-cleaned substrates were positioned on the sample-holder inside the oven and then covered with a glass bell jar, provided with an appropriate gasket at the bottom. A mechanical pump was used to make the vacuum (about a few mTorr) inside the bell jar, while keeping the silanization valve and the nitrogen valve closed. The heating system was switched on and a target temperature of 110 °C – to vaporize the silane without inducing its chemical degradation – was set on the controller [59]. The temperature was monitored during the process by means of a thermocouple connected to the sample holder.

The time necessary for the stabilization of the temperature was about 1 hour. After that, we let OTS vapor entering the deposition chamber (bell jar), by interrupting the pumping (vacuum valve closed) and opening the silanization valve. The formation of a complete monolayer of OTS under dry conditions is known to be a slow process [59, 77], so that a deposition time of about 2 hours was considered to be necessary. Before removing the samples from the oven, we stopped the flow of silane (silanization valve closed), we reactivated the vacuum (vacuum valve open) and we increased the oven temperature to 120 °C in order to anneal the samples. The annealing step allows for the re-evaporation of the OTS not chemisorbed on the surface. Finally, we stopped both vacuum and heating, we vented the chamber (nitrogen valve open) and we remove the samples. Before being characterized, the substrates were ultrasonically rinsed in toluene and isopropanol to further remove the excess of silane.

The water contact angle, reported in Table 2.1, turned out to be 83° ± 2°, which confirms the successful modification of the surface chemistry and is a proof of high hydrophobicity. In addition, the AFM measurements (Figure 2.8d) revealed that OTS treated SiO_2 is slightly rougher than the HMDS counterpart (average RMS roughness: 0.3 nm vs. 0.27 nm).

2.4 Vacuum-sublimation of tetracene thin films

Nowadays, a variety of different techniques are available for depositing organic thin films, such as liquid deposition (e.g. drop-cast, spin-coating, blade coating), direct printing (e.g. contact stamp printing) and Physical Vapor Deposition (PVD, e.g. vacuum thermal evaporation) [7]. The type of process to be used is determined by both the properties of the material and the desired film characteristics/applications. For example, PVD techniques are not suitable for high

molecular weight materials, such as polymers, since they easily degrade before evaporating. Instead, organic small molecules, such as acenes, sublime at relatively low temperature (generally lower than 200 °C in high vacuum) and are easily deposited by thermal evaporation.

This technique has been widely used in the context of this research project to grow films of tetracene. Basically, it consists in the vaporization of the source material – under high or ultra-high vacuum (UHV) conditions – and in the condensation of the gaseous molecules on a cooler substrate. Although more expensive than other techniques, vacuum thermal evaporation is commonly employed and widely studied since it provides high purity films together with the possibility of an improved molecular ordering [83].

In this section we describe the equipment and the experimental set-up adopted for the tetracene deposition process. The multi source-evaporator integrated in a nitrogen-filled glove box, as shown in Figure 2.16a, was conceived for depositing both organic molecules and metals. It is provided with six independent sources, each one having its own shutter in the proximity and a quartz crystal microbalance (QCM) for monitoring deposition rate and thickness. Furthermore, a cross contamination shielding, constituted by radial fins (Figure 2.16b), avoids the deposition of contaminants on other sources and allows for co-evaporation processes.

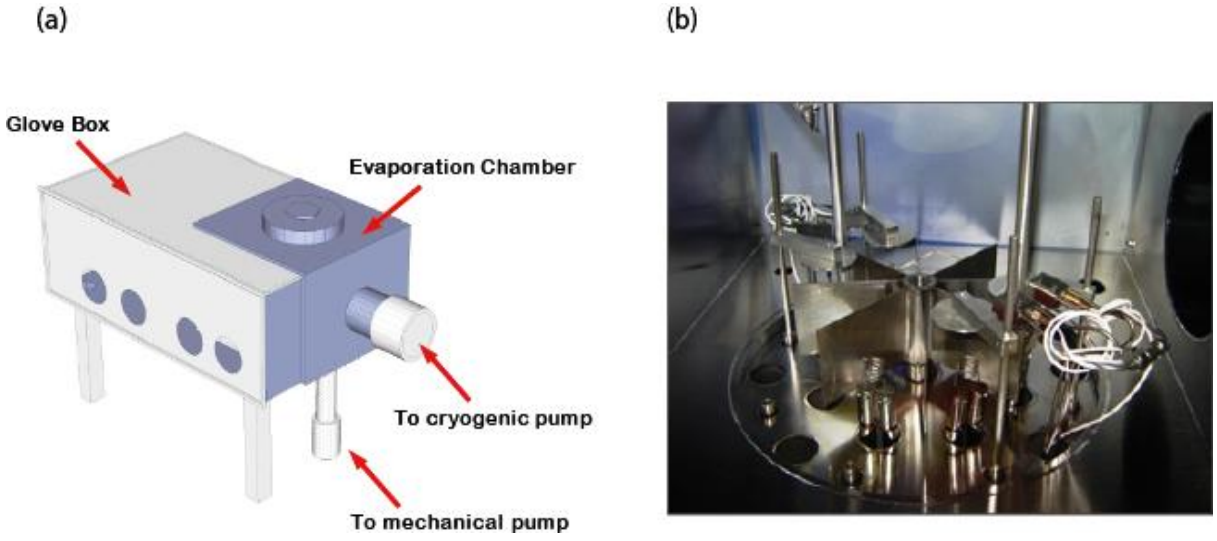

Figure 2.16 – (a) Schematic illustration of the glove-box integrated evaporator and (b) photograph of the multi-source evaporator for metals and organic molecules used in this project.

The evaporation chamber was evacuated by means of a mechanical pump, for the primary vacuum (down to 5×10^{-3} Torr) and a cryogenic pump for the high vacuum. The minimum achievable pressure inside the chamber was about 2.5×10^{-6} Torr, measured by a cold cathode ionization gauge (Penning gauge), located at the bottom of the chamber.

The system was used for the deposition of both tetracene and gold, as active material and top-contact electrodes, respectively. The integration of the evaporator with the glove box was essential for conducting the manipulations (Section 2.1) between OS and metal depositions.

The source material is heated by running large currents either through a metal foil boat (fashioned to contain the material to evaporate) or through a tungsten filament braided around an alumina crucible. Gold has been evaporated using the metal boat heater while tetracene using the crucible. In the first case, the source material is heated directly by the metal resistance: the heat produced by Joule effect is "lost" through the heat of fusion and vaporization of the metal, conduction into the electrodes (copper blocks), and emission of radiation [84]. In the second case, the source material is only indirectly heated, with no contact between the heating filament and the material to evaporate. This is interesting in view of the homogeneous heating and the reduced contamination achievable [7].

The tetracene deposition procedure begins by filling the crucible with tetracene powder (TCI, >97%) and positioning it inside the tungsten wire basket. The dielectric substrates, prepared according to the procedures described in Section 2.3, were fixed onto a 10 cm diameter metal disk (see Section 2.1), which acted as the sample holder. The latter was positioned 18 cm far from the source, without lateral displacement between the center of the disk and the source, as shown in Figure 2.17. In the system of cylindrical coordinates (L, h) illustrated in the figure, the center of the disk lies at the point (0 cm, 18 cm). The position of the QCM was measured to be (5 cm, 7 cm) and the material density on the microbalance controller was set to the correct value for tetracene (1.24 $g\cdot cm^{-3}$). The shutter – a 8 cm diameter metal disk – was set to the "closed" position, to accurately shield the sample allowing to the QCM to detect the evaporation rate.

After the vacuum inside the chamber had reached 2.5×10^{-6} Torr, we activated the power supply that controls the current flow through the tungsten filament around the crucible. During all the time, the temperature was measured by means of two thermocouples, one fixed to the crucible (thermocouple 1), the other to the sample holder (thermocouple 2), as schematized in Figure 2.17.

The temperature of the sample holder did not vary for more than 2 °C from a typical base temperature of 20 °C.

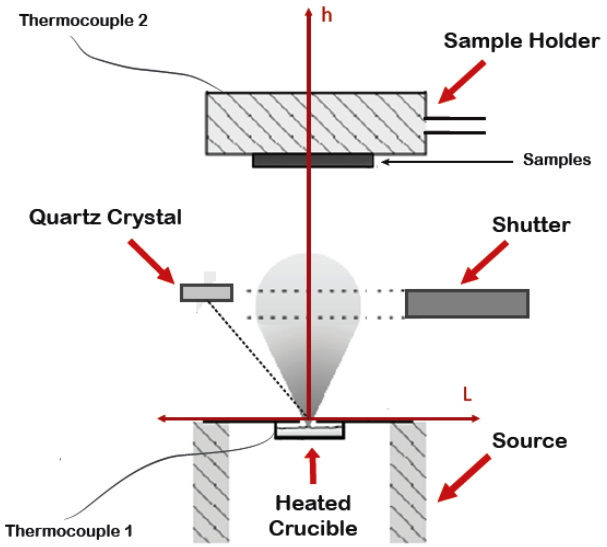

Figure 2.17 – Experimental set-up for tetracene vacuum-sublimation used in this project.

The heating of the source material was conducted gradually, by varying the current from zero to about 12 Amps in 20 minutes, until the temperature measured by thermocouple 1 achieved a value of approximately 190 °C (depending on the thermal contact between the crucible and the thermocouple). At this point, when the tetracene powder started to sublime, the QCM began to record a significant deposition rate and the current could be slowly increased to reach the desired deposition rate.

Afterward, the shutter was opened and kept open till the target thickness was displayed on the microbalance monitor. The current flow through the filament was slowly decreased and the system was let cooling down for about half an hour before refilling the chamber with nitrogen and opening it towards the glove box space. After each evaporation, the tetracene powder left inside the crucible was stored to be used for successive deposition runs. Significant desorption of tetracene has been observed when the substrates were left too long in high vacuum. This phenomenon was identified in the degraded performance of OFETs based on partially desorbed tetracene films, left in high-vacuum for more than 5 hours.

The deposition rate is known to play a key-role in determining the growth dynamics, the morphology and the properties of tetracene films. In a range between 0.1 and 5 Å/s, the higher the deposition rate, the higher the FET mobility [85]. We then set the deposition rate to 3.5 Å/s. This value was the highest possible deposition rate obtainable with our evaporation system without inducing a degradation of the source material by excessive heating. Increasing the deposition rate is also possible by reducing the sample-source distance; however for too low distances, the uniformity of the film can be compromised.

Choosing the thickness of organic films for application in top-contact OFETs must be done with special care. The amount of deposited material should be enough for complete substrate surface coverage but not too much to induce high contact resistance [86-88]. Considering these aspects, the thickness of the tetracene films employed for the fabrication of the OFETs was fixed to 50 nm. Hereafter, we describe the method adopted to control and achieve the target deposition rate and thickness at the sample.

Three evaporations were conducted to find the scaling factors between the thickness and deposition rate measured by the QCM and the effective thickness and deposition rate on the samples. The deposition time was recorded and the thickness of the resulting tetracene films was measured by means of profilometry. From these data we could evaluate the effective thickness and average deposition rate on the samples and relate them to the values measured by the QCM. The model adopted to relate the parameters is described in [84].

Considered that the QCM was approximately oriented as the plane containing the samples (see Figure 2.17), it was possible to apply the following equation, which gives the thickness d of material deposited over an elementary surface dS perpendicular to the h axis, at the point (L , h):

$$\mathrm{d} = \frac{\mathrm{K}}{\mathrm{h}^2 \left\{1 + \left(\frac{\mathrm{L}}{\mathrm{h}}\right)^2\right\}^{\mathrm{n}}} \tag{2.8}$$

n is a parameter which depends on the molecular emission profile generated by the source, and assumes a value of 1.5 in case of “point source” (spherical emission) and a value of 2 in the case of “planar source”. K is a constant related to the properties of the material and to the evaporation process. Using this equation it was possible to relate the thickness D_S on the sample (L_S, h_S) with the thickness D_Q measured by the QCM (L_C, h_C), obtaining:

$$\frac{D_S}{D_Q} = \frac{{h_Q}^2 \left\{1 + \left(\frac{L_Q}{h_Q}\right)^2\right\}^n}{{h_S}^2 \left\{1 + \left(\frac{L_S}{h_s}\right)^2\right\}^n} \tag{2.9}$$

By inserting the experimental data in relationship 2.3 we could determine an approximate value for the parameter *n*, which turned out to be about 1.5. This fact suggested that the emission of tetracene molecules from the crucible was characterized by an hemispherical profile.

Equation 2.8 and 2.9 were used to estimate the film thickness uniformity on a single substrate or the difference in film thickness for samples located at different positions on the sample-holder. As an example, we report in Table 2.4 the data relative to the deposition of 50 nm of tetracene with an average deposition rate of 3.5 Å/s. The corresponding values at the position of the microbalance, calculated using Equation 2.9, were used as a reference for the following evaporations.

The model allowed us to evaluate the thickness variation due to the lateral displacement in the plane of the sample holder. Two centimeters far from the center, the thickness changes by less than 2% while at the edges of the sample holder the variation is estimated to be about 10%.

Using the same model, we could analyze the film thickness uniformity at different sample-source distances. Reducing the distance to less than 18 cm, which could have been useful for achieving higher deposition rates, was judged inconvenient since it would have induced a too high variability among samples located at different positions on the sample-holder.

Position:	**QCM**	**Sample (center)**	**Sample ± 2cm**	**Sample ± 5 cm**
L [m]	0.05	0	0.02	0.05
h [m]	0.07	0.18	0.18	0.18
L/h	0.71	0	0.11	0.27
Thickness [nm]	**178.14**	**50**	**49.09 (-1.6%)**	**44.72 (-10.56%)**
Rate [Å/s]	**12.47**	**3.5**	**3.44**	**3.13**

Table 2.4 – Thickness and deposition rate of tetracene in the plane of the sample-holder (at the center, at 2, and at 5 cm from the center) and corresponding values at the QCM.

The lack in thickness uniformity was the reason for which we did not use a larger sample-holder to have all the six samples – bare SiO_2, PMMA, PS, parylene C, HMDS and OTS – in a single evaporation-run (Section 2.1).

In the context of the study of tetracene films' nucleation and growth (Section 3.1), sub-monolayer films of different nominal thicknesses (2, 5, 10, 17, and 35 nm) were vacuum-sublimed using a home-made thermal evaporator appositely dedicated to the deposition of organic molecules. The minimum pressure achievable inside the bell jar chamber was about 5×10^{-6} Torr. Once the vacuum was removed, the chamber was directly exposed to the ambient air. The deposition rate/thickness was monitored by means of a QCM located in close proximity to the sample-holder. The main difference with respect to the experimental set-up previously described, is the source-sample distance (30 cm vs. 18 cm). Under this condition, film thickness variation is not a concern so that all the six samples (about 1 cm × 1 cm) could be inserted in a single evaporation-run. The only issue was the larger source heating and time required for achieving a deposition rate of 3.5 Å/s at the position of the sample-holder.

Tetracene thin films deposited with one or the other systems were investigated by means of AFM. No significant difference was found in the morphological properties of the films.

2.5 Deposition of gold top-contact electrodes

The deposition of top-contact electrodes was the last step in the OFET fabrication process. As the electrode material we chose gold, which is a common choice due to its high air stability leading to the absence of native oxide layers resulting in unwanted injection barriers [7, 87]. The work function of gold is such that holes can be injected in the HOMO level of a number of OSs, while it generally forms significant energy barriers that limit the injection of electrons into the LUMO level of OSs (e.g. Figure 1.11).

The experimental set-up for the deposition of gold is equivalent to that presented in Section 2.4 for tetracene, so that we can continue to refer to Figure 2.17 for further discussion. The two only differences are the following: (i) a resistive boat was used instead of a crucible and (ii) the distance between source and samples was augmented in order to avoid a possible overheating of the samples due to the large amount of heat radiation emitted by the gold source.

Herein we want to discuss the use of thermal resistive heating in comparison with e-beam bombardment of the source material. This issue was brought to light during a poster presentation at the MRS Fall Meeting 2009 in Boston. As pointed out by Kymissis in reference [7], thermal resistive evaporation of metals is preferable when organic substrates are involved. The main reason lies in the fact that in case of e-beam evaporation – if the necessary precautions are not taken – a flux of backscattered electrons can reach the samples charging, degrading, or even decomposing the organic layer. Furthermore, IR/UV and X-Ray radiation can induce damage to the sample. Therefore, in the context of this research project, the use of thermal resistive evaporation was considered highly preferable. The problem of the heat radiation coming from the metal boat was not neglected. As reported by Cho [89], a long exposure to heat radiation affects the structure of molecular films. For this reason, we kept the samples at a larger distance from the source (about 34 cm) and we monitored the temperature throughout the course of the process. It was observed that the temperature in proximity of the samples – measured by thermocouple 2 – did not increase over 45 °C.

The procedure for depositing and patterning the top-contact electrodes is described in the following paragraphs.

After tetracene deposition, the sample-holder was extracted from the evaporation chamber and metal shadow masks were applied onto the samples, according to the procedure outlined in Section 2.1. One gold pellet (Kurt J. Lesker Company) was placed over the metal boat and the sample-holder was positioned over the source, with its center approximately at the point (0 cm, 34 cm). Minimizing the source-sample lateral displacement was found to be essential for a good transfer of the shadow mask pattern onto the substrates. The position of the QCM with respect to the source was measured to be (6 cm, 10 cm) and the material density on the QCM controller was set to the proper value for gold (19.32 $g \cdot cm^{-3}$). For the calibration of film thickness and deposition rate we adopted the same procedure described in Section 2.4 (i.e. conducting three evaporations, measuring the resulting film thickness by means of profilometry, and extracting the scaling factors). The results for a 50 nm thick gold layer deposited at 1 Å/s are reported in Table 2.5.

The process was conducted at a base pressure of 2.5×10^{-6} Torr, increasing the current with steps of 25 Amps/min from 0 to ca. 230 Amps, until the QCM started to detect the beginning of the

evaporation). Once the evaporation begun, the deposition rate becomes highly sensitive to variations of the current. When the flux measured by QCM was stable around 7.3 Å/s (which corresponds to about 1 Å/s on the samples), the shutter was opened to start the deposition.

Position:	**Quartz Crystal**	**Sample (center)**	**Sample ± 2cm**	**Sample ± 5 cm**
L [m]	0.06	0	0.02	0.05
h [m]	0.1	0.34	0.34	0.34
L/h	0.6	0	0.059	0.147
Thickness [nm]	**364.5**	**50**	**49.74 (-0.52%)**	**48.42 (-3.16%)**
Rate [Å/s]	**7.3**	**1**	**0.995**	**0.993**

Table 2.5 - Thickness and deposition rate of gold in the plane of the sample-holder (at the center, at 2, and at 5 cm from the center) and corresponding values at the QCM.

A nominal thickness of 50 nm was found to be enough for the formation of a continuous layer of gold over the granular structure tetracene films. This fact was judged by subsequent AFM and optical microscopy investigations.

As soon as the target thickness was achieved, the shutter was closed and the current was reduced gradually, in order to avoid thermal shocks. The system was let cooling down for about half an hour before removing the vacuum and extracting the samples from the evaporation chamber. The last step was taking off the shadow masks and dethatching the samples from metal disk. This operation required a special attention in order to prevent scratches and collisions that could drastically damage both the electrodes and the tetracene.

We conclude this section by presenting the details of the shadow masks employed for top-contact electrodes patterning. When dealing with organic substrates, it is not possible to take advantage of the well-established photolithographic techniques for metal deposition and patterning, since the use of resists and solvents induce the degradation of the organic material. Alternative solutions have been proposed [90]. However, shadow masking is still the most commonly employed technique, mainly because of its simplicity and versatility. Its main drawback lies in the minimum feature size (ca 30-50 μm).

The shadow masks were fabricated by Thin Metal Parts (Colorado, USA) – using laser ablation on stainless steel foils. The layout, designed by our research group, is reported in Figure 2.18.

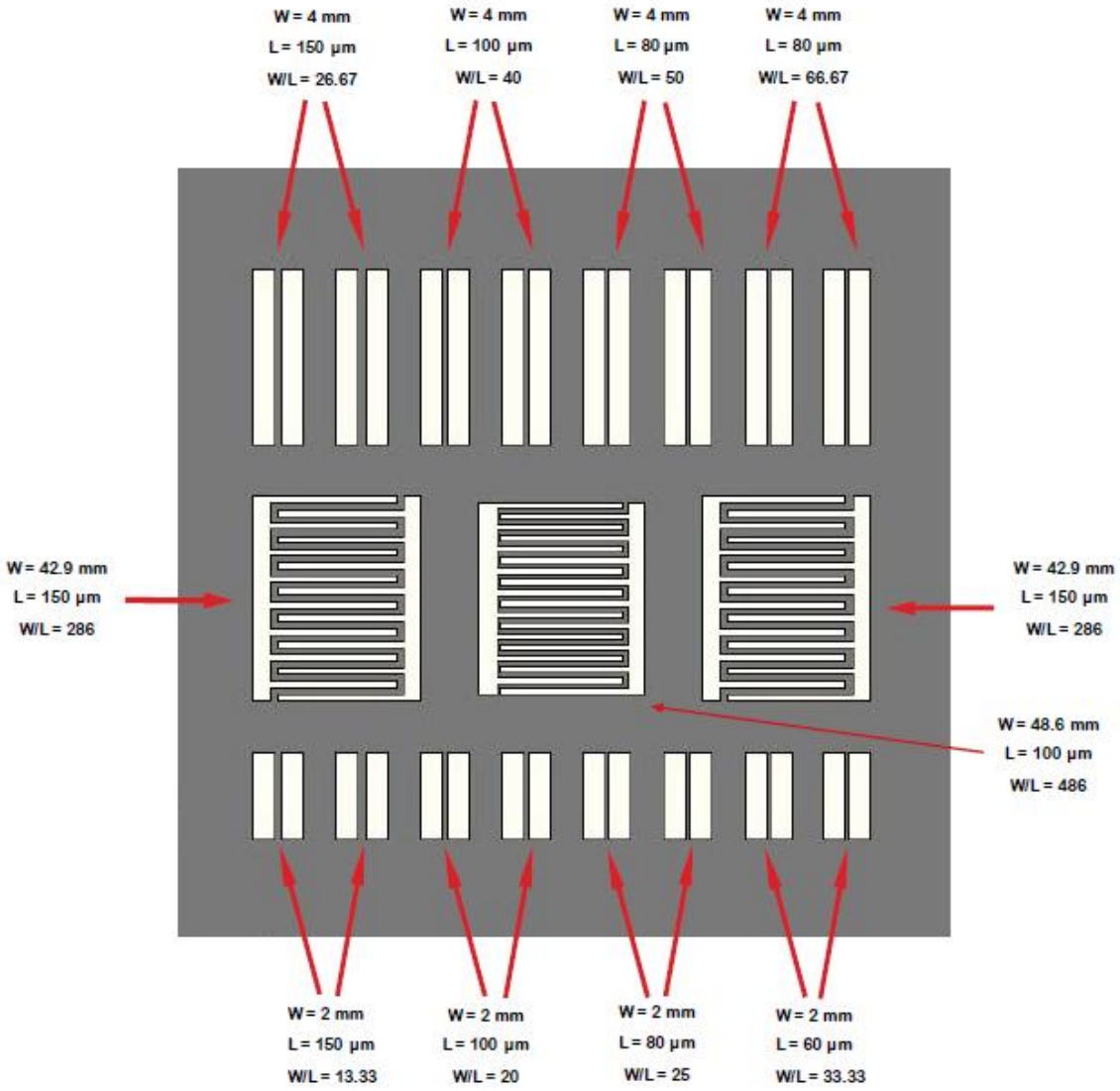

Figure 2.18 – Layout of the shadow mask used for the realization of the top-contact electrodes. Size: 18 mm × 18 mm. Thickness: ~250 µm.

In the first row (at the top), the rectangular electrodes couples are characterized by a constant channel width (W = 4 mm) and by a set of different channel lengths (L), namely 60 µm, 80 µm, 100 µm and 150 µm. The second row contains the interdigitated electrodes; due to the multiple finger-structure, the channel width increases linearly with the length and the number of fingers, allowing reaching W values of the order of few centimeters; L corresponds to the distance

between adjacent fingers. The third row (at the bottom) is equivalent to the first one, except that the channel width is reduced to 2 mm.

The layout was conceived with such geometry in order to: (i) provide a set of different channel lengths for the extraction of the contact resistance by the Transfer Line Method [88] (TLM), (ii) analyze the behavior of the FET current as a function of the W/L ratio (iii) obtain higher electroluminescence intensity from tetracene thin films (interdigitated electrodes).

Before completing the design of the aforementioned layout, two different "generations" have been produced and investigated. The "first generation" was characterized by 500 µm side squared electrodes separated by a 100 µm distance, resulting in a very small W/L. With such a geometry, as pointed out in [87], non-idealities may emerge due to the fringing field effect occurring at the edges of the transistor channel. The "second generation" had only interdigitated structures (one of these is shown in Figure 2.19a), with a relatively small channel length (80 µm). The main issue in the fabrication of these masks was the precision of the dimensions. This was limited by the laser spot diameter, by the heat transfer across the mask material, and by a structural fragility caused by the fact that the long metal serpentine is fixed only to two fragile spots of the 150 µm thick mask foil (indicated with two crosses). The geometrical tolerance guaranteed by the company was ± 12.7 µm, but the final result was indeed worse, as shown by a photograph taken at the optical microscope (Figure 2.19b). Notice that the metal wires should have had the same width everywhere in the image.

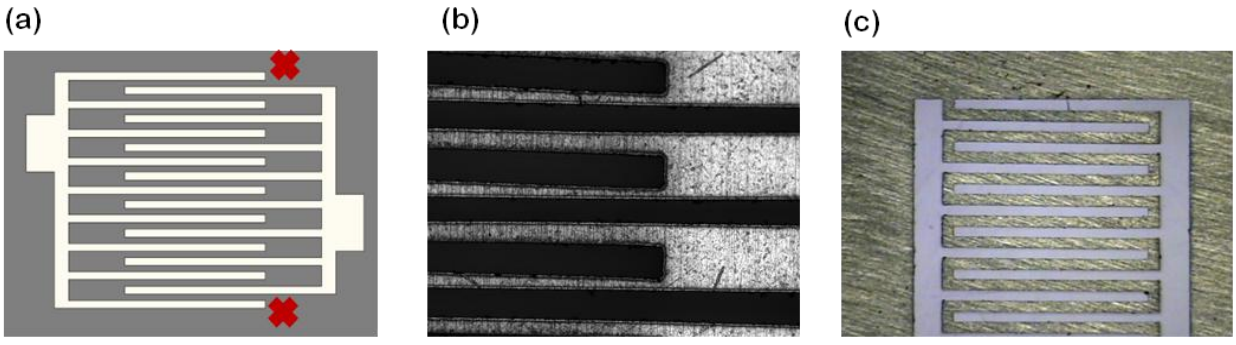

Figure 2.19 – (a) Interdigitated structure of the "second generation" shadow mask for top contact electrodes in tetracene FETs investigated in this project; (b) Optical microscopy photograph of the effective pattern ablated on the metal foil; (c) optical microscopy photograph of the "third generation" interdigitated structure.

Finally, the “third generation mask”, whose layout is reported in Figure 2.18, has both single-channel and interdigitated structures with fair aspect, as it can be inferred from Figure 2.19c. In order to achieve this result, it was necessary to set a larger channel distance (up to 150 µm) and to increase the stainless steel foil thickness up to 250 µm to achieve more robust metal structures.

Alternative strategies will be considered in the near future for higher resolution shadow masks. Among them: (i) micro-photo-electroforming [91] and (ii) silicon shadow masks, realized by means of side-to-side etching of thin silicon wafers [92-93].

We conclude this section by presenting a three dimensional layout of the top-contact interdigitated OFET microfabricated using the “third generation” shadow mask.

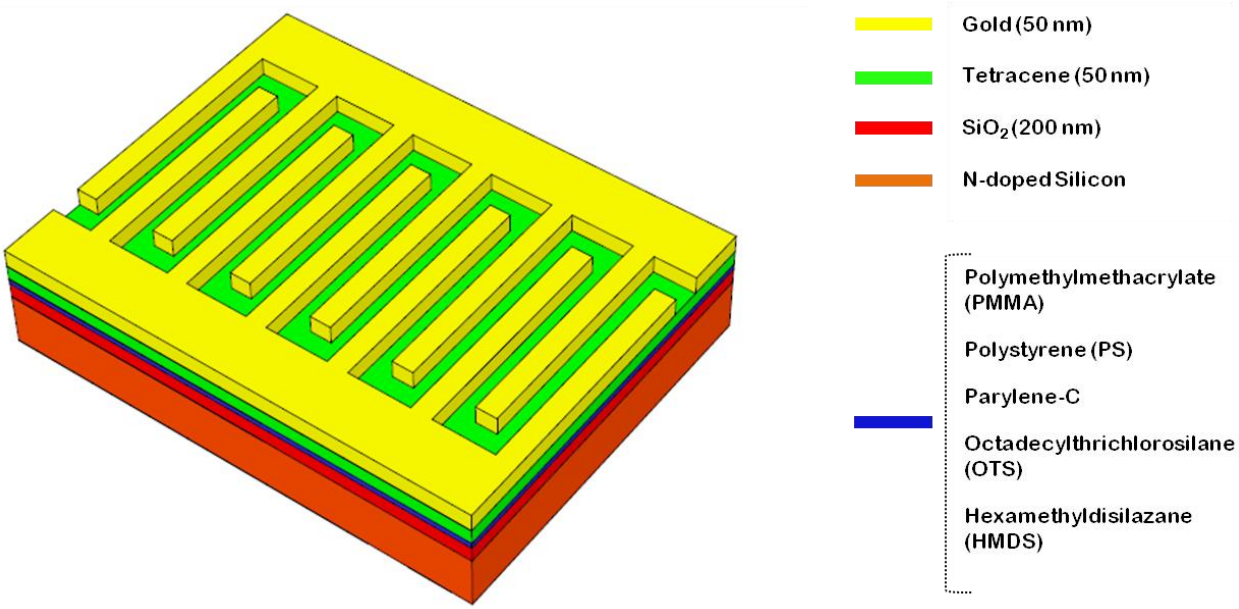

Figure 2.20 – Three dimensional representation of the final interdigitated top-contact OFET investigated in this project.

Chapter 3. RESULTS AND DISCUSSION

This chapter presents (i) the experimental investigations conducted on polycrystalline tetracene films deposited on the polymeric layers and SAMs and (ii) the results of the electrical characterization of the OFETs based thereon. The scientific problems addressed here concern the role of the dielectric layer in determining the performance of tetracene OFETs and the correlation between growth/morphology and FET mobility.

Section 3.1 deals with the results of the AFM investigation at sub-monolayer and complete substrate coverage of tetracene films grown on six different dielectric surfaces, namely bare SiO_2 (reference substrate), OTS treated SiO_2, HMDS treated SiO_2, parylene C on SiO_2, PS on SiO_2 and PMMA on SiO_2. In the early stages of growth, the nucleation density and the islands shape/size depend on the dielectric surface properties. At complete substrate surface coverage, films deposited on different substrates are characterized by significantly different RMS roughness and grain sizes.

In Section 3.2, the tetracene OFETs characteristics are reported. In previous publications [85] it was shown that in tetracene films the charge carrier mobility can be increased over two orders of magnitude (up to $4 \cdot 10^{-2}$ $cm^2V^{-1}s^{-1}$ – average value reported in [85]) by controlling the deposition flux. We will show here that the FET mobility can be further improved by a careful choice of the dielectric surface. The use of the aforementioned dielectric substrates results in FET mobility values ranging between $1 \cdot 10^{-2}$ (bare SiO_2) and $2 \cdot 10^{-1}$ $cm^2V^{-1}s^{-1}$ (PS on SiO_2).

Section 3.3 is dedicated to the analysis of the experimental data presented in the two previous sections, to understand the role of the dielectric layer and to shed light onto a possible correlation between films' growth/morphology and charge carrier transport properties.

Each dielectric substrate – being characterized by specific chemical and physical properties, such as the presence of polar/non polar groups in the molecular structure of the dielectric or the dielectric permittivity – leads inevitably to different distributions of the electronic states' densities at the interface, which may be responsible for the "quality" of the charge carrier transport [36].

Charge carrier transport and electroluminescence in OFETs and OLEFETs based on polycrystalline thin films are influenced by the crystal structure, the size/arrangement of the

crystalline grains and the orientation of the molecules inside the crystalline cell. To this purpose, Grazing Incidence X-Ray Diffraction (GIXRD) studies have been conducted at the synchrotron facility ELETTRA (beamline XRD1, Trieste, Italy – 12/15 May 2010) to investigate the correlation between the structure/texture of the polycrystalline tetracene films – at the dielectric/semiconductor interface – and the OFET performance. The analysis of the synchrotron data is in progress. We postpone their presentation and discussion to near-future papers.

As mentioned in Section 1.4, the long-term objective of this project consists in providing an answer to the question of whether it is possible to achieve an ambipolar transport in thin films of tetracene by means of dielectric surface engineering. The demonstration of ambipolarity in polycrystalline tetracene films deposited on organic dielectric substrates would represent a further proof of the "general observation of n-type behavior in organic semiconductors" – reported by Chua et al. [21] – and would lead to higher light emission efficiency from tetracene OLEFETs.

Presently, ambipolarity and electroluminescence in top-contact tetracene OFETs/OLEFETs (employing gold as the electrode material) have not been observed, despite the number of different dielectrics employed, as discussed in Section 3.4.

3.1 Nucleation and Growth of Tetracene Thin Films

The number of studies focusing on tetracene growth is limited compared to those dedicated to other more popular OSs. As an example, for pentacene a "layer-by-layer" growth has been observed on several dielectric surfaces. Literature reports indicate that tetracene thin films usually present an island growth mode, characterized by "granular growth structures". For the first time, in 2008, Qin et al. reported a "layered morphology" for tetracene thin films grown on SiO_2 [94]. They achieved this result by using a low deposition rate (0.5 Å/s) and a pressure inside the evaporation chamber lower than 3×10^{-9} Torr; the substrate were kept at room temperature.

We investigated the nucleation and growth of tetracene films on six dielectric surfaces, grown with a deposition rate of 3.5 Å/s and at a base pressure of 2.5×10^{-6} Torr.

This work represents a contribution to extend the present knowledge of tetracene, an OS that offers a good combination of electrical and optical properties [9] for applications in OFETs, OLEFETs and also phototransistors [95-96].

The process of nucleation and growth of tetracene thin films was investigated using *ex-situ* AFM. Tetracene films were vacuum sublimed on the six different substrates at six different nominal thicknesses: 2, 5, 10, 17, 35 and 50 nm.

After stating the reasons for studying the "interfacial" properties of OSs (Section 3.1.1) and introducing a few general arguments about the growth of organic thin films (Section 3.1.2), we will present the results on the early stages of tetracene growth (2 and 5 nm – Section 3.1.3), the islands growth and coalescence (10 and 17 nm – Section 3.1.4) and the complete substrate coverage films to be used in device applications (35 and 50 nm – Section 3.1.4).

3.1.1 Introduction: the role of the early stages

A fundamental goal of the research in organic electronics is the possibility to control the properties of organic thin films at interfaces [97]. This is particularly important in the case of OFETs, where the transistor channel – i.e. the region of the semiconducting film where the charge carrier transport occurs – extends only for a few nanometers far from the semiconductor/dielectric interface. Consequently, the final device performance is mostly determined by the properties of the organic film in the very proximity of the dielectric surface, while the semiconductor bulk-properties play only a minor role [24, 36].

Regarding the case of small organic molecules, such as pentacene and tetracene, vacuum deposited over dielectric substrates, the following aspects should be considered (A and B).

(A) The early stages of growth of organic polycrystalline films set the basis for the final film morphology. The nucleation and growth (e.g. nucleation density, island size distribution and island shapes) determine the nano and microstructure of the film. In general, a layer-by-layer growth (see Section 3.1.2) tends to form large crystalline grains and non-detrimental grain boundaries during coalescence, leading to high FET mobility [34, 98]. On the contrary, thin films characterized by a three-dimensional island growth (see Section 3.1.2), tend to form small crystalline grains and more detrimental grain boundaries that limit the current flow in the transistor channel.

(B) The orientation/arrangement that the molecules assume in the first monolayer not only influences the structure of the successive molecular layers, but also determines the efficiency of the charge carrier transport. In fact, flat-lying molecules, vertically standing molecules, or tilted

molecules may give rise to significantly different transistor behaviors [59]. As pointed in [34], higher FET mobility is commonly attained when the π-π stacking direction is parallel to the direction of the current flow; however, this is not a principle of general validity, and careful analysis must be conducted for each specific molecular semiconductor and dielectric surface [34]. Achieving the ability to control the orientation of the molecules at the interface with the dielectric is a key step towards the realization of high performance OFETs.

In conclusion, the need to understand the properties of the organic semiconducting films at the interface requires the investigation of the initial film layers.

In the context of this research project, the nucleation and growth of the films (aspect A) has been investigated by depositing and analyzing sub-monolayer films with different nominal thicknesses by means of AFM. On the other hand, the investigation of the molecular arrangement/ordering (aspect B) in the first layers has been conducted by means of GIXRD.

3.1.2 General considerations on the growth of organic films

When studying the growth of organic films it is important to recognize that organic molecules cannot be considered isotropic "point-like particles" since they possess a sort of nanostructure, characterized by orientational, conformational and vibrational/rotational degrees of freedom [99]. This fact renders the growth mechanism more complex compared to inorganic materials and models able to include anisotropic molecule-molecule and molecules-substrate interactions are needed.

Notice that both thermodynamic and kinetic aspects govern the film-formation process. Kinetic aspects deal with processes such as diffusion and nucleation [100]. For organic films, the possibility exists that the kinetics of growth induces the formation of non-equilibrium structures as deduced by "post-growth reorganization" phenomena [34, 100], proving that both thermodynamics and kinetics must be taken into account.

Similarly to inorganic films, three growth modes have been observed for organic molecular films, i.e. Vollmer-Weber (island), Frank-van-der-Merwe (layer-by-layer) and Stranski-Krastanov (layer plus island). Figure 3.1 shows the different growth modes and the relations among the three interfacial surface energies – i.e. the substrate surface energy $\gamma_{substrate}$, the film surface energy γ_{film}, and the film-substrate interface surface energy $\gamma_{interface}$ – resulting in a specific

growth mode. Notice that these relations, which come from thermodynamic arguments, represent useful but non-rigorous references for the prediction of the growth mode.

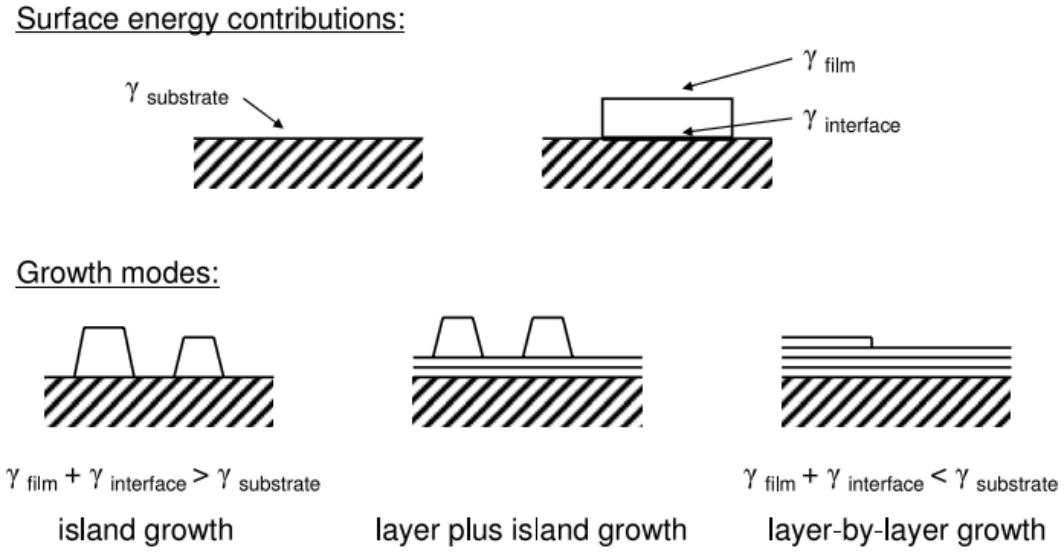

Figure 3.1 – (Top) Interfacial surface energies involved in the nucleation and growth process of thin films. (Bottom) Schematic illustration of thin film growth modes: Vollmer-Weber (island growth), Stranski-Krastanov (layer plus island growth) and Frank-van-der-Merwe (layer-by-layer growth). Image extracted from reference [100].

In Vollmer-Weber growth mode the molecule-molecule interactions are stronger than the molecule-substrate interactions, i.e. $\gamma_{film} + \gamma_{interface} > \gamma_{substrate}$: small clusters nucleate on the substrate surface and grow into three dimensional islands. In Frank-van-der-Merwe growth mode, the intermolecular interactions are weaker than the molecule-substrate interactions, i.e. $\gamma_{film} + \gamma_{interface} < \gamma_{substrate}$: the molecules tend to be adsorbed on the substrate instead that on pre-existing clusters. Ideally, a complete layer is formed before successive layers begin to form. Finally, in the case of Stranski-Krastanov growth mode, the features of the two previous growth modes are combined: initially one or more complete layers form; when a "threshold" thickness is reached, layer-by-layer growth becomes unfavourable – since the influence of the substrate diminishes while the intermolecular interactions become dominant – and three dimensional islands start to grow on top of the complete layers.

The substrate surface energy $\gamma_{substrate}$ can be viewed as a parameter for tailoring the nucleation and growth mode, and thus the microstructure, of the overgrown organic films, as discussed in Section 3.1.1, aspect A.

Before concluding this section, we want to clarify some terminological uses. The term "grain" is used in the literature to indicate a "crystalline grain" or "crystalline domain". The same word is often used (as is the case of this text) when dealing with AFM images of granular films. Besides that, in this work the word "particle" has been used as synonym for "island".

3.1.3 The early stages of tetracene growth

In Figure 3.2 and Figure 3.3, AFM images of tetracene films with nominal thicknesses of 2 and 5 nm are reported. For each type of substrate and each nominal thickness, at least four different AFM images, in four different locations of the samples, have been analyzed. We consider the images presented in this text as representative of the sample under examination. The elaboration of the data has been conducted with the software WSxM v.5.0 [49].

The two sets of AFM images reveal that islands are formed on all the substrates but with different densities, sizes, and shapes. This variability can be associated to the different properties of the dielectric substrate, among which the substrate surface energy. Approximate values of this parameter, as extracted from the literature and from polymer properties databases [79, 101-103], are reported in Table 3.1. The deposition/processing techniques as well as the values of the water contact angles reported in the literature [79] are both similar to those reported in this study. This suggests that the surface energy of our dielectric substrates should not be considerably different from the values indicated in Table 3.1. However, we will use these values only for qualitative discussion.

	Bare SiO_2	**OTS**	**HMDS**	**PARY C**	**PS**	**PMMA**
$\gamma_{substrate}$	~60 $mJ \cdot m^{-2}$ [79]	~28 $mJ \cdot m^{-2}$ [79]	~45 $mJ \cdot m^{-2}$ [79]	~60 $mJ \cdot m^{-2}$ [101]	~41 $mJ \cdot m^{-2}$ [102-103]	~ 44 $mJ \cdot m^{-2}$ [102-103]

Table 3.1 – Values of the surface energy for the dielectric substrates investigated in this project, extracted from the literature [79, 101] and from polymer properties' databases [102-103].

Figure 3.4 shows the histograms of the particle density (a) and average island surface area (b) for 2 nm (left column) and 5 nm (right column) nominal thickness films. The error bars associated to each column represent the maximum and minimum value obtained from the analysis of four AFM images. The histograms will guide us in the discussion of the early stages of growth; they illustrate the change in island density and size with the film thickness.

In Table 3.2 (enclosed is a set of AFM images from where the data have been extracted) and Table 3.3 we report, for all the dielectric substrates, the data relative to (i) the degree of substrate surface coverage, (ii) the island density, (iii) the average distance between the geometrical centers of the first neighbor islands, (iv) the sub-monolayer film RMS roughness and (v) the average particle surface area. In Figure 3.5 we report the height distributions of a set of 5 nm nominal-thickness AFM images (shown in the figure insets). The software WSxM counts the number of (i,j) points whose corresponding z-height value is included in the range $(z, z+\Delta z)$, with $\Delta z \approx 0.525\, nm$. The location on the x-axis of the "right" peak can be viewed as the island "modal" height. On the other hand, the "left" peak is related to the underlying substrate and thus has been intentionally shifted to the 0 nm height level [104]. This was found to be consistent with the profile analysis conducted on substrate-island steps. The counting/characterization of the islands was conducted using the WSxM "flooding" function, which identifies the AFM image pixels with a $z(i,j)$ value larger than a threshold-height that must be carefully set between the two peaks. The counting/characterization of the islands was conducted using the WSxM "flooding" function, which identifies the AFM image pixels with a $z(i,j)$ value larger than a threshold-height that must be carefully set between the two peaks. As an example, the threshold-heights for the AFM images shown in the insets of Figure 3.5 were selected as follows: (a) ~5.5 nm; (b) ~5 nm; (c) ~3 nm; (d) ~6.5 nm; (e) ~3.5 and (f) ~4 nm.

Referring to Figure 3.4 and considering the case of bare SiO_2 (reference substrate), one can observe that the particle density increases significantly when adding new material (i.e. from 2 to 5 nm) while the average particle surface area remains approximately constant. Therefore, the increase in substrate surface coverage and the decrease in the first neighbor distance (see Table 3.2 and Table 3.3) are due to the increase of the island density. Moreover, by measuring by AFM the vertical profile of the islands, it has been observed that high three-dimensional islands exist from the very beginning of the growth.

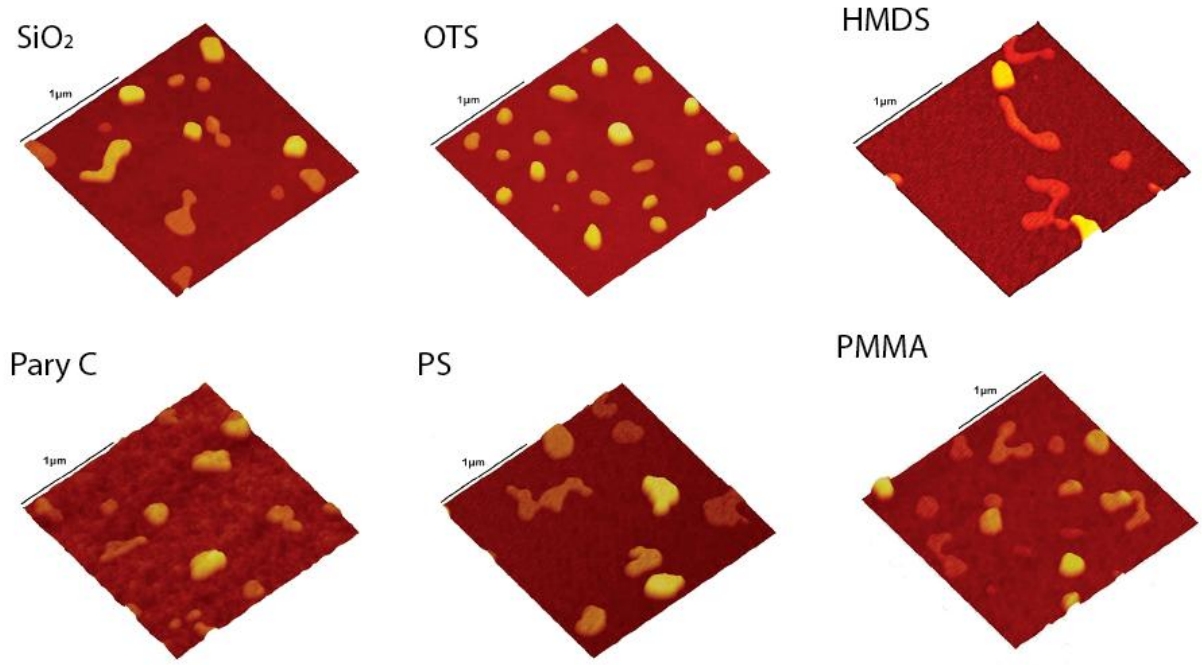

Figure 3.2 – AFM images of vacuum sublimed tetracene films with nominal thickness of 2 nm, deposition rate of 3.5 Å/s. Scale bars denote 1 µm.

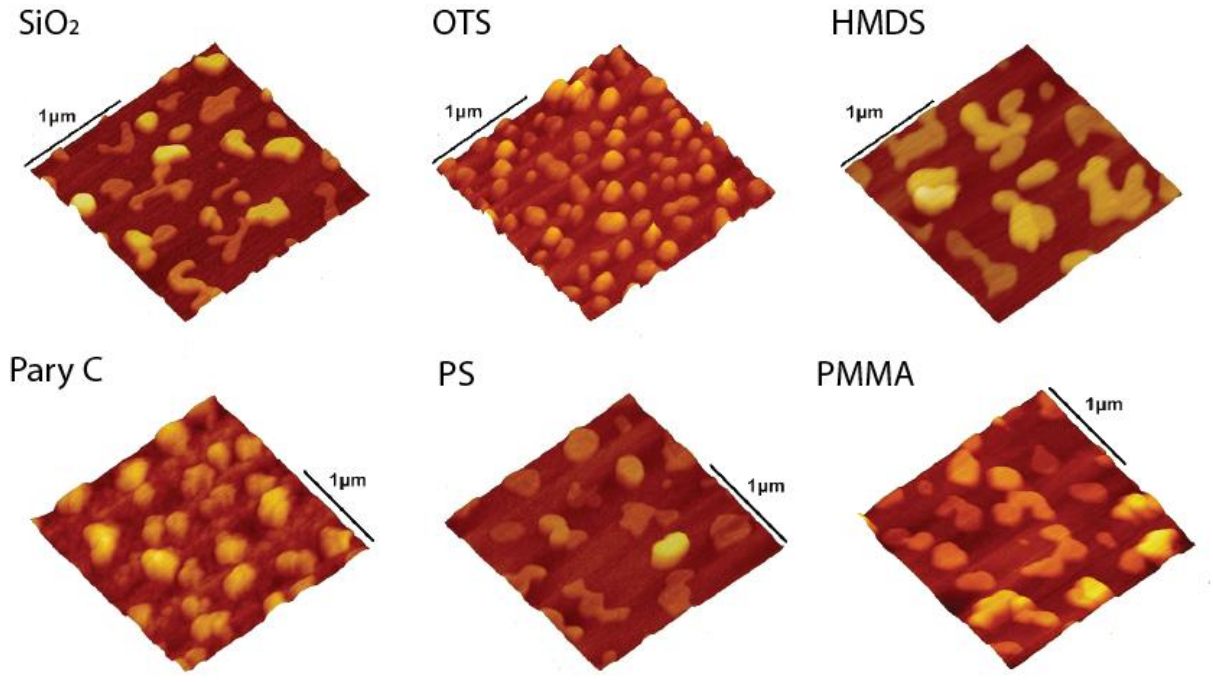

Figure 3.3 – AFM images of vacuum sublimed tetracene films with nominal thickness of 5 nm, deposition rate of 3.5 Å/s. Scale bars denote 1 µm.

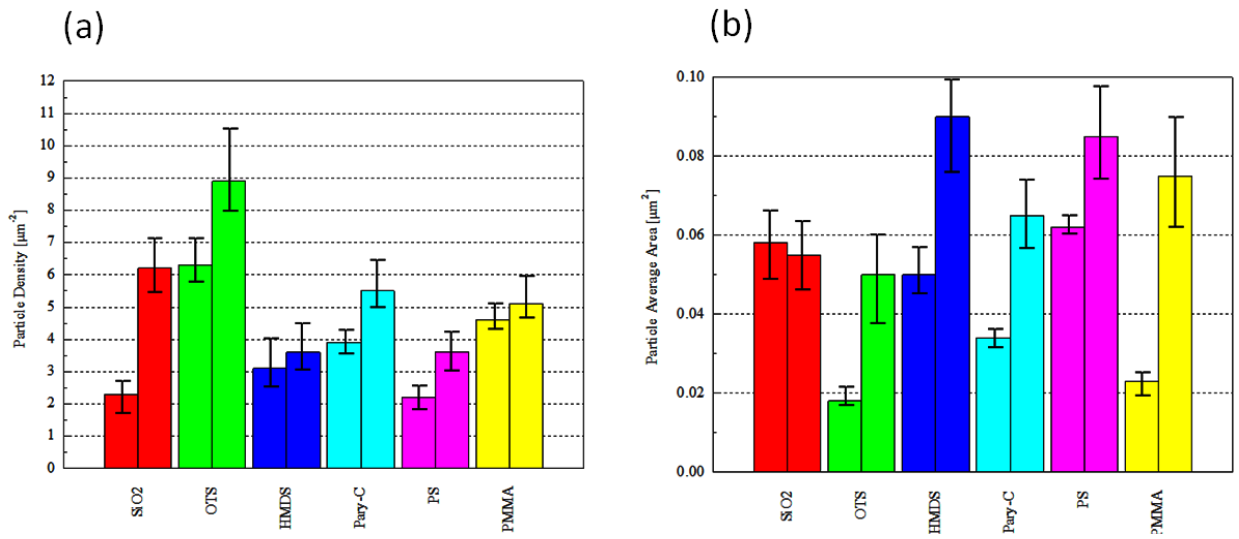

Figure 3.4 – Particle density (a) and average island surface area (b) for sub-monolayer tetracene films with nominal thicknesses 2 nm (left) and 5 nm (right). The error bars denote the minimum a maximum value obtained in four distinct AFM images for each substrate.

This can be inferred also by observing the height distribution diagram reported in Figure 3.5a for a 5 nm nominal-thickness sub-monolayer film, where the "right" peak lies at about 11.5 nm. Notice that the height of a single molecular layer, presumably constituted by vertically standing molecules, should be of the order of 1.3 nm, i.e. close to the long-axis length of the tetracene molecule (1.353 nm, Figure 1.10 [32]). Several low-height flat islands (~6-7 nm high) characterized by a variety of different shapes (see Figure 3.3, SiO_2) have also been observed.

The opposite scenario occurs in the case of HMDS and PMMA substrates. The particle density does not seem to vary significantly going from 2 to 5 nm; on the contrary, the average island area increases appreciably (see Figure 3.4). This indicates that "new" material is prevalently added to pre-existing islands. The 5 nm nominal-thickness AFM images of sub-monolayer tetracene films deposited on HMDS treated SiO_2, reveal relatively flat and large islands, characterized by nearly two-dimensional structures.

In the case of PMMA (Figure 3.5f) the peak is broad and it is located at ca. 8.5 nm. We measured the profile of several islands and it turned out that flat large islands coexist with small three dimensional ones.

Average Values:	Bare SiO_2	OTS	HMDS	PARY C	PS	PMMA
Coverage [%]	13.5 ± 2	11.5 ± 3	14.5 ± 3	13.5 ± 2	14 ± 2	15 ± 2
Particle Density [μm^{-2}]	2.3 ± 0.5	6.3 ± 0.7	3.1 ± 0.8	3.9 ± 0.3	2.2 ± 0.3	4.6 ± 0.2
1st neighbor distance [nm]	450 ± 30	275 ± 50	375 ± 80	350 ± 20	475 ± 20	350 ± 30
RMS roughness [nm]	5.4 ± 0.2	6.1 ± 0.2	4.0 ± 0.4	6.2 ± 0.2	5.4 ± 0.2	5.5 ± 0.2
Particle Area [μm^2]	0.058 ± .015	0.018 ± .004	0.050 ± .010	0.034 ± .005	0.062 ± .005	0.023 ± .010

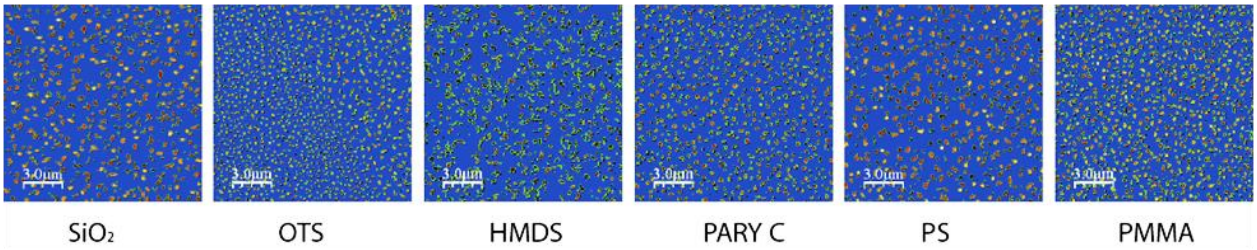

Table 3.2 – Properties of the sub-monolayer tetracene films (nominal thickness 2 nm, deposition rate 3.5 Å/s) calculated by means of WSxM software. Average values and error bars were evaluated from four different AFM images. A set of 15 μm × 15 μm AFM images where the tetracene islands were identified and characterized, is reported below the table.

Average Values:	Bare SiO_2	OTS	HMDS	PARY C	PS	PMMA
Coverage [%]	31 ± 2.5	44 ± 7	33 ± 4	35.5 ± 2	30.5 ± 2	35 ± 4
Particle Density [μm^{-2}]	6.2 ± 0.9	8.9 ± 1.5	3.6 ± 0.7	5.5 ± 0.7	3.6 ± 0.6	5.1 ± 0.9
1st neighbor distance [nm]	300 ± 30	180 ± 60	360 ± 30	310 ± 30	370 ± 40	340 ± 30
RMS roughness [nm]	7.5 ± 0.2	11.5 ± 1.5	6.8 ± 0.5	7.6 ± 1.0	6.4 ± 0.8	6.9 ± 0.8
Particle Area [μm^2]	0.055 ± .015	0.050 ± .020	0.090 ± .025	0.065 ± .015	0.085 ± .025	0.075 ± .030

Table 3.3 – Properties of the sub-monolayer tetracene films (nominal thickness 5 nm, deposition rate 3.5 Å/s) calculated by means of WSxM software. Average values and error bars were evaluated from four different AFM images. A set of 10 μm × 10 μm AFM images from where the tetracene islands were identified and characterized is reported in the insets of Figure 3.5.

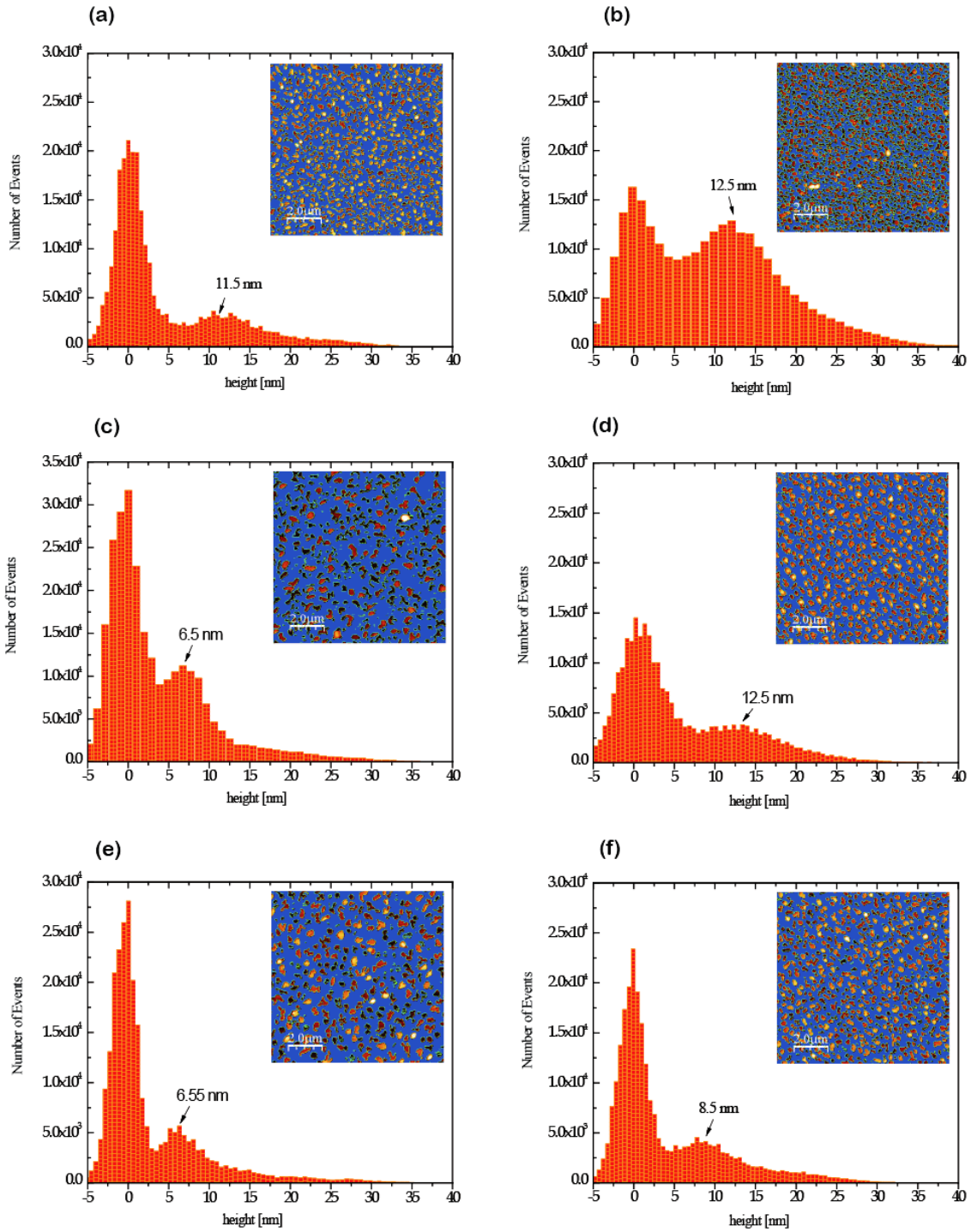

Figure 3.5 – Height distribution analysis of sub-monolayer tetracene films (nominal thickness 5 nm, deposition rate 3.5 Å/s) deposited on different dielectric layers: (a) bare SiO_2; (b) OTS; (c) HMDS; (d) parylene C; (e) PS; (f) PMMA. The histograms were obtained by means of the software WSxM (see text for details). The figure insets represent the AFM images from where the information were extracted.

Similarly, a number of flat and large islands can be found over the PS surface. This is indicated by the pronounced peak in Figure 3.5e – at about 6.5 nm – and by the remarkable island average area reported in Figure 3.4b.

Notice that, according to Table 3.1, the values of the surface energies of PS, PMMA and HMDS are close to each other, suggesting an explanation for the similar growth behavior.

Among all the employed dielectric substrates, OTS treated SiO_2 has the lowest surface energy and presents the highest density of small three-dimensional islands. This can be deduced directly from the observation of the AFM images of Figure 3.2 and Figure 3.3. With a low substrate surface energy, the relation $\gamma_{substrate} < \gamma_{film} + \gamma_{interface}$ (Section 3.1.2) can be easily satisfied so that a three-dimensional growth mode is strongly favored.

OTS is a well known SAM in the field of organic electronics because films of OSs grown on OTS usually perform better in term of charge carrier mobility compared to films grown on bare SiO_2. The reasons are (i) OTS can passivate interfacial electronic trap states (e.g. silanol groups on a SiO_2 substrate) and (ii) OTS promotes a higher OS nucleation density thus permitting to improve the substrate surface coverage [81].

We can observe that films on OTS are characterized by the highest particle density – at both 2 and 5 nm of nominal thickness – compared to all the other dielectric layers. Adding new material, from 2 to 5 nm, results in an increase of both island density and island area (Figure 3.4) that combined together favor the substrate surface coverage (~44% at 5 nm of nominal thickness, as indicated in Table 3.3). The islands are clearly three-dimensional. At 5 nm of nominal thickness the right-peak assumes a value of 12.5 nm (Figure 3.5b). The peak is pronounced but broad and the height distribution presents non-negligible values even beyond 20 nm. Moreover, the sub-monolayer tetracene films deposited on OTS are characterized by a significantly high RMS roughness (~11.5 nm at 5 nm of nominal thickness, as indicated in Table 3.3) which is induced by the large number of high three-dimensional particles.

The last dielectric substrate left to discuss is parylene C. Similarly to OTS, both an increase of particle density and particle area occur from 2 to 5 nm of nominal thickness (Figure 3.4). The islands are prevalently three-dimensional. Notice that, according to Table 3.1, the surface energy of parylene C is similar to that of bare SiO_2 (~60 $mJ \cdot m^{-1}$). However, its high RMS roughness (1.2

nm, see Table 2.1) is believed to play a role in the nucleation process, limiting the diffusion of the molecules on the substrate surface.

3.1.4 Island growth and coalescence

In this section we present the AFM images of the 10 and 17 nm nominal thickness tetracene films deposited over the six dielectric substrates investigated in this project.

Figure 3.6 shows a set of 10 μm × 10 μm AFM images of the 10 nm thick films, that further proves a substrate-property dependent film growth. In the case of bare SiO_2 and HMDS treated SiO_2, the low-height flat islands, mentioned in the previous section, grow and coalesce, resulting in the low density and large area islands of Figure 3.6a and Figure 3.6c. Terraced structures have been identified by means of AFM profile analysis on both HMDS-treated and bare SiO_2. In the first case, step heights of the order of 1.2 nm have been recorded. These could be associated to single-monolayer steps, suggesting a nearly vertical orientation of the molecules (Figure 1.10) inside the molecular planes. Notice that large "canyons" [94] exist among the islands, indicating that further material is required for achieving the complete substrate coverage. The scenario is somehow similar to that reported in the literature for tetracene films deposited on SiO_2 and grown according to a "layer-by-layer" mode [94].

Figure 3.6b shows a 10 nm tetracene film grown over the OTS-treated SiO_2 surface. A stripe-region is observed at the center of the image where tetracene grows in a fashion more similar to the case of bare SiO_2. On the contrary, outside this region, the islands are smaller, higher and denser, following the trend encountered in the 2 and 5 nm AFM images in the case of OTS. A possible explanation for this phenomenon is the incomplete silanization of the SiO_2 substrate. Although this phenomenon was observed only once during the research project, it seemed interesting to report it here for illustrating the remarkable contrast in the morphological properties induced by the OTS-treatment. In all the other cases the morphology was found to be uniform and equal to that of the regions outside the presumably not silanized stripe.

Among the three polymeric substrates, PS (Figure 3.6e) gives the higher substrate surface coverage. At 10 nm of nominal thickness, it seems that a complete coverage has been obtained on the dielectric surface. Moreover, the islands appear homogeneous in their shapes and tightly packed to each other. On the other hand, 10 nm tetracene films on parylene C and PMMA,

shown in Figure 3.6d and Figure 3.6f respectively, do not yet achieve the complete substrate surface coverage. On PMMA, the islands are significantly smaller than in PS and parylene C. The marked color contrast between islands and substrate observable in the AFM image (Figure 3.6f) suggests that voids are still present between the tetracene particles.

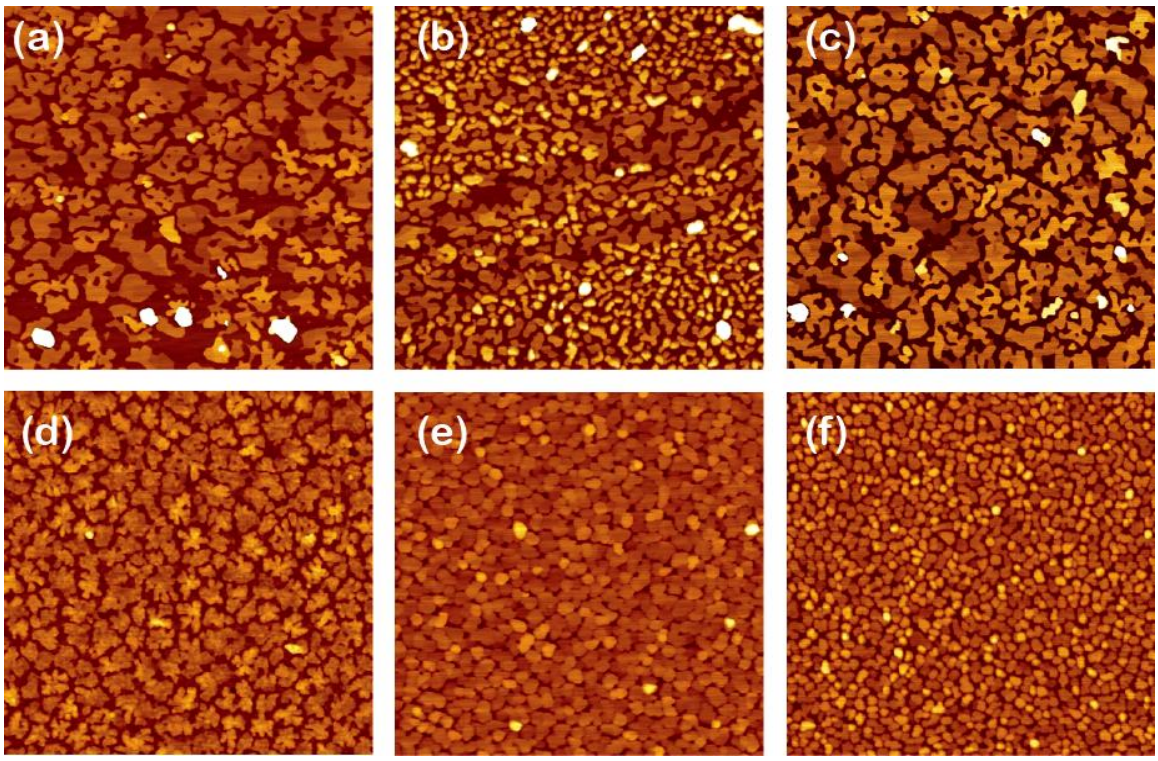

Figure 3.6 – 10 μm × 10 μm sized AFM images of tetracene thin films (nominal thickness 10 nm, deposition rate 3.5 Å/s) grown on different dielectric layers: (a) bare SiO_2; (b) OTS; (c) HMDS; (d) parylene C; (e) PS; (f) PMMA. Height scale: 0 - 50 nm.

In Figure 3.7 we report a set of Fluorescence Microscopy images relative to the 17 nm nominal thickness tetracene films. Notice that the optical band-gap of tetracene crystals is of the order of 2.3 eV [4], corresponding to a ~540 nm wavelength (green). The AFM images of the same samples are shown in the figure insets.

Adding material from 10 to 17 nm did not result in noticeable changes in the films' morphology. We observe a remarkable increase of substrate surface coverage in the case of OTS, PMMA and parylene C (complete coverage).

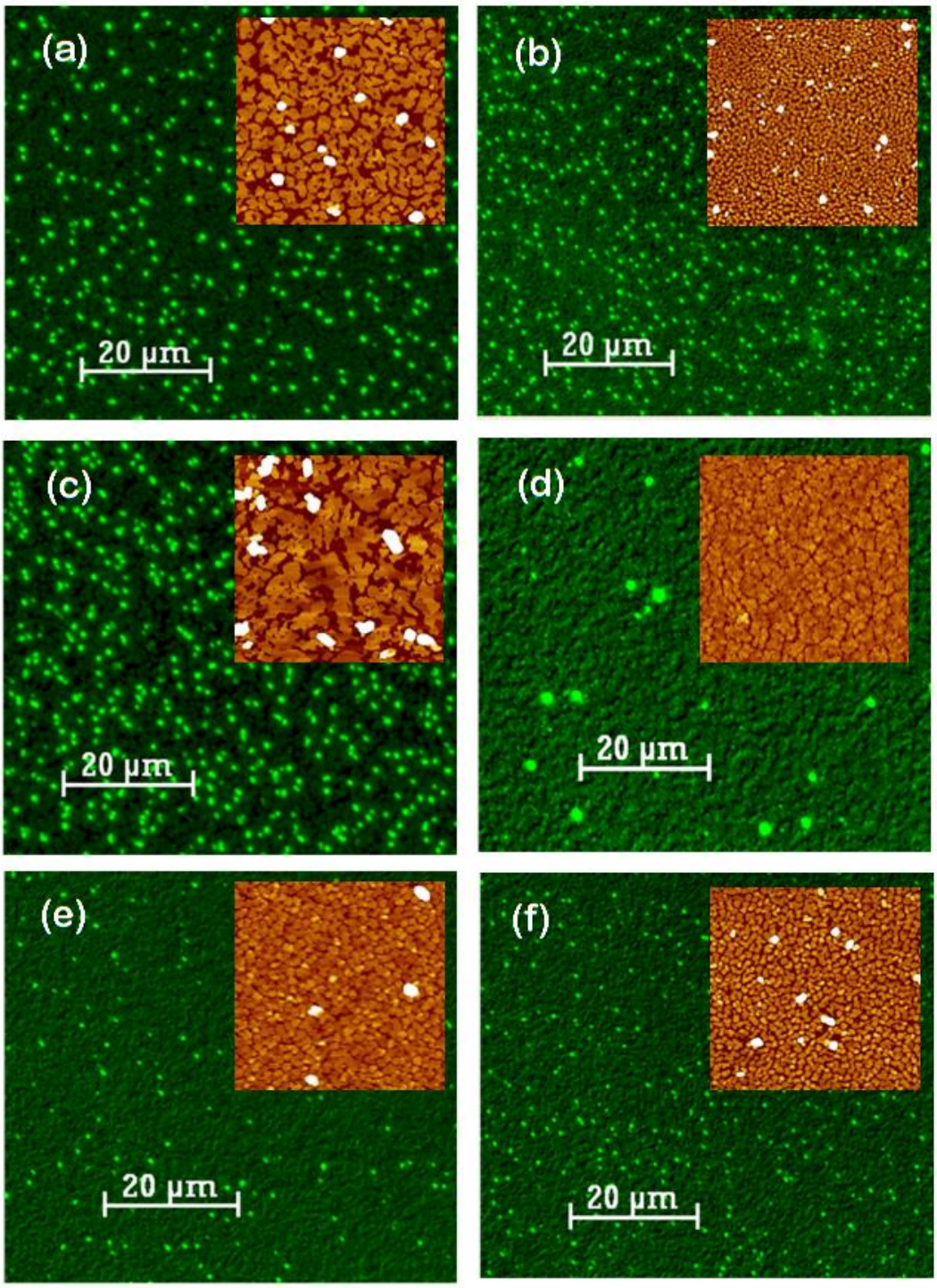

Figure 3.7 – Fluorescence images of tetracene films (nominal thickness 17 nm, deposition rate 3.5 Å/s) grown on different dielectric layers: (a) bare SiO_2; (b) OTS; (c) HMDS; (d) parylene C; (e) PS; (f) PMMA. The figure insets show 10 µm × 10 µm sized AFM images of the same films, height scale: 0 - 50 nm.

On HMDS-treated SiO_2 and bare SiO_2, the complete substrate surface coverage does not yet occur. The presence of exposed substrate areas is even indicated by the dark spots – with no green-light emission – visible in the Fluorescence images.

At both 10 and 17 nm, high three-dimensional particles, evident as clear spots in the AFM images and as bright green spots in the Fluorescence images, are found to coexist together with large flat islands. The green color of the light emitted by the particles and their highly geometrical shapes suggest that they are tetracene crystallites. Their origin is not yet well understood.

3.1.5 Complete coverage tetracene films

Hereafter we report the results of the AFM investigation conducted on complete coverage tetracene films deposited over different dielectric substrates, having nominal thicknesses of 35 nm (Figure 3.8 and Figure 3.9) and 50 nm (Figure 3.10).

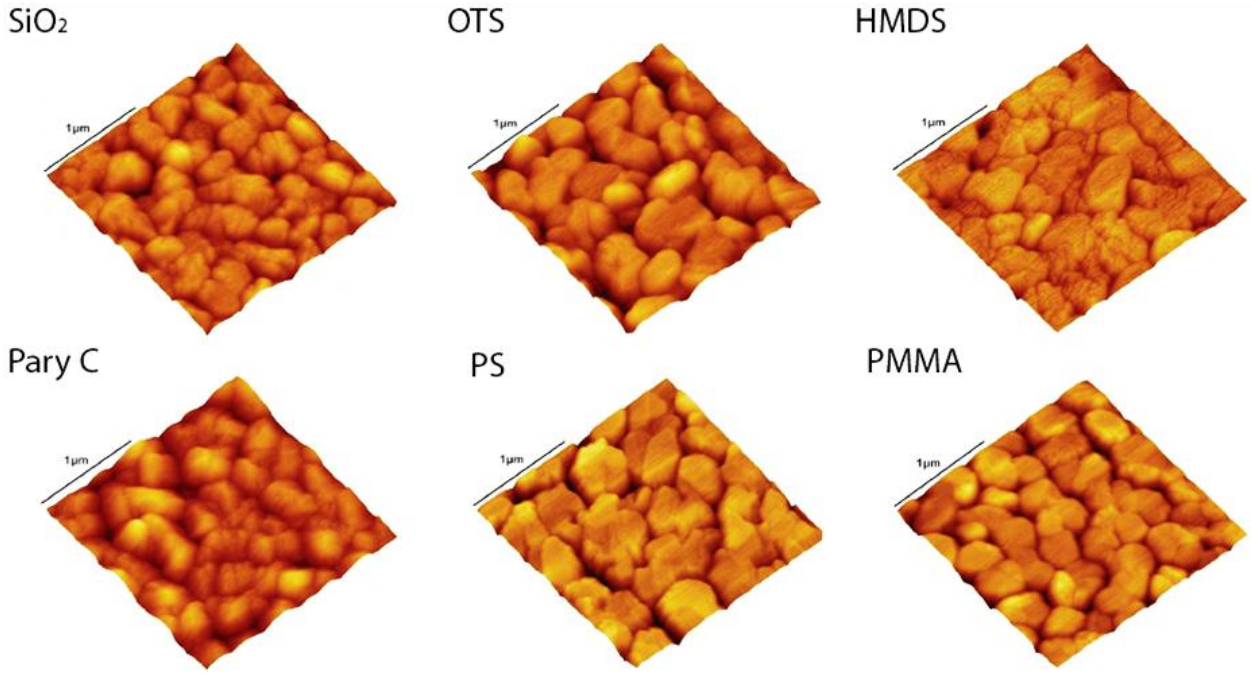

Figure 3.8 – AFM images of tetracene films with nominal thickness 35 nm, deposition rate 3.5 Å/s. Scale bars denote 1 µm.

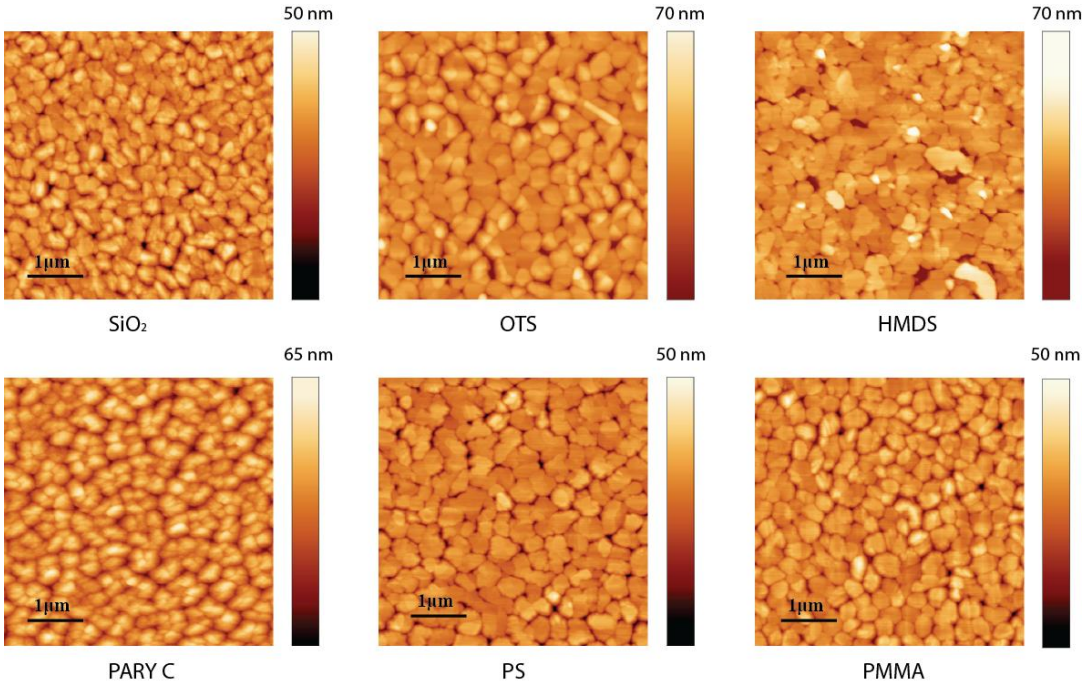

Figure 3.9 – 5 µm × 5 µm sized AFM images of tetracene films with nominal thickness 35 nm, deposition rate 3.5 Å/s, deposited on different dielectric substrates.

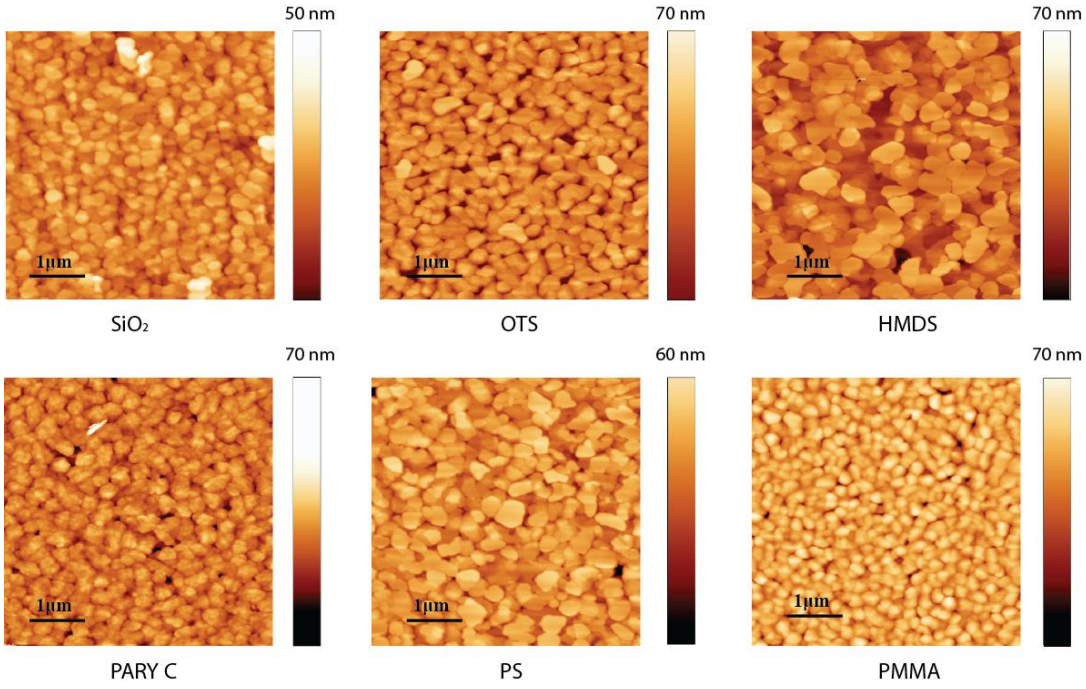

Figure 3.10 – 5 µm × 5 µm sized AFM images of tetracene films with nominal thickness 50 nm, deposition rate 3.5 Å/s, deposited on different dielectric substrates.

The AFM images of tetracene films reported in Figure 3.8 show granular morphologies with distinct features, specific to each dielectric. A straightforward method to estimate the average grain size in complete coverage films consists in extracting the correlation length ε (vide infra) from the Power Spectral Density (PSD) analysis [105]. The log-log PSD vs. spatial frequency plots obtained from the AFM images of Figure 3.9 are reported in Figure 3.11. They show two distinct regions: (i) a "plateau" at low spatial frequencies and (ii) a "decaying branch" at higher frequencies [106]. The reciprocal of the cut-off frequency is referred to as the correlation length, ε, and represents the "dominant lateral length scale" of the AFM image. In the case of granular-like morphologies, characterized by well connected grains, the correlation length provides an estimation of the average grain size.

The PSD analysis of the AFM images was conducted using the software WSxM v.5.0, which applies the Fast Fourier Transform (FFT) algorithm to calculate the discrete power spectrum of a topographic map $z(m,n)$, according to the following equation [107-108]:

$$\mathrm{PSD_{2D}}(\mathrm{k_x}, \mathrm{k_y}) = \mathrm{L^2}\left[\frac{1}{\mathrm{N^2}}\sum_{\mathrm{m=0}}^{\mathrm{N-1}}\sum_{\mathrm{n=0}}^{\mathrm{N-1}} \mathrm{z(m,n)e^{-2\pi i\frac{L}{N}(k_x m + k_y n)}}\right]^2 \qquad (3.1)$$

where L is the spatial length of an image row/column and N is the number of pixels of a single scan line. Notice that $\mathrm{PSD_{2D}}$ is a function of two spatial frequencies $\mathrm{k_x}$ and $\mathrm{k_y}$. However, due to the isotropy in the x-y plane of the granular-like morphology of tetracene films (no preferential direction exists in the x-y plane), it is possible to angle-integrate the $\mathrm{PSD_{2D}}$ without losing information. This permits to extract one-dimensional PSD plots as those presented in Figure 3.11, The correlation lengths, extracted from the PSD graphs of Figure 3.11, have been plotted in the histogram of Figure 3.12a to highlight the differences in average grain size occurring among the dielectric substrates. The error bars denote the maximum and minimum value obtained by measuring the correlation length of four distinct AFM images per each substrate.

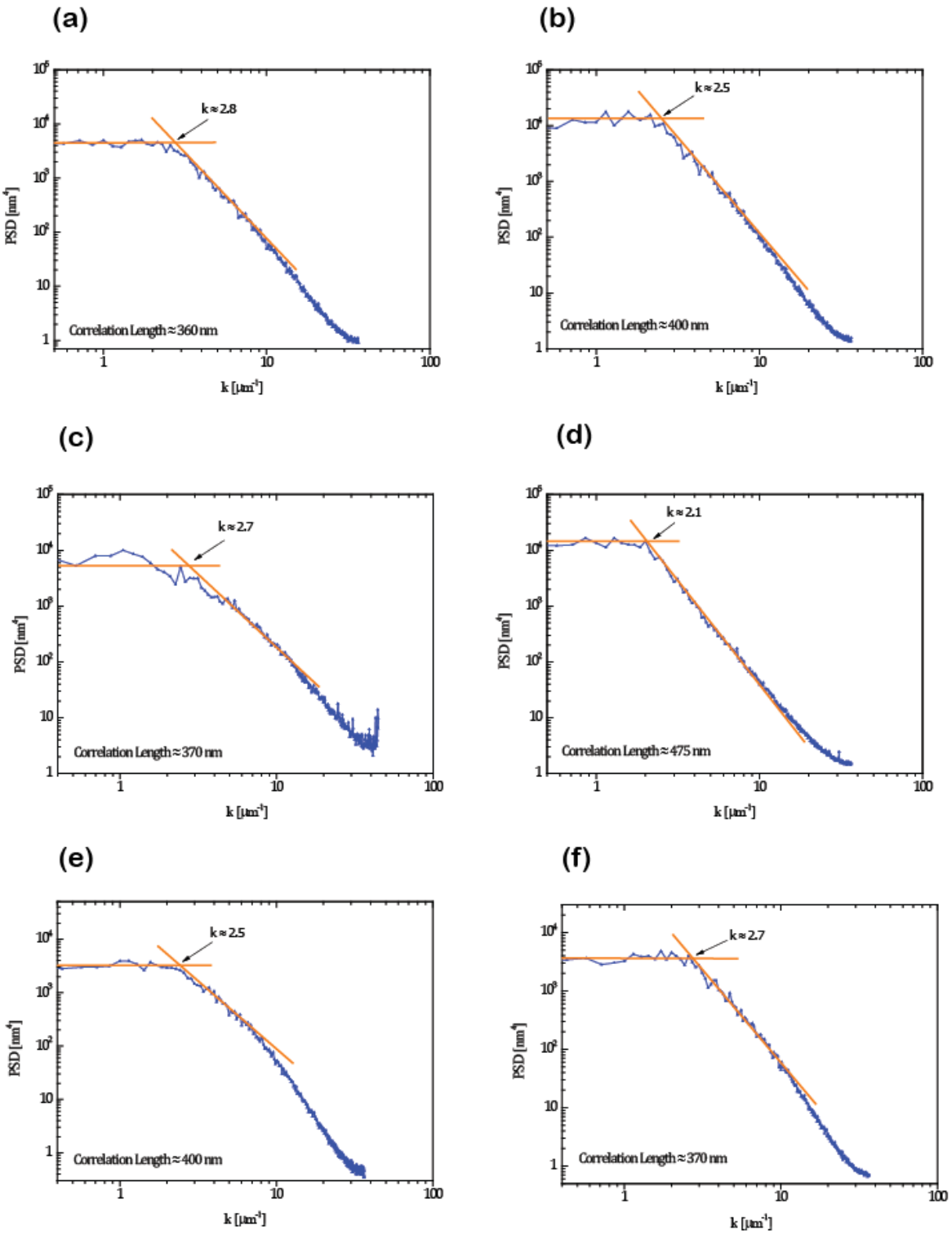

Figure 3.11 – PSD analysis of the AFM images presented in Figure 3.9. The intersection between the "plateau" and the exponential decay (logarithmic scale) represents the reciprocal of the correlation length ε.

The histogram does not reveal the presence of remarkable differences. Notice just that the use of dielectric substrates alternative to SiO_2 seems to improve the average grain size. In Figure 3.12b we plotted the RMS roughness from the same AFM images.

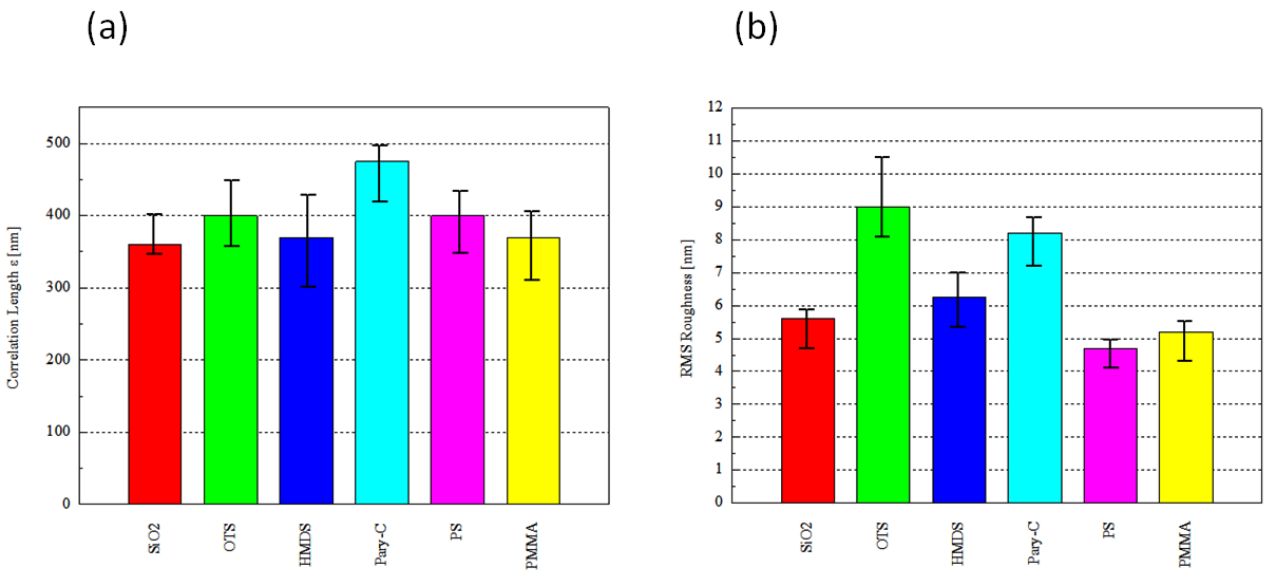

Figure 3.12 – Correlation Length ε (a) and RMS roughness (b) of the AFM images reported in Figure 3.9. The error bars denote the minimum a maximum value obtained in four distinct AFM images per each substrate.

Contributions to the RMS roughness of films with granular morphologies are given by the density of the grains as well as their size and connectivity.

The low RMS roughness of the films grown on PS suggests that tetracene grains (Figure 3.9) are smooth and well interconnected, consistently with the observations in Section 3.1.4.

Moreover, the RMS roughness plays a key role in determining the quality of the metal top contact-organic interface. Smooth organic films leads to good quality metal-organic interfaces, but not necessarily to the lowest contact resistance; indeed, as pointed out in [70], rough organic films favor the penetration of gold closer to the dielectric surface, thus reducing the "access resistance" to the channel.

PSD and roughness analysis have been conducted also on tetracene films with nominal thickness of 50 nm. The correlation length ε and the RMS roughness are plotted in the histograms of Figure 3.13a and Figure 3.13b respectively. The results appear considerably different from those obtained for the 35 nm films. As "new" material is added from 35 to 50 nm, for films deposited on OTS, HMDS and PS, a significant increase in RMS roughness is observable. Under these conditions, the meaning of the "correlation length" must be reviewed since it may be influenced by the presence of voids among the islands formed in the top layers of the organic films.

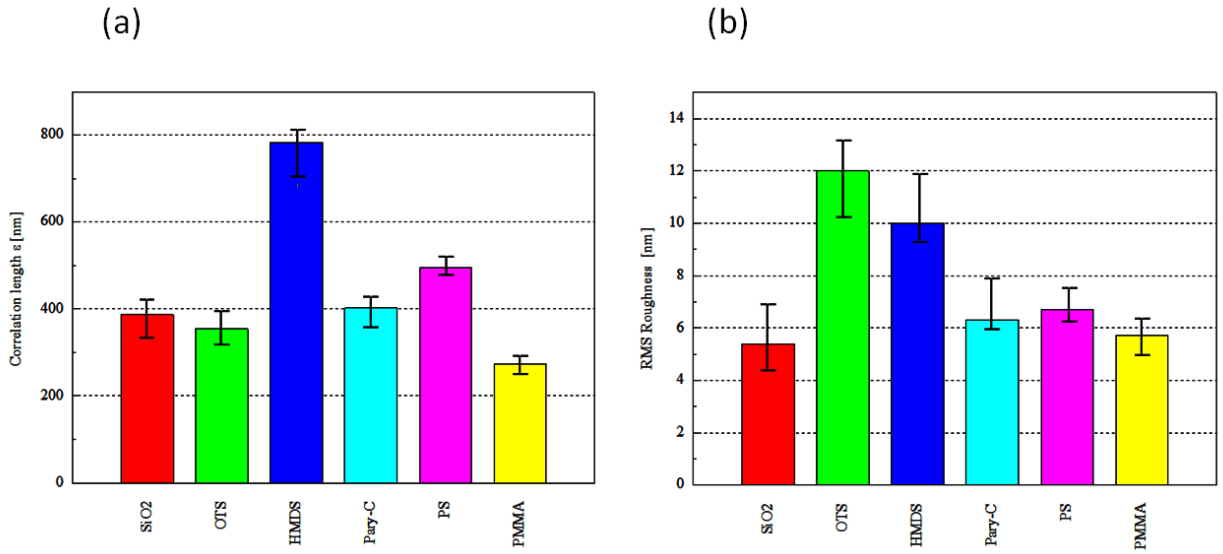

Figure 3.13 – Correlation Length ε (a) and RMS roughness (b) of the AFM images reported in Figure 3.10. The error bars denote the minimum a maximum value obtained in four distinct AFM images per each substrate.

3.2 Results on Tetracene-based OFETs

In this section we report the current-voltage characteristics of OFETs fabricated using the SAMs and polymers dielectrics. Different transistor channel geometries (single channel and interdigitated channels) have been explored, whose lengths L and widths W are indicated in Figure 2.19. We obtained working FET over all the dielectric substrates with different values of FET mobility and threshold voltage (V_{th}). These parameters were extracted from the saturation transfer characteristics, as described in Section 1.3, at a drain-source voltage equal to -60 V.

Measuring the FET mobility at saturation is a common approach in organic electronics since it avoids non idealities (observable in the linear region) associated with charge carrier injection barriers.

In the following pages we present the output (Figure 3.14) and transfer (Figure 3.15) characteristics of a set of OFET devices, having L = 100 μm and W = 4000 μm. The correspondent values of the FET mobility and V_{th} are reported inside the figures. All the OFETs present a I_{ON}/I_{OFF} ratio in the range of $10^5 \div 10^6$.

The output characteristics reveal bias stress effects (decrease in the drain-source current with increasing drain-source voltage) in the case of OTS (Figure 3.14b) and HMDS (Figure 3.14c). The stress effects are observable also in the transfer characteristics, identified by the presence of a significant V_{th} shift and by a large hysteresis, observed when the gate voltage is swept from 0 to -60 V (i.e. from the OFF to the ON state) and vice versa. These may be due to a not optimized SAM deposition process, e.g. due to chemical impurity in the reagents or to possible traces of solvent in the films [109].

In general, hysteresis can be caused by: (i) slow polarization of the dielectric layer and (ii) charge carrier trapping at the semiconductor/dielectric interface [110].

Phenomenon (i) occurs with polar dielectric materials (e.g. parylene C) or when dipoles are present on the dielectric surface (e.g. –OH groups). Here, the gate field induces a slow reorientation of the dipoles at the interface, which retards the accumulation of charge carriers during V_{GS} scan. The outcome is a hysteresis as in Figure 3.15d (parylene C), where the forward current is lower than the reverse current.

Phenomenon (ii) is associated with the presence of trap states in the transistor channel and causes an opposite loop direction, where the forward current is larger than the reverse current [110-111]. In the case of pentacene, a comprehensive explanation for hysteresis and loop direction is provided in reference [112]. This behavior is present – with more or less intensity – in the devices fabricated on all the dielectric substrates (except parylene C) employed in this project.

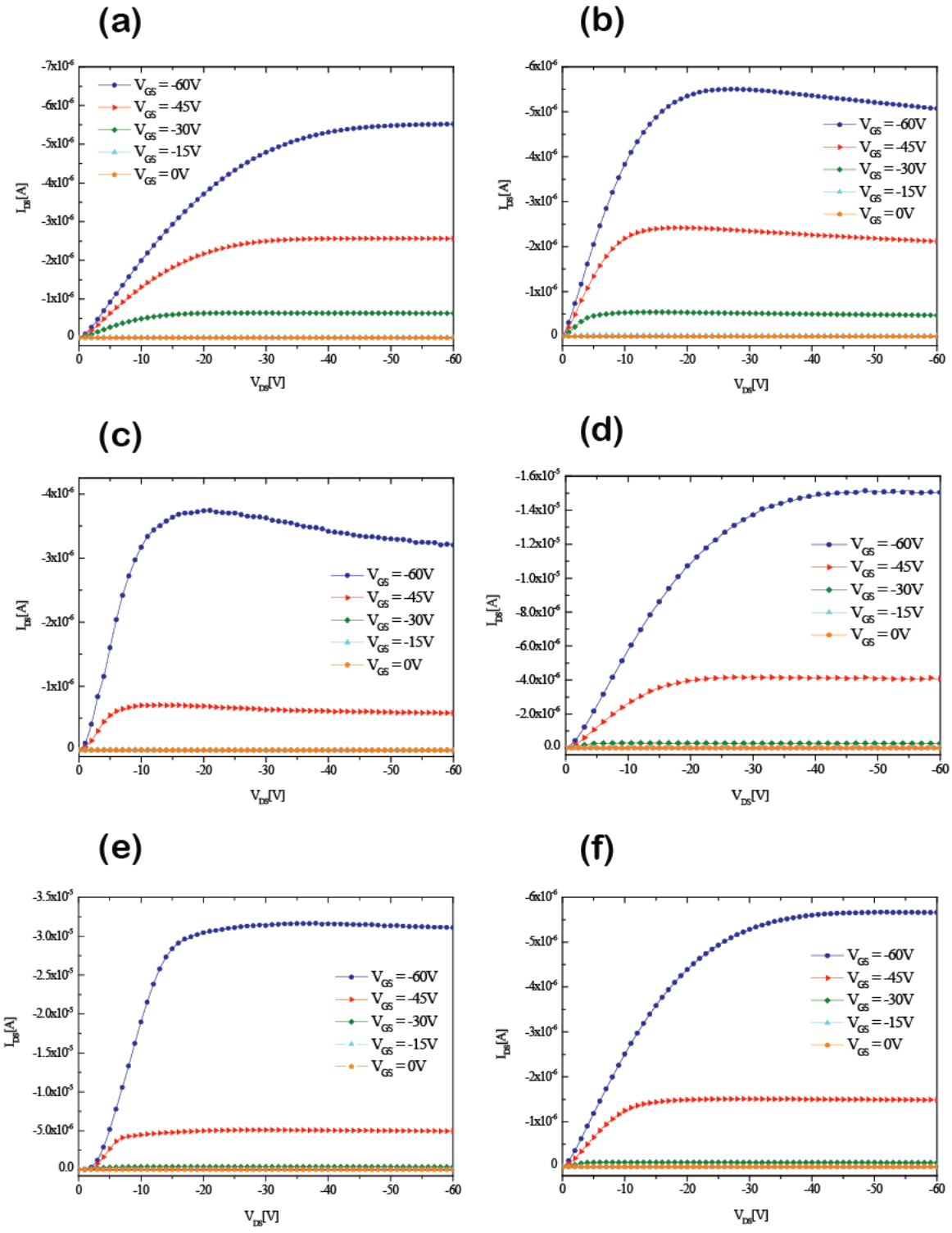

Figure 3.14 – Drain-source current (I_{DS}) vs. drain-source voltage (V_{DS}) output characteristics at different gate-source biases (V_{GS}), for tetracene OFETs employing different organic dielectric layers: (a) bare SiO_2; (b) OTS; (c) HMDS; (d) parylene C; (e) PS; (f) PMMA. All curves refer to single-channel devices, with channel length L=100 μm and channel width W = 4000 μm.

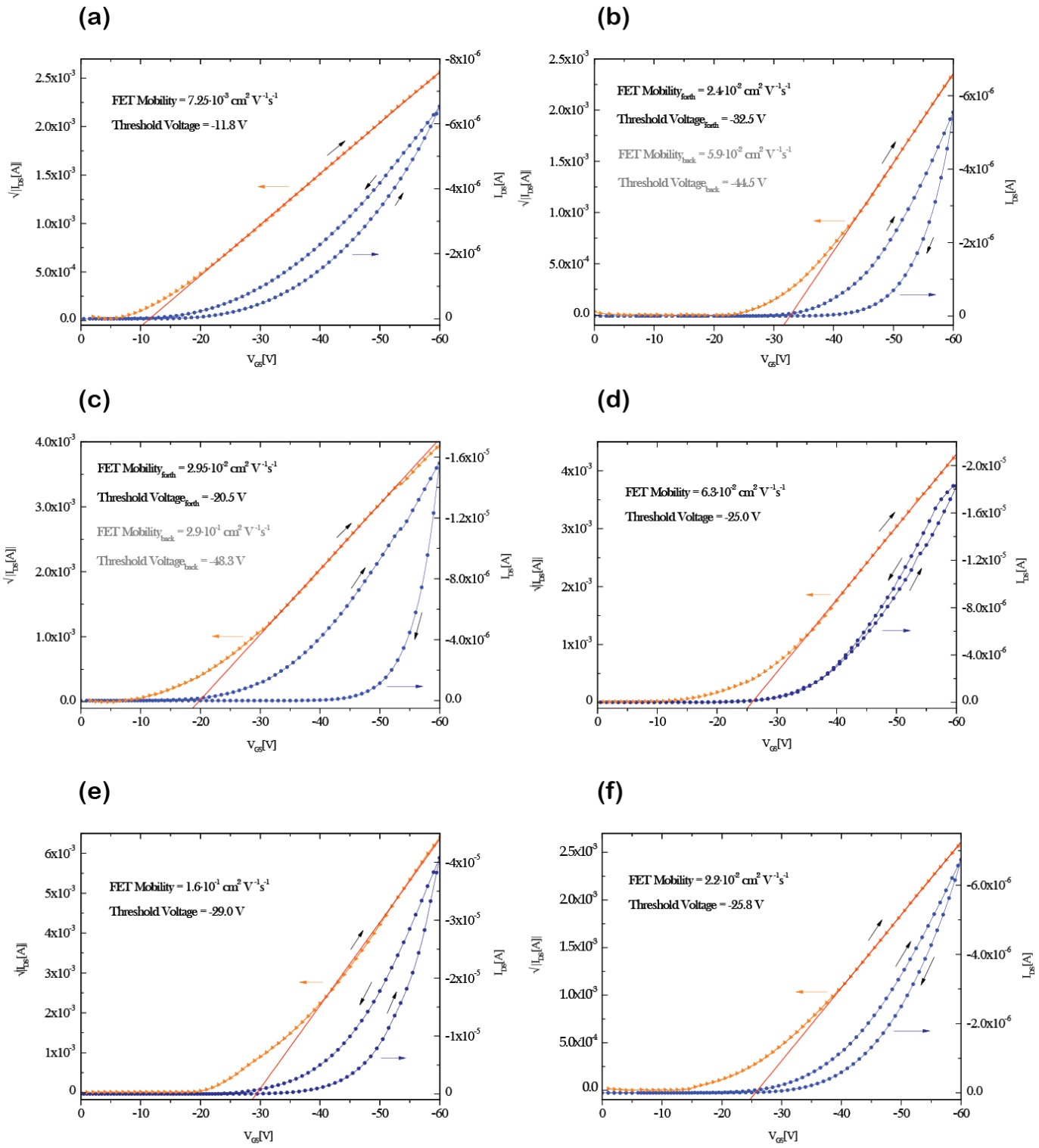

Figure 3.15 – I_{DS} vs. V_{GS} (blue) and $\sqrt{|I_{DS}|}$ vs. V_{GS} (orange) curves, with V_{DS} biased at -60 V, for tetracene OFETs (L = 100 µm and W = 4000 µm) employing different dielectric layers: (a) bare SiO_2; (b) OTS; (c) HMDS; (d) parylene C; (e) PS; (f) PMMA.

The highest hysteresis can be observed in Figure 3.15c (HMDS), for which the V_{th} and FET mobility were measured using the transfer curves in forward and reverse scans. In the "OFF to ON" direction we obtained a FET mobility and a threshold voltage equal to $2.95 \cdot 10^{-2}$ $cm^2V^{-1} \cdot s^{-1}$ and -20.5 V respectively. In the reverse scan, due to the large V_{th} shift (~28 V), it was possible to measure an "apparent" FET mobility as high as $2.9 \cdot 10^{-1}$ $cm^2V^{-1} \cdot s^{-1}$, i.e. one order of magnitude higher. This indicates the need for higher quality (e.g. in terms of chemical purity) HMDS monolayers.

For each dielectric, we measured at least 20 devices. In Figure 3.16 we report the average FET mobilities (horizontal lines) and the FET mobility values (scatter points) of different "working" OFETs, i.e. characterized by fair saturation of the output curves and proper scaling of the drain-source current with the W/L ratio, according to the equations presented in Section 1.3. The rate of success, by which we mean the number of "working" devices over the total number of measured devices, was between 60% and 80%, depending on the type of substrate.

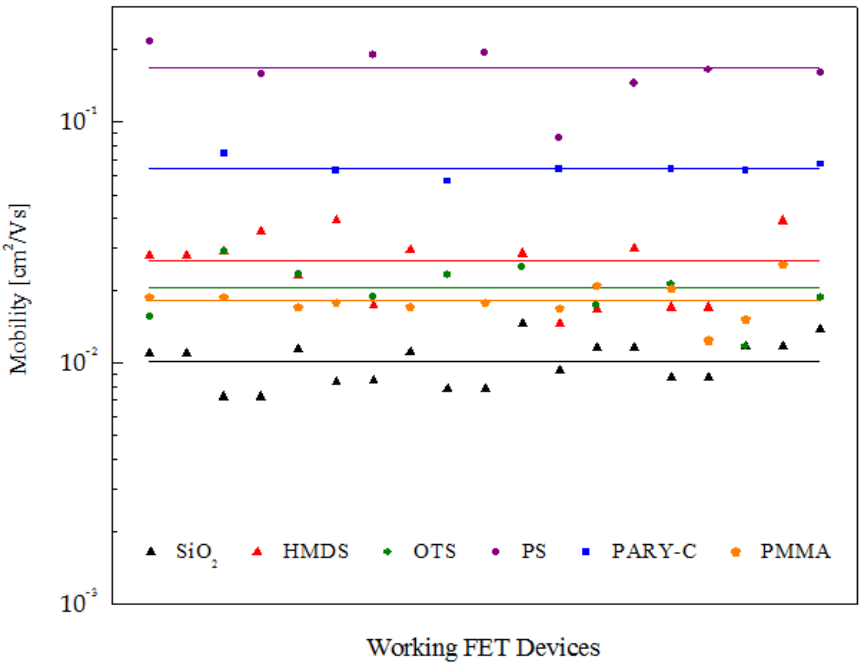

Figure 3.16 – FET mobility extracted from the transfer curves at saturation of tetracene OFETs. For each type of dielectric layer, different single-channel devices were tested, with L of 60, 80, 100, 150 µm and W of 2 and 4 mm.

The use of different channels lengths (60, 80, 100, 150 µm), allowed us to apply the Transfer Line Method (TLM) to estimate the contact resistance R_C. In top contact OFETs, contributions to the contact resistance are given by the metal-organic interface resistance R_{inj} and by the bulk resistance R_{bulk} experienced by the charge carriers moving from the electrode to the transistor channel [86]. Methods to extract the total contact resistance $R_c = R_{inj} + R_{bulk}$ have been extensively reviewed by Horowitz [113]. In Figure 3.17 we show the plot of the device resistance (normalized to W for comparison with the literature [87]) vs. L at two different gate voltages. The device resistance was evaluated as the reciprocal of the slope of the output curves at small source-drain voltages. The y-axis intercept of the linear extrapolation represents the total contact resistance R_c, whose values at $V_{GS} = -60$ V and $V_{GS} = -45$ V are reported in Table 3.4. In the table we indicate also the standard errors and the R^2 values resulting from the fitting procedure. Notice that the high relative error on the y-axis intercept arises from a lack of experimental points for small L due to limitations associated with shadow masks fabricated through laser ablation (Section 2.5). The contact resistance was found to be ca $3 \cdot 10^5$ Ω·cm at V_{GS} = -60 V, about one order of magnitude higher than for gold top contacts on pentacene [87]).

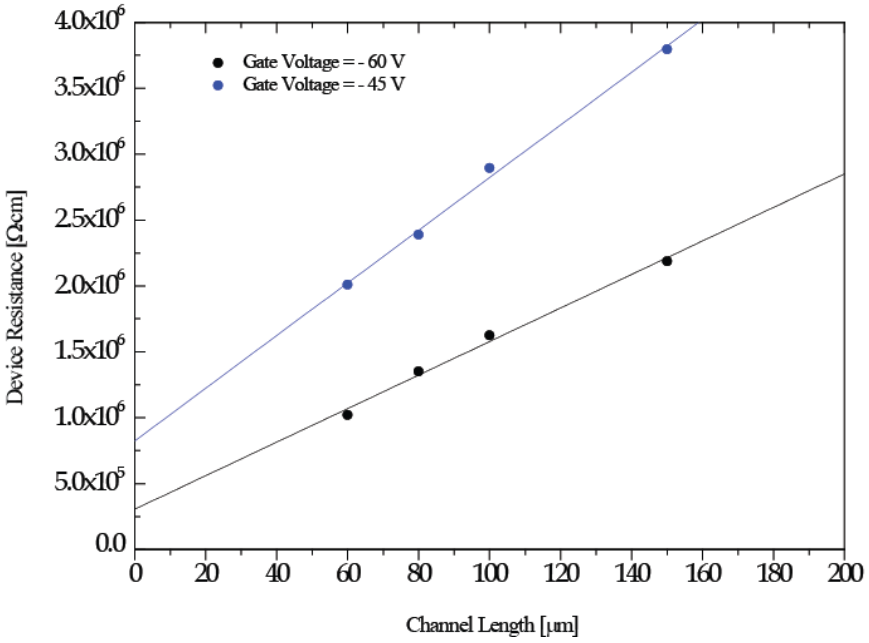

Figure 3.17 – Transmission Line Plot ($R_{TOT} \cdot W$ vs. L) at V_{GS} = -60 V (black) and V_{GS} = -45 V (blue) for top-contact tetracene OFETs employing PMMA as organic dielectric layer. The y-axis intercept represents the device contact resistance [87].

Gate Voltage	Contact Resistance [Ω·cm] (y-intercept)	Standard Error [Ω·cm]	Error %	R^2
-60 V	304889.20	84477.85	27.7	0.9877
-45 V	823349.35	93825.95	11.40	0.9938

Table 3.4 – Results of the linear extrapolation in Figure 3.17 (see text).

Figure 3.18 shows the average V_{th}, obtained from the transfer characteristics (in the forward direction) of the devices whose mobility is reported in Figure 3.16. The error bars represent the maximum and minimum V_{th}. The error on V_{th} for OTS and HMDS is due to the poor reproducibility of the measurements (bias stress effects). Both the capacitance of the dielectric layer and the density of trap states at the semiconductor/dielectric interface contribute to determine the V_{th} value. Compared to the SiO_2 case, the use of the polymeric dielectric layers increases V_{th} as a consequence of the reduction of the total dielectric capacitance [27]; higher V_{th} in OFETs with OTS and HMDS presumably stems from higher densities of electronic trap states at the dielectric/semiconductor interface.

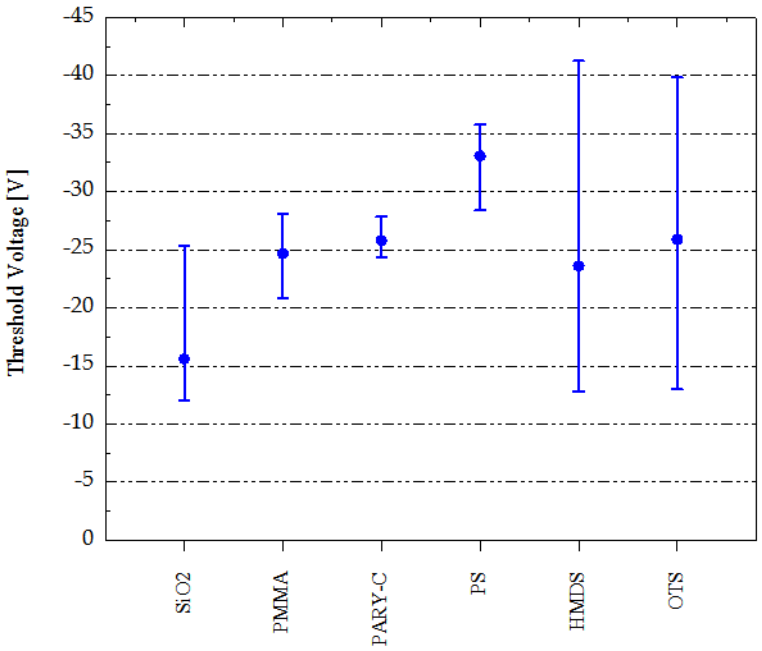

Figure 3.18 – V_{th} extracted from the saturated transfer characteristics of tetracene-based OFETs discussed in Figure 3.16 employing different dielectric layers. The error bars denote the minimum a maximum V_{th} value obtained for each dielectric.

Notice that, since the thickness of the PS and PMMA dielectric are similar (Table 2.1), the different device operational voltages can be related to the dielectric constants of the two polymers ($\varepsilon_{r,PS} = 2.6$ and $\varepsilon_{r,PMMA} = 3.5$).

Figure 3.19 shows the average values of FET mobility, with the corresponding error bars, obtained in OFETs employing different dielectric layers.

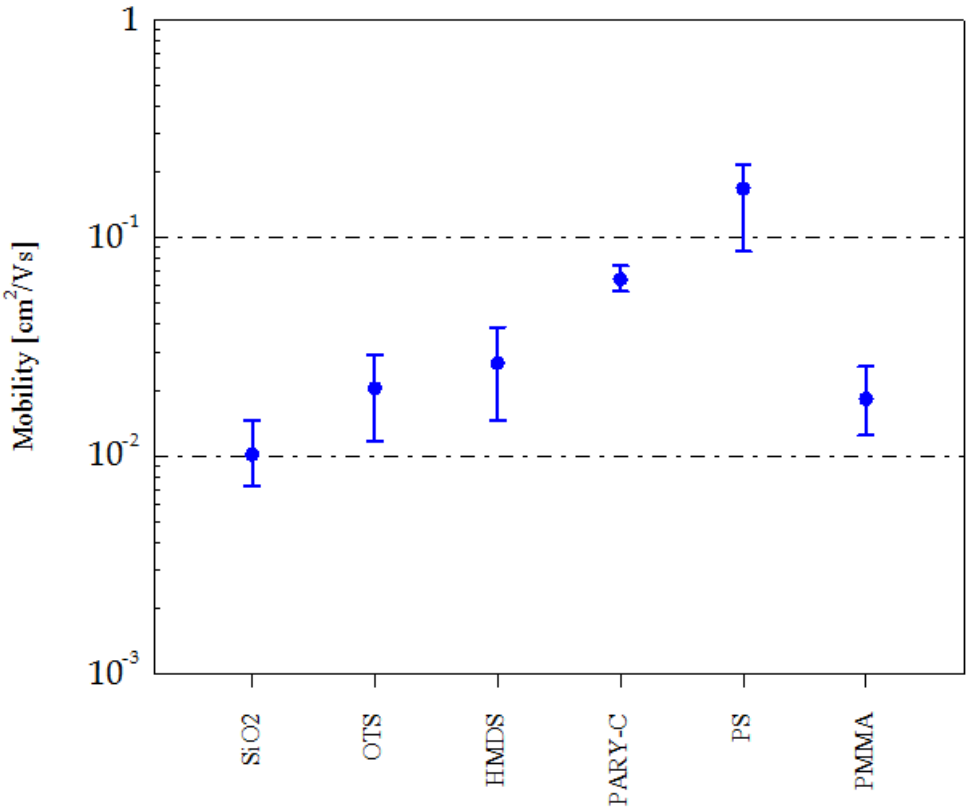

Figure 3.19 – FET extracted from the saturated transfer characteristics of tetracene-based OFETs employing different dielectrics. The error bars denote the minimum a maximum value obtained in the devices in Figure 3.16.

In previous publications [85] it was proved that the charge carrier mobility can be increased over two orders of magnitude (up to $4 \cdot 10^{-2}$ $cm^2V^{-1}s^{-1}$) by a proper choice of the deposition rate. Here we show that a FET mobility as high as $2 \cdot 10^{-1}$ $cm^2V^{-1}s^{-1}$ can be achieved by a careful choice of the dielectric substrate. The improvement we obtained over the SiO_2 gate dielectric by the use of a PS dielectric layer is higher than one order of magnitude. Notice that the performance of tetracene deposited on SiO_2 may depend considerably on the pressure and on the contamination

inside the evaporation chamber during the deposition. The system adopted in this research project had a base pressure of about 2.5×10^{-6} Torr and it is currently utilized for the evaporation of both metals (Al, Au) and organic molecules (pentacene and tetracene). Better results are expected using higher vacuum (e.g. as in reference [31, 94]) and a better control over contaminants.

The use of SAMs allows for a moderate increase of the device performance compared to SiO_2. However, we expect that higher FET mobilities can be obtained by optimizing the SAMs deposition process. A near-future objective is the realization of bias-stress free tetracene OFETs based on HMDS and OTS/SiO_2 gate dielectrics. The use of the three dielectric polymers leads to an increase of FET mobility. The improvement is remarkable in the case of PS and parylene C, but it appears modest in the case of PMMA.

It is worth noting that both the FET mobility and the V_{th} values in OFETs with a parylene C dielectric layer are characterized by the smallest error. This could be ascribed to the solvent-free processing of the dielectric layer (deposited from vapor phase) that limits chemical contamination and trap states at the interface.

Hereafter we want to briefly discuss the role of the different factors that may affect the extraction of charge carrier mobility and threshold voltage in an OFET device. When using laser ablated metal shadow masks, the value of the effective channel length may be different from the nominal value of the shadow mask layout. The deviation of the real channel length from the nominal one stems from both the limited geometrical precision of the shadow mask pattern and the possibility of a significant diffusion of the thermally evaporated gold far from the source and drain electrodes edges. We considered these two aspects by measuring the effective channel length from optical microscopy photographs and by investigating the morphology of the gold-tetracene step by means of AFM. Another factor that should be considered is the variability in the gate dielectric capacitance, which is due to the porosity of the dielectric material and to the deviation of the real dielectric layer thickness (oxide and polymer layer) from its reference value. However, the variability of the gate dielectric capacitance was estimated to induce an error in the FET mobility smaller than 5% and therefore considerably smaller than the error bars reported in Figure 3.19. The largest source of error is instead related to the bias-stress effects and to the strong dependence of the drain-source current from the history of the device. To minimize the variability we adopted the following strategy: for each device we first acquired a saturated

transfer characteristic in the forward direction of the gate-source voltage scan, from which the FET mobility was extracted; to minimize the bias stress effect we measured the current-voltage characteristic with a resolution of 0.5 V.

Notice that the charge carrier mobility depends on the gate voltage and the $\sqrt{|I_{DS}|}$ vs. V_{GS} curve at large V_{DS}, may not be linear; as a consequence there exists an uncertainty in the choice of the range to be used for the linear extrapolation with a consequent ambiguity in the determination of both threshold voltage and FET mobility. For different devices we evaluated the error in mobility and threshold voltage by considering the possible linear extrapolations of the $\sqrt{|I_{DS}|}$ vs. V_{GS} curve with the highest and the lowest slope. This allowed us to estimate a 15-20% variation in mobility and up to 30% in the threshold voltage.

3.3 Charge Carrier Transport in Tetracene OFETs - Discussion

Different aspects contribute to determine the efficiency of the charge carrier transport in tetracene OFETs, among which: (i) the properties of the dielectric layer, such as RMS roughness, dielectric constant, and surface chemistry; (ii) the structural and morphological properties of the tetracene films at the semiconductor/dielectric interface.

As we already mentioned, the dielectric substrate surface properties affect the transistor behavior. For example a high RMS roughness is detrimental to charge transport, since it limits the diffusion of the molecules on the surface thus preventing the formation of large islands with non-detrimental grain boundaries. On the other hand, in the context of this work, the RMS roughness was not found to be a dominant factor, being somehow limited and similar among the different dielectric layers employed (with the only exception of parylene C).

The dielectric permittivity plays a critical role. In general, it has been observed that the lower the dielectric permittivity, the higher the mobility [114]. Even though dielectrics with large permittivity are preferable for the decrease of the operational voltages, they also favor the charge carrier localization, due to strong local polarization effects [114]. We report in Figure 3.20 our results for the dependence of the charge carrier mobility on the dielectric constant ε_r, which seem to support this hypothesis.

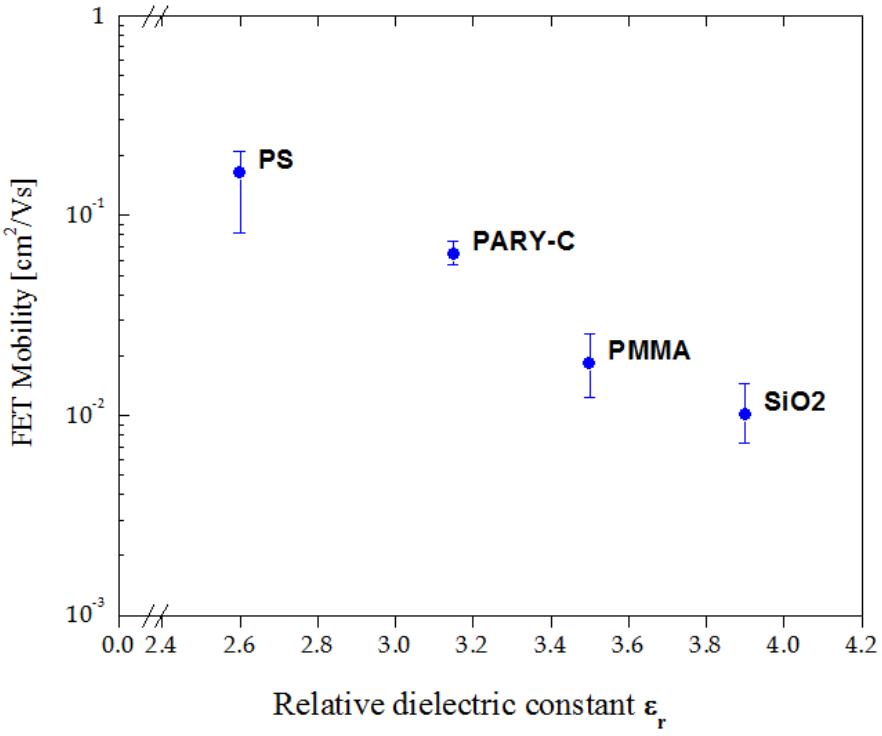

Figure 3.20 – FET Mobility vs. relative dielectric constant for tetracene OFETs fabricated on different dielectric layers.

Another aspect that directly affects the charge carrier transport is the dielectric surface chemistry, which can be related to the presence of electronic trap states. One example in literature is the electron trapping attributed to the silanol groups at SiO_2 surface [21], considered to be responsible for n-type transport suppression in OS. Contaminants, such as traces of solvents from the solution deposition of the dielectrics, can also cause charge carrier trapping.

The properties of the dielectric layer affect charge carrier transport by influencing the morphological and structural properties of the tetracene films at the interface. Here we consider the effects of film morphology, postponing the results on the film structure to the forthcoming analysis of the GIXRD data.

In Figure 3.21 we show the dependence of the FET mobility on the correlation length, ε, (see Section 3.1.5) for 50 nm thick tetracene films employed as active materials in OFETs.

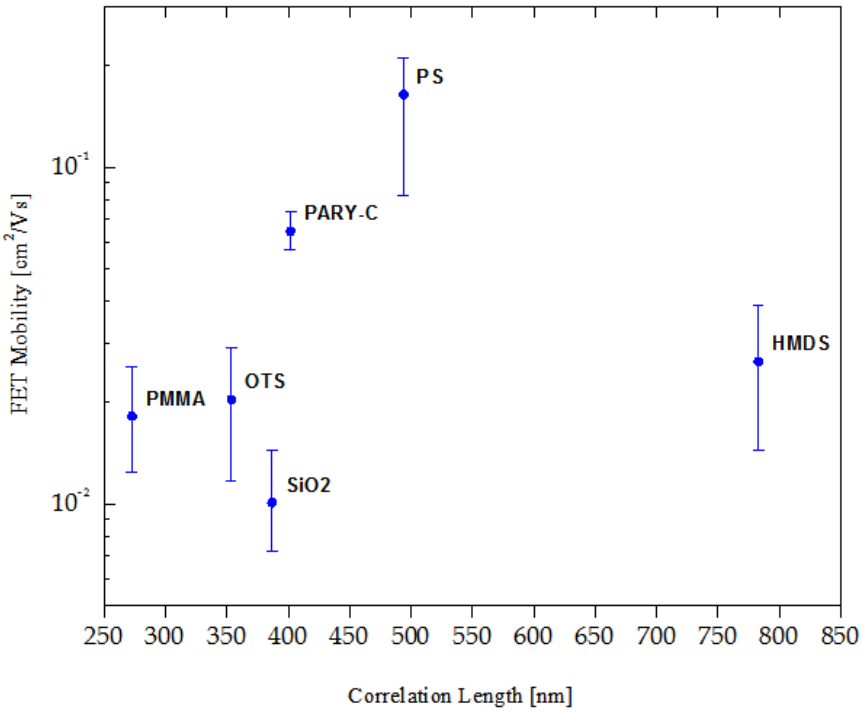

Figure 3.21 – FET Mobility vs. Correlation Length, ε, plot for tetracene thin films with nominal thickness of 50 nm. The error bars for ε are reported in the histogram of Figure 3.13a.

The treatment of SiO_2 with HMDS and OTS leads to a moderate increase of FET mobility. The study of the nucleation and growth process revealed that OTS favors the interfacial nucleation: the overgrown sub-monolayer tetracene films are characterized by a high density of islands from the very beginning of growth, with high levels of substrate surface coverage (~44% at 5 nm of nominal thickness, Table 3.3), which can explain the moderate increase of FET mobility. Other aspects may play a significant role, such as the structure/orientation of the crystalline grains, which are expected to be more similar to their bulk-like form (due to the reduced influence of the molecule-substrate interactions).

Although the morphology of tetracene films deposited on HMDS treated SiO_2 (Section 3.1.5) looks favorable for charge transport, the mobility improvement is modest. Large and flat islands, grown into a "quasi layer-by-layer" mode (Section 3.1.3), are expected to produce non-detrimental grain boundaries during coalescence. At the same time, as suggested by the strong hysteresis in Figure 3.15c, a high density of interfacial trap states could be located at the dielectric/semiconductor interface, due to a lack in chemical purity of HMDS or to residual traces of solvents on the surface.

For the polymeric dielectrics, the interpretation of the results from the point of view of morphology seems to be straightforward. Looking at Figure 3.21, it appears that a correlation exists between the grain dimensions and the FET mobility: the performance of OFETs employing PMMA is remarkably lower than for PS and parylene C, due to its smaller average grain size.

It is well documented in the literature that an increase in crystalline grain size corresponds to an increase in FET mobility, since the larger the grains, the smaller the "number" of grain-boundaries encountered by the mobile carriers during their path along the transistor channel. This behavior has been studied by Horowitz et al. [115] in the case of vacuum deposited semiconducting thiophenes. The authors explain that the charge transport is significantly affected by a "trapping and thermal release" process occurring at the localized electronic states located at the grain boundaries [115].

The good performance of OFETs using a parylene C gate dielectric, can be attributed both to the solvent-free processing of the dielectric layer and to the improved morphological properties of the overgrown tetracene films. As seen in Section 3.1, the tetracene islands in the early stages of growth are homogeneous in their shapes and cover uniformly the substrate surface. At the same time, the RMS roughness of the dielectric surface (~1.2 nm, Table 2.1) limits the achievement of higher FET mobilities.

In general, a clear effect of the dielectric surface roughness on the performance of the devices was not observed. Other factors play a more significant role, among which the presence of impurities coming from the use of solvents seems to be dominant.

As mentioned in Section 3.1.4, among the three polymeric substrates, PS leads to higher substrate surface coverage. This is proven by the formation of a complete monolayer at 10 nm of nominal thickness (Figure 3.6e), characterized by large, homogeneous and well connected islands. Moreover, the low RMS roughness of tetracene films on PS, suggests that the grains are smooth and well interconnected to each other. Thus, the interfacial layer, where the charge transport occurs, is characterized by a lower number of detrimental grain boundaries.

The low dielectric permittivity, the small dielectric layer RMS roughness (Table 2.1) and the improved tetracene morphology, all contribute to promote the efficiency of charge carrier transport in OFET devices based on a PS gate dielectric.

3.4 Electroluminescence from Tetracene Thin Films

The long-term objective of this work is to explore the possibility of an ambipolar transport in polycrystalline tetracene films, by the use of different dielectric substrates. This is interesting both from a fundamental point of view, for comparison with the present hypotheses on the general n-type behavior of OSs [21], and from a technological perspective, for the possibility to achieve high light-emission efficiency in tetracene based OLEFETs.

In the context of this research project, ambipolarity and electroluminescence in top-contact tetracene OFETs/OLEFETs were not observed, despite the different dielectric materials investigated. Several contributions might explain the observations. To illustrate these contributions we prefer to "disentangle" the ambipolarity issue from the lack of electroluminescence. The fact that we did not observe an ambipolar transport in our vacuum sublimed films could be ascribed to the presence of contaminants from the atmosphere collected during the processing of the organic dielectric layers as well as during their transfer to the glove box and characterization in the probe station. The high volatility of tetracene as well as the limited mechanical stability at high temperatures (higher than 100 °C [23]) of the organic dielectrics employed hinders the possibility to thermally treat the samples to eliminate such contaminants. On the other hand, in the hypothesis of the absence of contaminants at the interface organic film/dielectric interface, i.e. in case of efficient passivation of the dielectric substrate, the lack of ambipolarity could be due to the poor matching between the LUMO level of tetracene and the gold work function i.e. to the high barrier for the injection of electrons from the negatively biased drain electrode to the LUMO level of tetracene (Figure 1.11 [4]).

The lack of electroluminescence detection is even more delicate to explain.

The use of interdigitated electrodes, characterized by a large W/L ratio (e.g. W = 48.6 mm and L = 100 μm, Section 2.5) is a common strategy to amplify the electroluminescence signal, by increasing the drain-source current. In this way, the light emitted from the device can be visible at the naked eye and detectable by the use of a photodiode. However, despite the relatively large drain-source current recorded (hundreds of μA) no light emission was detected.

The better hypothesis we can formulate at present deals with the relatively high inter-electrode distance typical of transistors where top contact source and drain electrodes are patterned by shadow masking.

In fact, if we look at the literature, electroluminescence from unipolar OSs, has been achieved by the use of OLEFET architectures with relatively short transistor channel length. The first OLEFET, developed by Hepp et al. [14] employed a channel length of 5μm; Reynaert et al. [116], achieved electroluminescence from tetracene-based top contact OLEFETs (with Au as the source electrode material and Ca as the drain) by fabricating sub-micron channels.

However, with a short channel length, the transistor may not behave according to the standard equations presented in Section 1.3. In such transistors the holes pinch-off region (see Section 1.3) does not occur even at high drain-source voltages. The holes concentration profile decreases gradually from source to drain, but the pinch-off condition is not satisfied at any point along the transistor channel. This means that a non-negligible density of mobile holes exist in the proximity of the drain electrode. Electrons, injected from the drain electrode into the LUMO level of tetracene (possible injection mechanisms are explained in [14, 33]), can meet the holes located in proximity of the drain to form the excitons whose radiative recombination generate electroluminescence. The test of this hypothesis is in progress.

An optical image of the electroluminescence generated by an interdigitated bottom contact tetracene FET (L = 6 μm), is reported in Figure 3.22. Green electroluminescence is visible in close proximity to the electron injecting (drain) gold electrode. The image proves that the new set-up built ad hoc for the characterization of light emitting transistors works properly and thus does not limit their characterization.

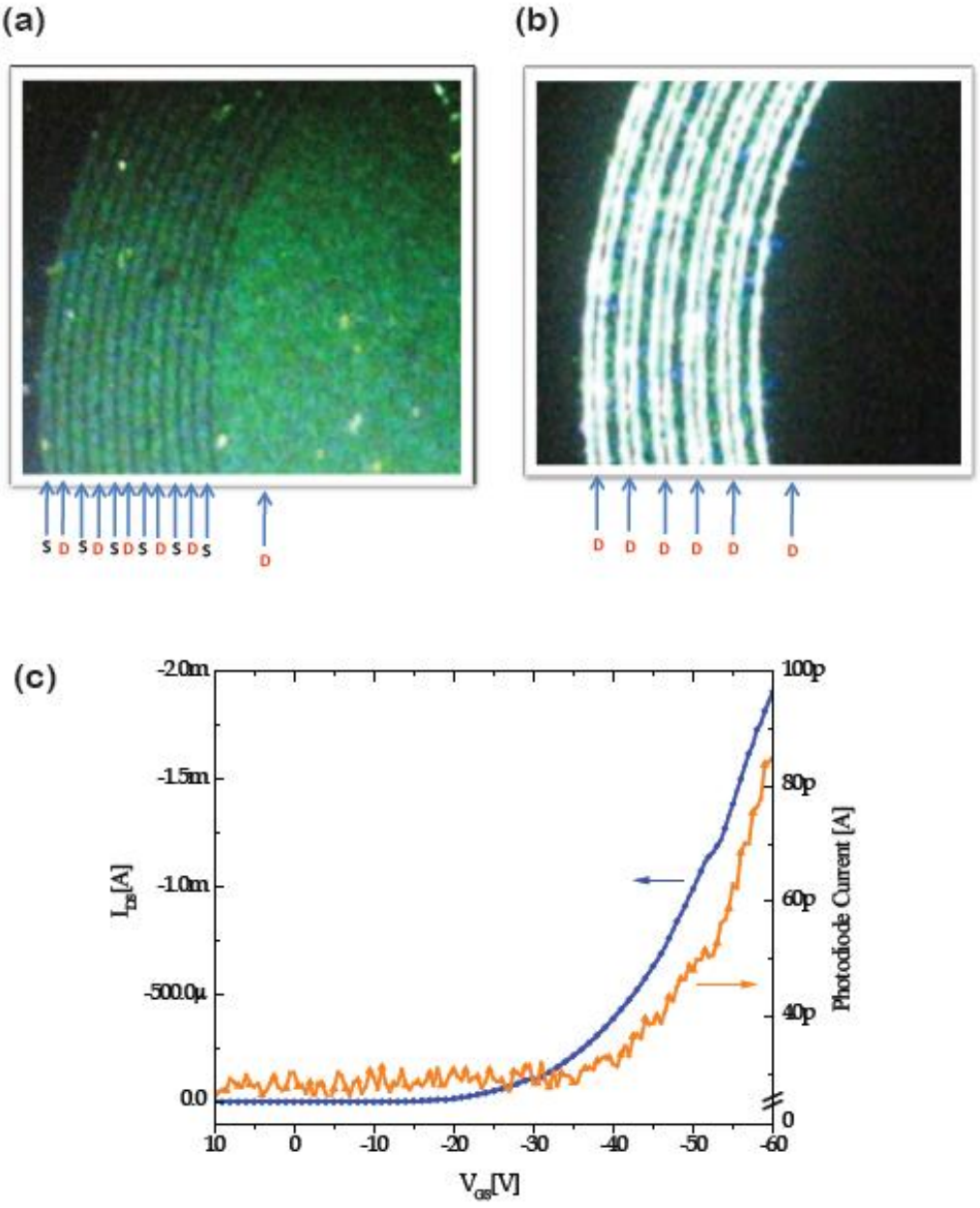

Figure 3.22 – (a) Optical image of the circular bottom contact interdigitated electrodes employed in light emitting tetracene FET investigated in this project; (b) optical image of the electroluminescence generated by tetracene films, under nitrogen atmosphere, showing the light emission region localized close to the negatively biased drain electrode; (c) I_{DS} vs. V_{GS} curves (blue) acquired simultaneously with the photodiode current (orange) caused by the light-emitted by the tetracene FET. W = 41000 µm and L = 6 µm.

Chapter 4. CONCLUSION AND PERSPECTIVES

In this work we investigated the role of organic dielectric layers in determining/influencing the properties of polycrystalline tetracene films for application in OFETs and OLEFETs.

The tetracene films were vacuum sublimed at 3.5 Å/s on six different dielectric substrates, namely bare SiO_2 (reference substrate), OTS treated SiO_2, HMDS treated SiO_2, parylene C on SiO_2, PS on SiO_2 and PMMA on SiO_2. The substrates were kept at room temperature and the pressure inside the vacuum chamber was of 2.5×10^{-6} Torr.

With these deposition conditions, we successfully fabricated tetracene-based p-type OFETs, employing all the aforementioned dielectric layers, and measured the respective hole FET mobility. OFETs were fabricated in the bottom gate – top contact geometry depositing the source and drain electrodes by thermal evaporation of gold through a metal shadow masks.

We observed that the hole mobility varies over more than one order of magnitude, depending on the dielectric substrates, ranging between $1\cdot10^{-2}$ $cm^2V^{-1}s^{-1}$ (bare SiO_2) and $2\cdot10^{-1}$ $cm^2V^{-1}s^{-1}$ (PS). To our best knowledge, the mobility value obtained on PS-based OFETs is the highest reported up to now for polycrystalline tetracene films. Better results are expected by the use of an evaporation system with a lower pressure inside the vacuum chamber (e.g. as in [31, 94]) and by further purification of the tetracene source material.

The interesting result is the remarkable variability of the hole mobility ascribed to different aspects of both the dielectric layers and the overgrown tetracene films.

The properties of the dielectric substrate surface influence the nucleation and growth process and consequently the final films' morphology and structure. Hence, the effect on film growth/morphology and charge transport had to be understood.

The nucleation and growth process was investigated from the early stages of growth up to complete substrate surface coverage by means of ex-situ AFM. The growth and the morphology of the tetracene films were found to depend significantly on the dielectric layer properties. Since the early stages of the growth, islands are formed with different densities, shapes and sizes. The dielectric substrate surface energy was observed to play a role in determining the islands density and shape. The dielectric substrate with the lowest surface energy, i.e. OTS treated SiO_2,

presented the highest density of highly three-dimensional islands. We observed that treating the SiO_2 surface with OTS promotes the interfacial nucleation thus leading to increased substrate surface coverage, compared to bare SiO_2. However, the highly three dimensional shape of the tetracene islands on OTS can induce the formation of detrimental grain boundaries during coalescence. The trade-off between these two aspects could explain the moderate increase in hole mobility associated with the OTS treatment of the SiO_2 surface.

On HMDS treated SiO_2, flat and large islands grow in a quasi "layer-by-layer" mode. This is expected to generate large and well interconnected crystalline grains at the dielectric/semiconductor interface, where the charge transport occurs. The FET mobility is moderately higher than in the case of bare SiO_2 and OTS treated SiO_2. However, severe bias stress effects limit the performance of the corresponding OFETs.

Tetracene thin films grown on PMMA show a hole FET mobility significantly lower compared to parylene C and PS. A Power Spectral Density analysis of the 50 nm thick tetracene films vacuum sublimed on the different dielectric substrates, revealed that the average size of tetracene grains on PMMA is significantly smaller than on the other polymer layers.

Tetracene films on PS show low RMS roughness and the earliest complete substrate surface coverage: at 10 nm of nominal thickness the islands appear homogeneous in their shapes and tightly packed to each other. Well interconnected and ordered grains in the early stages of the growth represent a possible reason for the high hole FET mobility of tetracene on PS.

The ongoing elaboration of the GIXRD data obtained from tetracene thin films deposited on the different substrates will shed light on the possible correlation between the charge transport and film structure.

The properties of the dielectric layer, such as the surface chemistry, the RMS roughness and the dielectric permittivity, directly affect the films' functional properties. An example was given in Section 3.3 when dealing with the role of the dielectric permittivity in influencing the FET mobility. Our results on tetracene films grown on polymeric dielectric substrates seem to confirm the model presented by Veres et al. in reference [114]: dielectric materials with high dielectric permittivity, although advantageous for the reduction of the operational voltages, result in lower FET mobilities. It should be noted that among the dielectric layers employed in this research project, PS had the lowest dielectric constant.

Another aspect that plays a role to determine the performance of OFETs, is the chemical purity of the dielectric surface. In fact, in the solution processed dielectric layers, residual traces of solvents or chemical contaminants, may affect the performance of the device by generating electronic trap states, as observed in the case of HMDS. In agreement with that, it was interesting to notice that the OFETs employing parylene C as a gate dielectric layer (deposited from the vapor phase) showed the smallest variability of threshold voltage and FET mobility.

Our experimental procedures did not lead to the observation of ambipolar transport. A more careful control of the organic dielectric processing (better control of the atmosphere) is believed to be necessary to reveal the transport of electrons within the tetracene transistor channel. Work is in progress to design a procedure for fabricating/characterizing tetracene-based OFETs and OLEFETs in inert atmosphere, without exposing the substrates to the ambient air after the deposition of the organic dielectric layer. This would allow reducing the adsorption of an oxygen/water layer at the dielectric/semiconductor interface that can be detrimental for the electron transport.

Electroluminescence was not detected in our top-contact tetracene OLEFETs. This result is probably related to the high inter-electrode distance typical of transistors where source and drain electrodes are patterned by shadow masking. Alternative strategies will be considered in the near future for higher resolution shadow masks, such as micro-photo-electroforming and silicon shadow masks, realized by means of side-to-side etching of thin silicon wafers.

A step that we want to take in the near future is the fabrication of “dual color electrodes”, i.e. source and drain contacts made with two distinct metals with the objective to better match HOMO and LUMO levels of tetracene with the electrodes’ work functions.

OTHER WORKS AND PROJECTS

Hereafter I describe other works and projects that I carried out at École Polytechnique de Montréal, in part as necessary steps for the completion of my M.Sc. project, in part as a contribution to the activity of my research group. The results of each work are available in the form of internal reports prepared for group meeting presentations.

1. AFM and Fluorescence Microscopy investigation of thin films of a new class of semiconducting small molecules [117]: dithienothiophene S-oxide and S,S-dioxide inner core oligomers (5SO, 5SO2, 7SO, 7SO2). The films were deposited by solution processing and thermal evaporation on differently treated SiO_2 substrates (HMDS and OTS). Tasks: (a) spin-coating, drop-cast and thermal evaporation (7SO2); (b) AFM measurements and Fluorescence imaging.

2. Electrical characterization of the OFETs based on the semiconducting films mentioned at point 1. Tasks: electrical measurements and extraction of the main device parameters (mobility, threshold voltage and on/off current ratio) from devices with different combinations of active material and dielectric layer. The experimental work was a contribution to a research project that resulted in the publication of the paper:

   Influence of the oxidation level on the electronic, morphological and charge transport properties of novel dithienothiophene S-oxide and S,S-dioxide inner core oligomers. **Journal of Materials Chemistry, 2010. 20(4): p. 669-676**.

3. Fabrication and electrical characterization of pentacene-based thin-film transistors with fluorine treated SiO_2 as dielectric layer. Tasks: (a) thermal evaporation of pentacene on pre-patterned bottom-contact FETs using both fluorine treated and bare SiO_2 as gate dielectrics; (b) electrical characterization of the devices; (c) analysis of the results in terms of mobility, threshold voltage and on/off current ratio.

4. Investigation of the properties of tetracene thin films vacuum sublimed on SiO_2 starting from tetracene powder purchased from three different companies: Kintec (China), Sigma Aldrich (USA) and Tokyo Chemical Industry (Japan). Tasks: (a) fabrication and electrical characterization of OFETs based on the three tetracene products; (b) AFM investigation of

the different tetracene films. The work became a proof of the low quality of tetracene commercialized by Kintec.

5. Calibration and optimization of the evaporator system for organic molecules and metals. Tasks: (a) cleaning and maintenance of the evaporator; (b) investigation on the optimal sample-source distance for tetracene, gold and aluminum; (c) thickness measurement of several Al and Au films (profilometry) to obtain the appropriate scaling factors for different positions of the quartz crystal microbalance with respect to the samples; (d) four-points probe measurements of the conductivity of Al and Au films.

6. AFM investigation of Carbon Nanotubes deposited on SiO_2 at different concentrations, used to promote the electron injection efficiency from bottom-contact electrodes in OFETs.

7. Investigation of the effects of different substrate cleaning procedures on the performance of organic transistors. Tasks: (a) cleaning the pre-patterned bottom-contact samples by means sonication in solvents (IPA/Acetone) followed by either O_2 plasma or UV/Ozone; (b) deposition of the active material; (c) electrical characterization of the devices and analysis of the results. The best performance was found with UV/Ozone cleaning method.

8. Fabrication of top-contact (TC) and bottom-contact (BC) devices based on different semiconducting polymers and small-molecules, namely P3HT (spin-coated), pentacene (vacuum sublimed), MEH-PPV and PCBM (spin-coated). The scope of the work was the comparison between the characteristics (e.g. FET mobility and contact resistance) of TC and BC devices. Tasks: (a) fabrication of TC OFETs based on the aforementioned organic semiconductors; (b) deposition of semiconducting thin films on pre-patterned BC substrates; (c) electrical measurements and extraction of FET mobility, threshold voltage and contact resistance. The latter was evaluated by both Transfer Line Method (TLM) and Single Curve Analysis (SCA).

9. In May 2010 I participated in a Synchrotron research activity at ELETTRA (Trieste, Italy) to investigate – by means of Grazing Incidence X-Ray Diffraction – the structure and texture of polycrystalline tetracene films grown on the dielectric surfaces presented in this text. (Results to be published in near-future papers).

REFERENCES

1. Heeger, A.J., *Semiconducting and metallic polymers: the fourth generation of polymeric materials.* Synthetic Metals, 2001. **125**(1): p. 23-42.

2. Chiang, C.K., et al., *Electrical Conductivity in Doped Polyacetylene.* Physical Review Letters, 1977. **39**(17): p. 1098.

3. Pochettino, A., Acad. Lincei Rend., 1906. **15**: p. 355.

4. Pope, M. and C.E. Swenberg, *Electronic processes in organic crystals*. Monographs on the physics and chemistry of materials, 39. 1982, Oxford; New York: Clarendon Press ; Oxford University Press.

5. Heilmeier, G.H. and L.A. Zanoni, *Surface studies of alpha-copper phthalocyanine films.* Journal of Physics and Chemistry of Solids, 1964. **25**(6): p. 603-611.

6. Tsumura, A., H. Koezuka, and T. Ando, *Macromolecular electronic device: Field-effect transistor with a polythiophene thin film.* Applied Physics Letters, 1986. **49**(18): p. 1210-1212.

7. Kymissis, I., *Organic field effect transistors: theory, fabrication and characterization*. 2009, New York, NY: Springer.

8. Facchetti, A., *Semiconductors for organic transistors.* Materials Today, 2007. **10**(3): p. 28-37.

9. Cicoira, F. and C. Santato, *Organic Light Emitting Field Effect Transistors: Advances and Perspectives.* Advanced Functional Materials, 2007. **17**(17): p. 3421-3434.

10. Zi, H., et al., *Design, Synthesis, and Transistor Performance of Organic Semiconductors*, in *Organic Field-Effect Transistors*. 2007, CRC Press.

11. Klauk, H., et al., *Ultralow-power organic complementary circuits.* Nature, 2007. **445**(7129): p. 745-748.

12. Chuang, T.-K., et al., *Polysilicon TFT technology on flexible metal foil for AMPLED displays.* Journal of the Society for Information Display, 2007. **15**: p. 455-461.

13. Malliaras, G. and R. Friend, *An Organic Electronics Primer.* Physics Today, 2005. **58**(5): p. 53-58.

14. Hepp, A., et al., *Light-emitting field-effect transistor based on a tetracene thin film.* Physical Review Letters, 2003. **91**(15).

15. Muccini, M., *A bright future for organic field-effect transistors.* Nature Materials, 2006. **5**(8): p. 605-613.

16. Capelli, R., et al., *Organic light-emitting transistors with an efficiency that outperforms the equivalent light-emitting diodes.* Nature Materials, 2010. **9**(6): p. 496-503.

17. Brütting, W., *Physics of organic semiconductors*. 2005, Weinheim: Wiley-VCH.

18. Zaumseil, J. and H. Sirringhaus, *Electron and Ambipolar Transport in Organic Field-Effect Transistors.* Chemical Reviews, 2007. **107**(4): p. 1296-1323.

19. Sirringhaus, H., *Organic semiconductors: An equal-opportunity conductor.* Nature Materials, 2003. **2**(10): p. 641-642.

20. Ando, S., et al., *Novel p- and n-type organic semiconductors with an anthracene unit.* Chemistry of Materials, 2005. **17**(6): p. 1261-+.

21. Chua, L.-L., et al., *General observation of n-type field-effect behaviour in organic semiconductors.* Nature, 2005. **434**(7030): p. 194-199.

22. Yoon, M.H., et al., *Gate dielectric chemical structure-organic field-effect transistor performance correlations for electron, hole, and ambipolar organic semiconductors.* Journal of the American Chemical Society, 2006. **128**(39): p. 12851-12869.

23. Aguirre, C.M., et al., *The Role of the Oxygen/Water Redox Couple in Suppressing Electron Conduction in Field-Effect Transistors.* Advanced Materials, 2009. **21**(30): p. 3087-+.

24. Dinelli, F., et al., *Spatially correlated charge transport in organic thin film transistors.* Physical Review Letters, 2004. **92**(11).

25. Gamota, D., *Printed organic and molecular electronics*. 2004, Boston: Kluwer Academic Publishers.

26. Sze, S.M. and K.K. Ng, *Physics of semiconductor devices*. 2007, New York: John Wiley & Sons.

27. Horowitz, G., et al., *The Concept of "Threshold Voltage" in Organic Field-Effect Transistors.* Advanced Materials, 1998. **10**(12): p. 923-927.

28. Zaumseil, J., R.H. Friend, and H. Sirringhaus, *Spatial control of the recombination zone in an ambipolar light-emitting organic transistor.* Nature Materials, 2006. **5**(1): p. 69-74.

29. Takahashi, T., et al., *Ambipolar light-emitting transistors of a tetracene single crystal.* Advanced Functional Materials, 2007. **17**(10): p. 1623-1628.

30. Reese, C., et al., *High-performance microscale single-crystal transistors by lithography on an elastomer dielectric.* Applied Physics Letters, 2006. **89**(20): p. 202108-3.

31. Gundlach, D.J., et al., *Thin-film transistors based on well-ordered thermally evaporated naphthacene films.* Applied Physics Letters, 2002. **80**(16): p. 2925-2927.

32. Tersigni, A., et al., *Structure of tetracene films on hydrogen-passivated Si(001) studied via STM, AFM, and NEXAFS.* Physical Review B (Condensed Matter and Materials Physics), 2006. **74**(20): p. 205326-1.

33. Santato, C., et al., *Tetracene-based organic light-emitting transistors: optoelectronic properties and electron injection mechanism.* Synthetic Metals, 2004. **146**(3): p. 329-334.

34. Locklin, J., et al., *Optimizing the Thin Film Morphology of Organic Field-Effect Transistors: The Influence of Molecular Structure and Vacuum Deposition Parameters on Device Performance.* Polymer Reviews, 2006. **46**(1): p. 79 - 101.

35. Joo Shin, T. and H. Yang, *Grazing Incidence X-Ray Diffraction (GIXD),* in *Organic Field-Effect Transistors*. 2007, CRC Press.

36. Braga, D. and G. Horowitz, *High-Performance Organic Field-Effect Transistors.* Advanced Materials, 2009. **21**(14-15): p. 1473-1486.

37. Tompkins, H.G., E.A. Irene, and Knovel. *Handbook of ellipsometry*. 2005.

38. Stracci, G., C. Palazzesi, and F. De Matteis, *Appunti di Ellissometria.*

39. Fujiwara, H., *Spectroscopic ellipsometry: principles and applications*. 2007, Chichester, England; Hoboken, NJ: John Wiley & Sons.

40. Wollam J.A., *2010, Ellipsometry Tutorial.* Extracted from http://www.jawoollam.com, on October 2, 2010.

41. Tompkins, H.G., *A user's guide to ellipsometry*. 1993, Boston: Academic Press.

42. Walsh, C.B. and E.I. Franses, *Thickness and quality of spin-coated polymer films by two-angle ellipsometry.* Thin Solid Films, 1999. **347**(1-2): p. 167-177.

43. Walsh, C.B. and E.I. Franses, *Ultrathin PMMA films spin-coated from toluene solutions.* Thin Solid Films, 2003. **429**(1-2): p. 71-76.

44. Alves, J.M., et al., *A differential mechanical profilometer for thickness measurement.* Review of Scientific Instruments, 2004. **75**(12): p. 5362-5363.

45. Binnig, G., C.F. Quate, and C. Gerber, *Atomic Force Microscope.* Physical Review Letters, 1986. **56**(9): p. 930.

46. Giessibl, F.J., *Advances in atomic force microscopy.* Reviews of Modern Physics, 2003. **75**(3): p. 949.

47. Blanchard, C.R., *Atomic Force Microscopy.* The Chemical Educator, 1996. **1**(5): p. 1-8.

48. Albrecht, T.R., et al., *Frequency-Modulation Detection using high-Q Cantilevers for Enhanced Force Microscopy Sensitivity* Journal of Applied Physics, 1991. **69**(2): p. 668-673.

49. Horcas, I., et al., *WSXM: A software for scanning probe microscopy and a tool for nanotechnology.* Review of Scientific Instruments, 2007. **78**(1): p. 013705-8.

50. Kwok, D.Y., et al., *Contact Angle Measurements and Contact Angle Interpretation. 1. Contact Angle Measurements by Axisymmetric Drop Shape Analysis and a Goniometer Sessile Drop Technique.* Langmuir, 1997. **13**(10): p. 2880-2894.

51. Tavana, H. and A.W. Neumann, *Recent progress in the determination of solid surface tensions from contact angles.* Advances in Colloid and Interface Science, 2007. **132**(1): p. 1-32.

52. Thiessen, D. and K. Man, *Surface Tension Measurement*, in *The Measurement, Instrumentation and Sensors Handbook on CD-ROM*. 1999, CRC Press.

53. Shafrin, E.G. and W.A. Zisman, *Critical surface tension for spreading on liquid substrate.* Journal of Physical Chemistry, 1967. **71**(5): p. 1309-1316.

54. Yun, Y., C. Pearson, and M.C. Petty, *Pentacene thin film transistors with a poly(methyl methacrylate) gate dielectric: Optimization of device performance.* Journal of Applied Physics, 2009. **105**(3): p. 034508-034508-7.

55. Puigdollers, J., et al., *Pentacene thin-film transistors on polymeric gate dielectric: device fabrication and electrical characterization.* Journal of Non-Crystalline Solids, 2004. **338-340**: p. 617-621.

56. Huang, T.-S., Y.-K. Su, and P.-C. Wang, *Study of organic thin film transistor with polymethylmethacrylate as a dielectric layer.* Applied Physics Letters, 2007. **91**(9): p. 092116.

57. Fortin, J.B. and T.M. Lu, *Chemical vapor deposition polymerization : the growth and properties of parylene thin films*. 2004, Boston: Kluwer Academic Publishers.

58. Klauk, H. and T.N. Jackson, *Pentacene organic thin-film transistors and ICs.* Solid State Technology, 2000. **43**(3): p. 63-+.

59. Shankar, K. and T.N. Jackson, *Morphology and electrical transport in pentacene films on silylated oxide surfaces.* Journal of Materials Research, 2004. **19**(7): p. 2003-2007.

60. Salleo, A., et al., *Polymer thin-film transistors with chemically modified dielectric interfaces.* Applied Physics Letters, 2002. **81**(23): p. 4383-4385.

61. Sirringhaus, H., N. Tessler, and R.H. Friend, *Integrated Optoelectronic Devices Based on Conjugated Polymers.* Science, 1998. **280**(5370): p. 1741-1744.

62. Sandberg, H.G.O., et al., *Ultrathin Regioregular Poly(3-hexyl thiophene) Field-Effect Transistors.* Langmuir, 2002. **18**(26): p. 10176-10182.

63. Yang, H., et al., *Conducting AFM and 2D GIXD Studies on Pentacene Thin Films.* Journal of the American Chemical Society, 2005. **127**(33): p. 11542-11543.

64. Killampalli, A.S. and J.R. Engstrom, *Nucleation of pentacene thin films on silicon dioxide modified with hexamethyldisilazane.* Applied Physics Letters, 2006. **88**(14): p. 143125-143125-3.

65. Muller-Buschbaum, P., *Influence of surface cleaning on dewetting of thin polystyrene films.* European Physical Journal E, 2003. **12**(3): p. 443-448.

66. Stange, T.G., et al., *Scanning tunneling microscopy and atomic force microscopy characterization of polystyrene spin-coated onto silicon surfaces.* Langmuir, 1992. **8**(3): p. 920-926.

67. Hall, D.B., P. Underhill, and J.M. Torkelson, *Spin coating of thin and ultrathin polymer films.* Polymer Engineering & Science, 1998. **38**(12): p. 2039-2045.

68. Chou, W.-J., et al., *Optimization of the deposition process of ZrN and TiN thin films on Si(1 0 0) using design of experiment method.* Materials Chemistry and Physics, 2003. **82**(1): p. 228-236.

69. Vazquez-Ceron, E.R., et al., *Principal factors determination in the growth of thin films using Taguchi's technique.* Journal of Applied Research and Technology, 2007. **5**(2): p. 113-120.

70. Bao, Z. and A.J. Lovinger, *Soluble Regioregular Polythiophene Derivatives as Semiconducting Materials for Field-Effect Transistors.* Chemistry of Materials, 1999. **11**(9): p. 2607-2612.

71. Brandrup, J. and E.H. Immergut, *Polymer handbook*. 1989, New York: Wiley.

72. Meng, E. and T. Yu-Chong. *Parylene etching techniques for microfluidics and bioMEMS*. in *Micro Electro Mechanical Systems, 2005. MEMS 2005. 18th IEEE International Conference on*. 2005.

73. Yao, T.-J., et al., *Parylene for MEMS applications*. 2002, California Institute of Technology: Pasadena, Calif.

74. Specialty Coating Systems (SCS), http://www.scscookson.com, consulted on October 8, 2010.

75. Ito, Y., et al., *Crystalline Ultrasmooth Self-Assembled Monolayers of Alkylsilanes for Organic Field-Effect Transistors.* Journal of the American Chemical Society, 2009. **131**(26): p. 9396-9404.

76. Delorme, N., et al., *Controlled modification of octadecyltrichlorosilane self-assembled monolayer by CO2 plasma.* Thin Solid Films, 2006. **496**(2): p. 612-618.

77. Wang, Y. and M. Lieberman, *Growth of Ultrasmooth Octadecyltrichlorosilane Self-Assembled Monolayers on SiO2.* Langmuir, 2003. **19**(4): p. 1159-1167.

78. Bai, Y., et al., *Organic thin-film field-effect transistors with MoO3/Al electrode and OTS/SiO2 bilayer gate insulator.* Microelectronics Journal, 2007. **38**(12): p. 1185-1190.

79. Lim, S.C., et al., *Surface-treatment effects on organic thin-film transistors.* Synthetic Metals, 2005. **148**(1): p. 75-79.

80. Todescato, F., et al., *Correlation between Dielectric/Organic Interface Properties and Key Electrical Parameters in PPV-based OFETs.* The Journal of Physical Chemistry B, 2008. **112**(33): p. 10130-10136.

81. Virkar, A.A., S.C.B. Mannsfeld, and Z. Bao, *Energetics and stability of pentacene thin films on amorphous and crystalline octadecylsilane modified surfaces.* Journal of Materials Chemistry, 2010. **20**(13): p. 2664-2671.

82. Yagi, I., K. Tsukagoshi, and Y. Aoyagi, *Modification of the electric conduction at the pentacene/SiO_2 interface by surface termination of SiO_2.* Applied Physics Letters, 2005. **86**(10): p. 103502-3.

83. Malliaras, G., J. Blakely, and A. Mayer, *Vacuum Evaporated Thin Films*, in *Organic Field-Effect Transistors*. 2007, CRC Press.

84. Ohring, M., *Materials science of thin films: deposition and structure*. 2002, San Diego, CA: Academic Press.

85. Cicoira, F., et al., *Correlation between morphology and field-effect-transistor mobility in tetracene thin films.* Advanced Functional Materials, 2005. **15**(3): p. 375-80.

86. Opitz, A., et al., *Bipolar transport in organic field-effect transistors: Organic semiconductor blends versus contact modification.* New Journal of Physics, 2008. **10**.

87. Daniel Frisbie, C. and M. Panzer, *Contact Effects in Organic Field-Effect Transistors*, in *Organic Field-Effect Transistors*. 2007, CRC Press.

88. Necliudov, P.V., et al., *Contact resistance extraction in pentacene thin film transistors.* Solid-State Electronics, 2003. **47**(2): p. 259-262.

89. Cho, J.H., et al., *Effects of metal penetration into organic semiconductors on the electrical properties of organic thin film transistors.* Applied Physics Letters, 2006. **89**(13): p. 132101-3.

90. DeFranco, J.A., et al., *Photolithographic patterning of organic electronic materials.* Organic Electronics, 2006. **7**(1): p. 22-28.

91. Tecan Ltd, *2006, The Photo Electro Forming Process.* Extracted from http://www.tecan.co.uk/ on Onctober 10, 2010.

92. Aljada, M., et al., *High quality shadow masks for top contact organic field effect transistors using deep reactive ion etching.* Journal of Micromechanics and Microengineering, 2010. **20**(7).

93. Apanius, M., P.B. Kaul, and A.R. Abramson, *Silicon shadow mask fabrication for patterned metal deposition with microscale dimensions using a novel corner compensation scheme.* Sensors and Actuators a-Physical, 2007. **140**(2): p. 168-175.

94. Shi, J. and X.R. Qin, *Nucleation and growth of tetracene films on silicon oxide.* Physical Review B, 2008. **78**(11).

95. Choi, J.-M., et al., *Advantages of NiOx electrode over Au in low-voltage tetracene-based phototransistors.* Journal of Applied Physics, 2006. **100**(11): p. 116102.

96. Choi, J.M., et al., *High-performance low-voltage tetracene phototransistors with polymer/AlOx bilayer dielectric.* Electrochemical and Solid State Letters, 2006. **9**(9): p. G289-G291.

97. Santato, C. and F. Rosei, *Organic/metal interfaces: Seeing both sides.* Nat Chem, 2010. **2**(5): p. 344-345.

98. Santato, C., et al., *Organic light-emitting transistors using concentric source/drain electrodes on a molecular adhesion layer.* Applied Physics Letters, 2006. **88**(16).

99. Schreiber, F., *Organic Molecular Beam Deposition: Growth Studies beyond the First Monolayer*. Physics of Organic Semiconductors. 2006: Wiley-VCH Verlag GmbH & Co. KGaA. 15-40.

100. Kowarik, S., A. Gerlach, and F. Schreiber, *ChemInform Abstract: Organic Molecular Beam Deposition: Fundamentals, Growth Dynamics, and in situ Studies.* ChemInform, 2008. **39**(39): p. no-no.

101. Seong, J.W., et al., *Effects of ion bombardment with reactive gas environment on adhesion of Au films to Parylene C film.* Thin Solid Films, 2005. **476**(2): p. 386-390.

102. Fraunhofer IGB, *(2008) Surface tensions of polymers.* http://www.igb.fraunhofer.de/www/gf/grenzflmem/gf-physik/en/GFphys-PolymOberfl.en.html, consulted on November 2, 2010.

103. DataPhysics, *Solid surface energy data (SFE) for common polymers.* (2007) http://www.surface-tension.de/solid-surface-energy.htm, consulted on 28 October, 2010.

104. Cicoira, F., et al., *Environmentally stable light emitting field effect transistors based on 2-(4-pentylstyryl)tetracene.* Journal of Materials Chemistry, 2008. **18**(2): p. 158-161.

105. Papadimitratos, A., et al., *Organic thin-film transistors of pentacene films fabricated from a supersonic molecular beam source.* Applied Physics a-Materials Science & Processing, 2009. **95**(1): p. 29-35.

106. Biscarini, F., et al., *Scaling behavior of anisotropic organic thin films grown in high vacuum.* Physical Review Letters, 1997. **78**(12): p. 2389-2392.

107. Itoh, T. and N. Yamauchi, *Surface morphology characterization of pentacene thin film and its substrate with under-layers by power spectral density using fast Fourier transform algorithms.* Applied Surface Science, 2007. **253**(14): p. 6196-6202.

108. Gavrila, R., A. Dinescu, and D. Mardare, *A power spectral density study of thin films morphology based on AFM profiling.* Romanian Journal of Information Science and Technology, 2007. **10**(3): p. 291-300.

109. Gomes, H.L., P. Stallinga, and D.M. de Leeuw, *Organic materials for active layers in transistors: Study of the electrical stability properties*, in *Advanced Materials Forum Iii, Pts 1 and 2*, P.M. Vilarinho, Editor. 2006, Trans Tech Publications Ltd: Zurich-Uetikon. p. 33-37.

110. Gu, G. and M.G. Kane, *Moisture induced electron traps and hysteresis in pentacene-based organic thin-film transistors.* Applied Physics Letters, 2008. **92**(5): p. 053305-3.

111. Ng, T.N., J.A. Marohn, and M.L. Chabinyc, *Comparing the kinetics of bias stress in organic field-effect transistors with different dielectric interfaces.* Journal of Applied Physics, 2006. **100**(8).

112. Gu, G., M.G. Kane, and S.-C. Mau, *Reversible memory effects and acceptor states in pentacene-based organic thin-film transistors.* Journal of Applied Physics, 2007. **101**(1): p. 014504-9.

113. Bourguiga, R., et al., *Extracting parameters from the current-voltage characteristics of polycrystalline octithiophene thin film field-effect transistors.* European Physical Journal-Applied Physics, 2007. **39**(1): p. 7-16.

114. Veres, J., et al., *Low-k Insulators as the Choice of Dielectrics in Organic Field-Effect Transistors.* Advanced Functional Materials, 2003. **13**(3): p. 199-204.

115. Horowitz, G. and M.E. Hajlaoui, *Grain size dependent mobility in polycrystalline organic field-effect transistors.* Synthetic Metals, 2001. **122**(Compendex): p. 185-189.

116. Reynaert, J., et al., *Ambipolar injection in a submicron channel light-emitting tetracene transistor with distinct source and drain contacts*, in *Organic and Nanocomposite Optical Materials*, A. Cartwright, et al., Editors. 2005. p. 183-190.

117. Santato, C., et al., *Influence of the oxidation level on the electronic, morphological and charge transport properties of novel dithienothiophene S-oxide and S,S-dioxide inner core oligomers.* Journal of Materials Chemistry, 2010. **20**(4): p. 669-676.

CONFERENCES AND PUBLICATIONS

May 2010: Poster presentation at F-Pi-9, International Symposium on Functional Pi-Electron Systems (Atlanta, USA).

Organic Gate Dielectrics for Tetracene Field Effect Transistors: Chemical and Physical Effects.

May 2010: ACFAS (Association francophone pour le savoir): «Propriétés électroniques des matériaux organiques et nanométriques». (Montréal, Québec, Canada)

Couches minces de tétracène sur des substrats diélectriques organiques: croissance, morphologie et propriétés fonctionnelles.

November 2009: Poster presentation at MRS Fall Meeting (Boston, USA).

Tetracene Thin Films on Organic Dielectric Substrates: Growth, Morphology and Charge Transport. (Nominated for Best Poster Award)

C. Santato, L. Favaretto, M. Melucci, A. Zanelli, M. Gazzano, M. Monari, D. Isik, D. Banville, **S. Bertolazzi**, S. Loranger, and F. Cicoira **(2010)**, *"Influence of the oxidation level on the electronic, morphological and charge transport properties of novel dithienothiophene S-oxide and S,S-dioxide inner core oligomers"*, **Journal of Materials Chemistry, vol. 20, pp. 669-676.**